Computational study of electron-transfers and singlet oxygen in aprotic metal-O_2 batteries

Adriano Pierini

Supervised by Prof. Enrico Bodo

SAPIENZA
UNIVERSITÀ DI ROMA

PhD course in Chemical Sciences
XXXV cycle

Department of Chemistry
Sapienza University of Rome

Abstract

The push for decreasing carbon emission is leading many societal sectors toward electrification and urging academic-industrial research toward the optimization of next-generation batteries with increasingly higher energy density. Aprotic metal-oxygen batteries (MOBs), based on the electroreduction of molecular oxygen at a porous cathode, have attracted a vast interest in research, owing to their potential upgrade in terms of energy density and costs over present lithium-ion batteries.

Despite their highly promising features, aprotic MOBs based on alkali and alkaline-earth metals still suffer severe limitations in their practical applicability. One of the main unresolved issues, especially with Li-O_2 batteries, is represented by the high degree of parasitic reactivity. Singlet oxygen ($^1O_2$) is today held responsible for a major contribution to such reactivity, and the disproportionation of the superoxide anion is considered as one of the most likely source of $^1O_2$ in the cell environment. Experimental evidences for electrolyte degradation and evolution of $^1O_2$ have been reported, but the fundamental chemical mechanisms underlying these phenomena are still poorly understood. A valid strategy for contrasting the arise of side-reactions and materials degradation is to use redox mediators (RMs), which allow to recharge the battery with greatly reduced overpotentials. Understanding the connection of RM-assisted charging with the production $^1O_2$ is likely to play a key role in the design of fully reversible and efficient practical MOBs in the future.

In this thesis, quantum chemical computational methods were used to investigate reactive processes of electron-transfer involving reduced oxygen species in aprotic MOBs. The possibility of reactive pathways leading to the release of $^1O_2$ was addressed in particular. The aim of the thesis was to apply theoretical methods to the modeling of reactive systems, in order to unravel part of the mechanisms which underpin the parasitic chemistry of MOBs. Despite their apparent simplicity, the reaction governing the chemistry of the cells involve a complex interplay of radical species and electronic excited states. For this reason, our approach was to use mainly ab-initio correlated multiconfigurational methods for a high-level description of potential energy surfaces and reaction energies. Owing to the computational costs of the methods, such an approach necessarily entails the resort to simplified models,

including the exclusive use of implicit solvent and the neglect of solid phases and interfacial effects.

Chapter One presents an introduction to MOBs and their dedicated literature. In the first section, the fundamental electrochemical reactions at the basis for discharge and charge cycling of alkali and alkaline-earth metals MOBs are analyzed, focusing in particular on the disproportionation of the superoxide radical. The second section discusses the implication of singlet oxygen in the parasitic chemistry of MOBs, from its production to current contrasting strategies. The third section covers the topic of redox mediators, in particular those based on iodine/iodide and bromine/bromide redox couples.

Chapter Two offers a basic recap on the electronic structure theory and methods which were employed during the work for this thesis. The exposition is focused on the concepts, rather than on formulae, aiming at illustrating the main assumptions that underlie the application of different computational methods. The problem of electron correlation is briefly covered, and the most common strategies are presented to recover it via both single-reference and multi-reference methods.

Chapter Three finally presents the results of the work, divided in two parts. The first section is focused on the formation of peroxide species upon disproportionation of the superoxide anion. Thanks to the detailed description of the electronic structure of the system, the proper disproportionation route is found to compete with a metal-reduction route which not only can affect the release of $^1O_2$, but it also open the road for the production of additional reactive species for the onset of degradation reactions. The second section deals with the oxidation of peroxide clusters, as prototype of the discharge products of Li-O_2 batteries, mediated by halogen/halide redox mediators. Different oxidation routes are compared, again trying to point out the most likely pathways leading to $^1O_2$, also taking into account the occurrence of triplet-singlet spin transition triggered by spin-orbit coupling in presence of I and Br heavy atoms.

Contents

List of Figures

List of Tables

Chapter 1

Introduction

The chapter presents the essential concepts on the chemistry and design of aprotic metal-oxygen batteries and especially on the role and implications of the disproportionation reaction of the superoxide radical and its connection to the release of singlet oxygen and parasitic reactivity. The last section discusses the use of redox mediators to promote the oxidation of peroxide/superoxide, and their relations to the release of singlet oxygen.

1.1 Overview on metal-oxygen batteries

1.1.1 Ideas and perspectives

Energy storage and rechargeable batteries play a key role in the long-term perspective of replacing fossil fuels, integrating renewable energy sources into the energy grid and reducing the global carbon emissions at such a pace to contrast the current climate changes. Some of the biggest technological and environmental challenges in our society critically depend on the desirable switch to electrical energy supply. During the last decade the automotive industry has probably been the most impactful sector to be massively hit by the race toward electrification, particularly for what concerns electric cars. As such, the practical requirements of ideal batteries, which could fully sustain the spread of electric mobility, are directly exerting a strong influence on the scientific research at all levels. Many important parameters are to be considered in order to fulfil those requirements, but the strongest driving force in today's research in rechargeable batteries for electric cars is the quest for higher energy density. Specific (or volumetric) energy density is defined as the amount of energy the battery contains per mass (or volume) unit. The limitation due to low energy density is strong: considering the problem of electric cars, a short autonomy not

only hampers the practical use from the standpoint of the consumer, but it also poses severe urgency on the re-design and project of suitable power supply infrastructures. In terms of environmental impact, other aspects are also important: the costs of manufacturing and materials, their toxicity, and the natural abundance of elements in nature. Li-ion batteries (LIBs) have dominated so far the market of portable electronics, but their weight, costs and a potential shortage of lithium make them unpractical for designing an electric car with a power autonomy comparable to gasoline. Some of these topics are currently addressed by the recent research on metal anodes and alternative metal-ion technologies (e.g. Na-ion, K-ion and Ca-ion batteries), but the problem of energy density still has to be overcome. Metal-air batteries are among the candidates for "next-generation" batteries, having the potential for meeting all the above requirements, while at the same time it is expected that intercalation chemistry will soon push Li-ion devices to their practical limits[1].

The original idea of using oxygen as the electroactive cathodic material, together with an alkali metal anode, dates back to several decades ago. Abraham and Jiang[2] were the first, in 1996, to report a working rechargable battery based on the reversible reduction of O_2 gas during discharge. This is still fairly recent when compared to Li-S batteries, another next-generation battery whose development is going on since half a century[3,4]. Also, the concept of metal-oxygen systems was studied on Zn-O_2 batteries in the same years[5], but the underpinning electrochemistry is rather different. Li-O_2 were slowly acknowledged during the 2000s[6–9]. The actual needing of electromotive industry led to an ever-increasing interest, which resulted in a real exploit of publications starting from 2010[10]. Soon, the attempts to overcome the challenges of Li-O_2 also took the direction of exploring the potential of different alkali metals. In the first years of the last decade, it was also the turn of Na-O_2[11,12] and K-O_2[13] batteries, which exploit the hugely superior availability of sodium and potassium compared to lithium. By the same concepts, also alkaline-earth metals gained interest as candidate materials for metal-oxygen batteries, namely Mg-O_2[14,15] and Ca-O_2[16]. The most appealing feature of alkali and alkaline-earth metal-oxygen batteries undoubtedly resides in the very large values of specific energy which are attainable, at least theoretically (see table 1.1.1). Different specific energy values of metal-O_2 batteries are often reported, depending for instance on whether the mass of the device includes or not the oxygen supply, which can be an O_2 gas compartment or even ambient air, in which case it is properly referred to as metal-air battery. In the present work, we will only refer to metal-oxygen batteries (MOBs), because the reduction process at the cathode is altered by the presence of other gaseous species in the air. Overall, for aprotic lithium-oxygen batteries (LOBs) the specific energy density is calculated to be 3505 $W{\cdot}h{\cdot}kg^{-1}$, which is roughly a fourth of that of fossil fuels. The above theoretical density is only referred to

Cell Chemistry	Discharge product	Cell Voltage (V)	Theor. spec. energy ($W \cdot h \cdot kg^{-1}$)
lithium-oxygen	Li_2O_2	2.96	3456
sodium-oxygen	Na_2O_2	2.33	1602
	NaO_2	2.27	1105
potassium-oxygen	K_2O_2	2.20	1070
	KO_2	2.48	935
magnesium-oxygen	MgO	2.95	3921
	MgO_2	2.94	2801
calcium-oxygen	CaO	3.13	2989
	CaO_2	3.38	2515

Table 1.1: Theoretical specific energy density and working voltage for different aprotic metal-oxygen batteries. Source data from refs: [22] [23]

the electrochemical energy associated with the bare chemical reactions, while more realistic estimates taking into account cell materials and cathode porosity are about half of the aforementioned value[17]. Nevertheless it is significant, for the sake of comparison, that the specific energy density of state-of-art LIBs is currently about 300 $W \cdot h \cdot kg^{-1}$ [18] and its rise is expected to reach a plateau over the next decade[19–21]. The Na-O_2 and K-O_2 systems offer a remarkably lower energy density, but still far above LIBs, in exchange of significantly improved stability and reversibility, as will be discussed in the next sections. The theoretical energy density is exceptionally high for alkaline-earth MOBs as well, ranging from 2515 to 3921 $W \cdot h \cdot kg^{-1}$ depending on the metal and the discharge product, but these systems are by far the less studied and are still to be explored thoroughly.

1.1.2 Chemistry and materials of alkali MOBs

The current flow in MOBs is produced by oxidation of the metal at the anode and reduction of oxygen at the cathode. If oxygen is taken from ambient air instead of pure O_2 gas, then other gases also take part in the cathodic process, most noticeably CO_2 and water from air humidity[24,25], and in this case we more precisely refer to metal-air batteries. The tangle of chemical/electrochemical processes taking place upon cycling a MOB is usually referred to as oxygen reduction reactions (ORR), when discharging, and oxygen evolution

reactions (OER), when charging. In the ORR, molecular oxygen O_2 is reduced to superoxide (oxidation state –1/2) and/or peroxide (oxidation state –1) species. The relative stability of the two products (and hence their prevalence) is mainly influenced by the alkali metal, as well as by the complex interplay of cathode, electrolyte and applied voltage. In this regard, a sharp difference has to be marked between aqueous and aprotic MOBs: in the former, the reduction of O_2 is tipically pushed up to the formation of oxide and hydroxide species (oxidation state –2), leading to a completely different cell chemistry, which is out of the scope of this thesis. In the generic case of aprotic MOBs, the ORRs at discharge are summarized in eqns. (1.1-1.4):

$$M \longrightarrow M^+ + e^- \tag{1.1}$$

while molecular oxygen gets reduced at the cathode:

$$O_2 + e^- + M^+ \longrightarrow MO_2 \tag{1.2}$$

$$MO_2{}^- + e^- + M^+ \longrightarrow M_2O_2 \tag{1.3}$$

$$MO_2 + MO_2 \longrightarrow M_2O_2 + O_2 \tag{1.4}$$

The first reduction in eq. 1.2 is electrochemical, and it is common to the chemistry of all of the alkali aprotic MOBs. A further reduction, to peroxide, can subsequently take place, and it can be either a second heterogeneous reduction at the cathode (eq. 1.3) or an homogeneous disproportionation (or dismutation) between two superoxide molecules (eq. 1.4). The two process are considered to be coexistent and competitive, and they are often referred to as the so called "surface route" and "solution route", respectively. A direct two-electron reduction during discharge, i.e. without formation of a MO_2 intermediate, has been generally discarded. In lithium-oxygen batteries, for instance, where superoxide species are very liable because the cell is thermodinamically shifted toward the formation of peroxides, the LiO_2 intermediate has been unambiguously detected with different experimental techniques[26–29], thus giving a direct confirmation of the two-step ORR mechanism.

For the OER, a multi-step mechanism is again invoked. When Li peroxide is formed as the discharge product, the oxidative decomposition of its solid phase starts with a progressive de-lithiation, which forms a mixed superoxide/peroxide phase:

$$M_2O_2 \longrightarrow M_{2-x}O_2 + xM^+ + xe^- \tag{1.5}$$

The faith of superoxide is then twofold, analogously to ORR: it can undergo further elec-

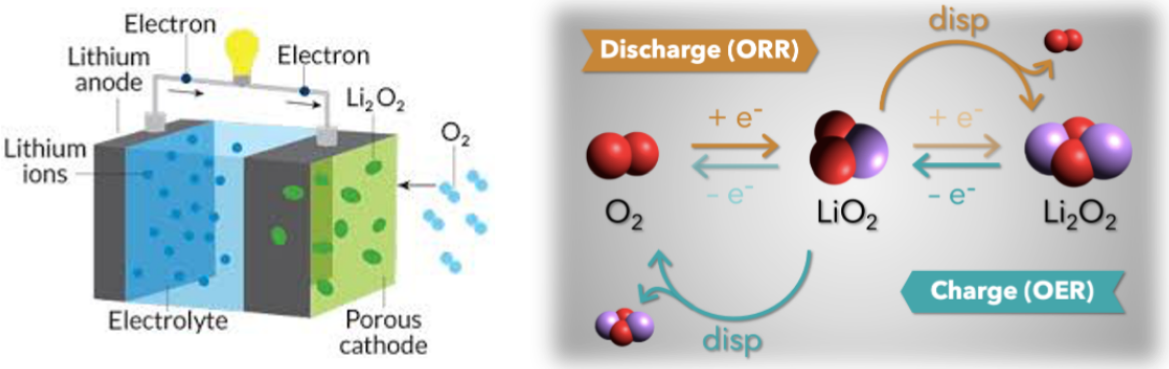

Figure 1.1: General scheme of Li-O_2 cells and their chemical processes on discharge and charge. On the left: the components of a cell and their setup. On the right: the oxygen reduction reactions (ORR), taking place during the discharge, and the oxygen evolution reactions (OER), taking place during the charge.

trochemical oxidation:

$$MO_2 \longrightarrow O_2 + M^+ + e^- \tag{1.6}$$

or chemical disproportionation via a solution-phase mechanism (same es in eq. 1.4). In the case of K-O_2 batteries, the superoxide is predicted to be stable and inert toward disproportionation, so the discharged superoxide is oxidized following mostly the electrochemical path. Na-O_2 is an intermediate case, where different factors can influence the prevalence of superoxide or peroxide at the end of ORR.

Since the introduction of the original concepts of LOB, many different cell setups have been experimented. Most of the research on alkali metal-O_2 batteries is focused on non-aqueous, aprotic electrolytes. The use of water-based electrolytes is an active field of investigation for LOBs, where the molecular oxygen is dishcarged at the cathode to form LiOH, whereas aqueous electrolytes were only seldom employed in sodium- and potassium-oxygen cells. The aprotic solvents for MOBs are usually classified as liquid organic solvents, ionic liquids or solid-state polymers. Among organic solvents, a large variety of compound classes have been tested, since the organic carbonates like those extensively used in LIBs were readily recognized to decompose when employed in LOBs[30]. Ethers and glymes (dimethoxyethane, DEGDME, TEGDME) are currently among the most frequent choices, but stability issues have been thoroughly addressed[31], and the same happened, to a lesser extent, for DMSO[32] and acetonitrile[33]. The problem of chemical and electrochemical stability is partially avoided with some ionic liquid formulations, but the drawbacks typically

consist in a sluggish mass transport across the electrolyte[34]. As a basic configuration, alkali metal plates are used in most cases as anode. These materials offer high reversibility and high specific capacity, but they are also very reactive. Hence, the protection of the anode surface is critical in order to prevent strong reactions with the electrolyte and the formation of an irregular solid-electrolyte interface, which would hamper ionic conduction and favor dendrite growth. For Na-O_2 and K-O_2 batteries, where the metal anode eventually represents a bigger issue, the use of composite anodic materials[35,36] has also shown to improve the SEI. The first requirement of the air cathode is a high porosity, which is essential in order to obtain high battery capacity. Carbon-based materials are therefore the most used cathodic material, for they provide appropriate porosity and electrical conductivity at the same time, at relatively reduced costs. Nevertheless, the electrochemical instability of carbon-based cathods when exposed to high charging overpotentials is a strong issue, which induced the research of alternative materials like TiC[37] or MoC2[38].

1.1.3 The discharge product

The nature of the main discharge product in different aprotic alkali MOBs is determined in first place by the alkali metal itself, for it determines the thermodynamic stability of its respective superoxides and peroxides. The larger alkali cation tend to better stabilize the superoxide, relative to the peroxide, as can be seen by the cell voltages in table 1.1.1, which equate the potential of formation of the discharge product.

Li_2O_2 is overwhelmingly abundant in the discharge products of Li-O_2 batteries, because Li superoxides, both in solution and as bulk, is known to be unstable and to disproportionate with a fast kinetic[40]. LiO_2 phases can be stabilized on purpose by using specific electrode materials at the cathode, like the reduced graphene oxide with added iridium nanoparticles (Ir-rGO) employed by Amine and co-workers[41]. The case of sodium is somewhat an intermediate, where the main discharge product is not uniquely predicted[42,43], owing to the remarkably small difference in the formation potentials (60 mV). Na_2O_2 has been reported to discharge alongside with NaO_2, often as mixed phases[44–46], and their relative proportion is strongly dependent on the chemical environment and the operating conditions. For example, in glyme-based electrolytes, NaO_2 is preferentially formed when cycling at low overpotentials, while at high overpotentials prevails Na_2O_2[47]. Kang and co-workers[48] also concluded from calculations that Na_2O_2 is a stable bulk phase, whereas NaO_2 is more stable at the nanoscale. K-O_2 batteries are generally regarded as working only through reduction to superoxide KO_2[49,50], as it is thermodinamically more stable than the peroxide and it has almost no tendency to disproportionate in aprotic solution. Nevertheless, stable

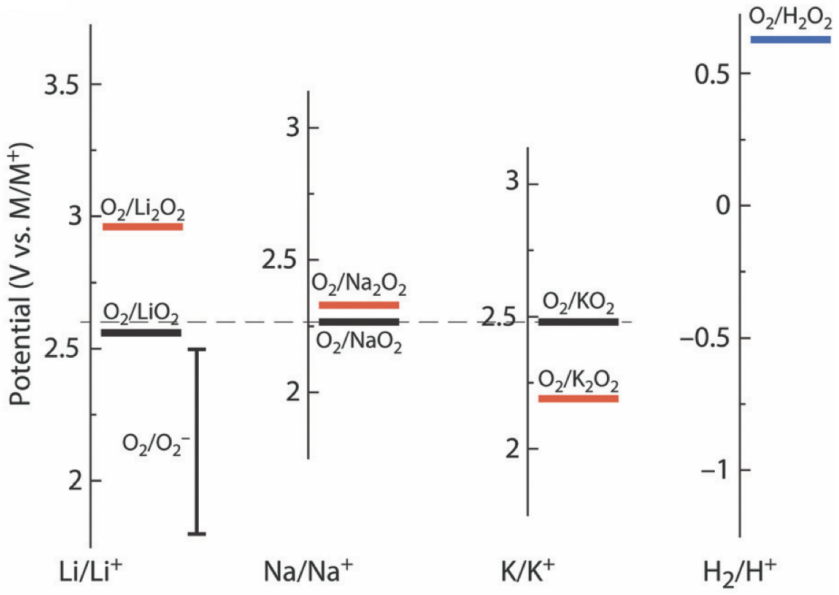

Figure 1.2: Standard potentials of the O_2/MO_2 and O_2/M_2O_2 redox couples on the M/M^+ scales with M = Li, Na, K as well as for the O_2/H_2O_2 couple. The scales are brought to a common scale based on their M/M^+ standard potentials. The dashed horizontal line indicates the O_2/KO_2 couple. Reproduced from ref. [39].

K_2O_2 has been identified after discharge in many cases, in a mix with KO_2, depending on the experimental setup and the applied potential [51–53]. The ORR stopping at the superoxide stage has the obvious disadvantage that less charge can be stored at the cathode during discharge. At the same time, in the case of sodium and potassium, the formation of a superoxide rather than a peroxide has a big compensation, since the simple electrochemical reaction and solubility of the product result in relatively low polarisation and improve the electrode kinetic and reversibility [49].

A key property of the alkaline peroxides, as discharge products, is their poor electric conductivity. Li_2O_2 and Na_2O_2 are both electric insulators, with wide band-gaps which were theoretically estimated to lie in the range of 4 - 5 V [54–58]. The behaviour of superoxides, on the contrary, is seemingly different. Bulk LiO_2, for instance, has a predicted semi-metallic conductivity, with a zero band-gap [59,60], which agrees well with the observed low overpotentials for charging. The calculations on NaO_2 instead predict a significantly larger band-gap [61], in the order of 2 V.

The morphology of the discharge products is strictly related to the mechanism of deposition and growth. As a general argument, two distinct and complementary pathways can dictate the formation of peroxide inside alkali MOBs [62]. In the "surface mechanism" the

intermediate MO_2 formed after the first 1-electron reduction agglomerates as bulk on the cathode surface, where it is further electrochemically reduced to peroxide (see eq. 1.3). In the "solution mechanism", instead, the readily formed O_2^- anion desorbs from the surface and diffuses into the bulk of the electrolyte, where it can react in presence of Li^+ by disproportionation, thus precipitating Li_2O_2 and evolving O_2. The surface mechanism yields peroxide in the form of a thin film, and is favored at high overpotentials and weakly solvating electrolyte. On the other hand, the solution mechanism is responsible for most of the toroid-shaped and micro-sized Li_2O_2 particles, and is favored by low overpotentials and strongly solvating electrolytes. This last case should provide the cell with higher capacity. This rationale, although widely followed in the literature, has been recently refuted by Prehal et al.[63], at least in the case of Li-O_2 batteries, where the authors found the solution pathway to dominate the ORR regardless of the electrolyte and its donor-number. Consistently, the measured capacities lacked a correlation with the expected solvation strength. Also in the case of Na-O_2, disproportionation was found to proceed faster in a solvent with low donor-number, like CH_3CN, than in DMSO[64]. Clearly related to the solvating strength of the electrolyte, the dissociation degree of the alkali salt is relevant to the growth mechanism of the peroxide in Li-O_2 batteries[65]. In glyme solvents, highly dissociated salts like LiFSI and LiTFSI result in the formation of a multilayered discharge mass, that rapidly blocks the electron conduction through the electrode interface; weakly dissociated ones (LiBr, LiAc, $LiNO_3$) instead produce more particle-sized peroxide and have better ORR performances.

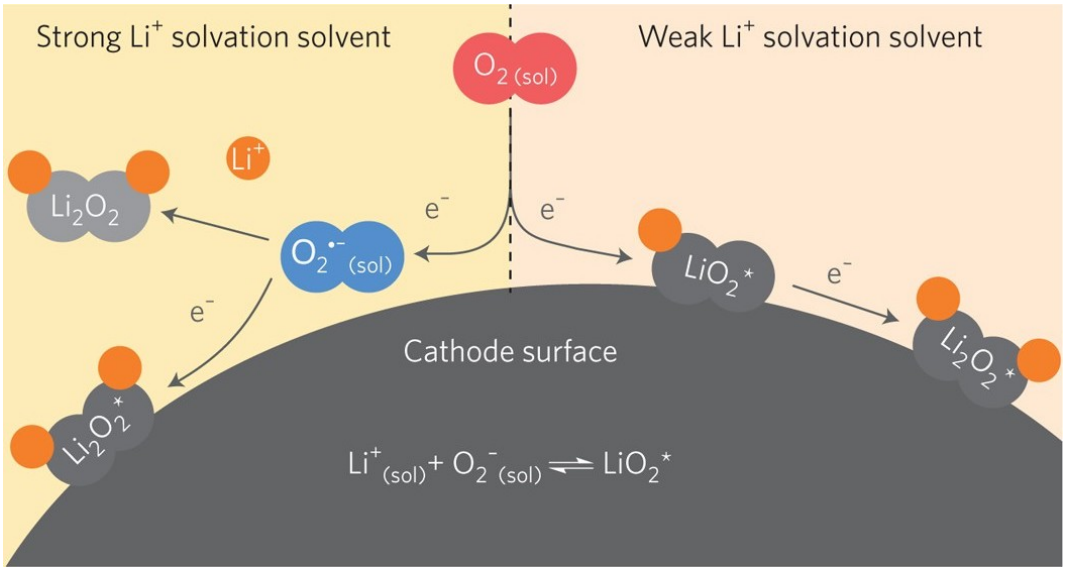

Figure 1.3: Schematic representation of the ORR process in aprotic Li-O_2 batteries according to a surface-mediated (weak solvation, on the right) or solution-mediated (strong solvation, on the left) mechanism.

A key problem in aMOBs is the contamination of the discharge products phase by many side-products. The most common are alkali carbonates, Li_2CO_3 and Na_2CO_3 [66], which are themselves insulators whose oxidation, to be complete, often requests the voltage to raise up to 4.5 V (vs Li+/Li) [67] and 3.4 V (vs Na+/Na) [68], respectively. Together with carbonates, also other organic derivatives are commonly detected, particularly in LOBs, like acetates, formiates and other carboxilates [67]. These unwanted products, which hamper the charging process, are though to be mainly originated by parasitic decomposition of the electrolytes. This point will be further discussed in secs. 1.2.1 and following.

It is worth mentioning that the presence of water heavily impacts the electrochemistry of the ORR, leading to a different composition of the discharge products. In aqueous LOBs, the 4-electron reduction becomes thermodynamically favored, instead of the 2-electron. H_2O molecules are involved in the cathodic process on discharge [69], according to eq. (1.7):

$$O_2 + 2\,H_2O + 4\,e^- \longrightarrow 4\,OH^- \tag{1.7}$$

The product usually grows as an hydrated hydroxide, $LiOH{\cdot}2H_2O$, and it presents interesting advantages over Li_2O_2: it is a better electric conductor, allowing lower overpotentials on charge, and it is relatively soluble in aqueous solution, which positively affects the capacity [70]. But problems also come together with the water-based electrolyte: the stability of the cell is a big issue, in particular for the necessity of carefully protecting the metal anode from the electrolyte [71]. The specific energy density is also lowered to the theoretical value of 1910 $W{\cdot}h{\cdot}kg^{-1}$ [70]. In Na-O_2 batteries, the product deposition upon discharge was found to benefit from traces of water, up to 100 ppm. NaO_2 is transferred onto the growing nuclei via a proton phase-transfer catalysis: HO_2 is formed, which migrates very efficiently trough the electrolyte, then it exchanges ions to NaO_2 and is readily deposited. [72] Reducing oxygen to Li_2O guarantees even higher theoretical specific energy density, 5200 $W{\cdot}h{\cdot}kg^{-1}$ [73]. Very recently, a high-temperature cell assembled with $LiNO_3/KNO_3$ acqeous electrolyte and a LNCO perovskite cathode was reported to maintain high efficiency over 100 cycles while discharging almost exclusively Li_2O as ORR product [74].

1.1.4 The disproportionation of superoxide

The superoxide radical has been often regarded as a highly reactive specie, and its reactivity towards inorganic, organic and biological substrates has been widely reviewed [40,75]. Aqueous solutions or the presence of protic subtrates induce two main reactions of the superoxide radical anion: direct oxidation through proton abstraction, and disproportionation. When

two superoxide molecules (oxidation number = $-\frac{1}{2}$) disproportionate, they yield a peroxide (oxidation number = –1) and a dioxygen (oxydation number = 0). The stability of the superoxide anion in many different homogeneous media has been studied for a long time. Given that the reaction of two bare O_2^- anions, forming a product and transition state with –2 charge, is excluded[76,77], the presence of at least one cation is necessary for the reaction to proceed. The nature of the cation has a strong impact on the reaction rate. Protic substrates are the most well-studied and documented booster for the disproportionation. The accepted mechanism is made up of a protonation step (eq. 1.8):

$$O_2{}^- + H^+ \longrightarrow HO_2 \tag{1.8}$$

followed by an electron-transfer (eq. 1.9) or H-transfer (eq. 1.10) in the proper disproportionation step:

$$HO_2 + O_2{}^- \longrightarrow HO_2{}^- + O_2 \tag{1.9}$$

$$HO_2 + HO_2 \longrightarrow H_2O_2 + O_2 \tag{1.10}$$

The reaction in water is very fast, and it is reported to follow mostly the stoichiometry of eq. (1.9), with a rate constant of $\sim 10^7$ $M^{-1}s$ against $\sim 10^5$ $M^{-1}s$ of eq. (1.10)[76]. In aprotic solvents, the competition of the two mechanisms is mainly determined by the acidic strength of the protic substrate. It is found that the presence of acids as weak as water or phenols[75,78] is enough to induce a fast disproportionation in aprotic solvents like DMSO, DMF or CH_3CN, and the reaction follows an electron-transfer mechanism like in eq. (1.9). Strong acids should favor instead the H-abstraction mechanism of eq. (1.10)[79]. This is also related to the first protonation process in eq. (1.8) being or not the rate-limiting step: if this is not the case, then it acts as a fast pre-equilibration step, which can be of first or second order relative to $[O_2^-]$ concentration. Disproportionation is fast enough that, during the electrolytic reduction of O_2, the electrochemical reduction of superoxide to peroxide is negligible[78]. In aprotic metal-oxygen batteries, the disproportionation may occur if properly driven by metal cations, though it has to be kept in mind that moisture or protic contaminations are not easy to avoid. Alkali cations show different effectiveness in promoting the disproportionation. KO_2 is well known to form stable solutions in aprotic solvents: in absence of proton sources, potassium cations simply do not induce the disproportionation of superoxide[80]. On the other hand, there is evidence that lithium cations efficiently induce superoxides to disproportionate. When a stable solution of a superoxide salt in aprotic solvent (like KO_2 or $TBAO_2$, where TBA is tetrabutylammonium) is added with a lithium-

containing salt, a fast disproportionation of the superoxide is typically triggered[39]. A same phenomenon is observed when Li^+ is added to O_2^- anions electrogenerated in DMSO from a O_2-saturated solution[81]. The instability of solid lithium superoxide is also also something well-reported in the litterature since a long time[82–84]. Sodium superoxide is also prone to react by disproportionation. Depending on the operating conditions, discharged NaO_2 is often found to be unstable after cycling in Na-O_2 batteries, with consequent evolution of O_2 gas[85]. Both dissolved and surface-deposited NaO_2 are unstable and can convert to Na_2O_2, the kinetics of the reaction being highly influenced by the solvating ability of the electrolyte. For instance, solvents with low Gutmann donor number (DN), like acetonitrile, enhance the disproportionation kinetics, while this latter turns to be sluggish in solvents like DMSO, which present high DN[64,86]. The overall trend, with decreased reactivity toward superoxide disproportionation going from Li to Na to K, has been rationalized in terms of Lewis acidity of the cation[26,39], where the smaller cations Li^+ and Na+ are stronger Lewis acids and form ionic bonds with the superoxide anion, while the larger K^+, with lower charge density, interacts more weakly with the anion. This argument is in agreement by the null reactivity of superoxide in aprotic solutions of tetraalkylammonium salts, that is well-known to be a very weak Lewis acid, and can be related to the precipitation/solubility of the different reduced oxygen species[26].

He et al.[87] have proposed a kinetic model for the disproportionation of LiO_2 which exhibits a good fit with the data in DMSO and DMF. According to this model, the association equilibrium (eq. 1.11) is more likely followed by a direct reaction (electron-transfer) between LiO_2 and O_2^- (eq. 1.12), rather than by the self-reaction between two associated LiO_2 neutral superoxides. The formed peroxide anion LiO_2^- then is rapidly binded to a Li^+ cation (eq. 1.13):

$$O_2{}^- + Li^+ \longrightarrow LiO_2 \tag{1.11}$$

$$LiO_2 + O_2{}^- \longrightarrow LiO_2{}^- + O_2 \tag{1.12}$$

$$LiO_2{}^- + Li^+ \longrightarrow Li_2O_2 \tag{1.13}$$

Independently of the nature of the two solvent, eq. (1.11) is found to be a fast equilibrium, hence the rate determining step is represented by eq. (1.12). Accordingly, the whole process results to be first order in superoxide at high $[O_2^-]$ concentrations, while it becomes second order at low concentration.

1.1.5 Hints on alkaline-earths MOBs

Together with the interest in Na- and K-based alternatives to Li-O_2 batteries, systems based on alkaline-earth metals have started to be investigated. Magnesium and calcium have proven to be potentially suitable anode materials[88–90] in an aprotic environment, and their abundance, availability and relatively low cost (compared to lithium) make them attractive alternatives. The theoretical capacity are also extremely appealing[91]. Compared to cells based on monovalent $Li^+/Na^+/K^+$ cations, divalent Mg^{2+}/Ca^{2+} cations with their higher charge density establish stronger interactions with the electrolyte solvent and counter-anions. As a general consequence, solubilities, ionic transport and conductivity can be drastically reduced[23]. As in alkali MOBs, the discharge products formed during the ORR electrical insulators and require large overpotentials to be applied during the OER in order to be electrochemically decomposed[92,93].

Differently from alkali metals, magnesium superoxide forms at far lower potential than peroxide. Based on both redox potentials and post-cycling characterization, the ORR in DMSO can bu summed up as an electrochemical-chemical-chemical process[14], where the first oxygen electro-reduction to superoxide (eq. 1.14) is followed by chemical disprportionation of $Mg(O_2)_2$ to form MgO_2 (eq. 1.15), and this last one disproportionate again to form MgO as a last product (eq. 1.16):

$$O_2 + e^- \longrightarrow {O_2}^- \tag{1.14}$$

$$2\,{O_2}^- + Mg^{2+} \longrightarrow MgO_2 + O_2 \tag{1.15}$$

$$2\,MgO_2 \longrightarrow 2\,MgO + O_2 \tag{1.16}$$

The final discharge product present a MgO crystalline phase, with amorphous domains of MgO_2, which remains for kinetic reasons without being converted to oxide. $Ca(O_2)_2$ instead is kinetically stable and does not undergo disproportionaiton[16], even if thermodinamically the formation of CaO_2 is strongly exoergonic, even more than CaO. Calcium superoxide, in fact, can be also synthesized as a stable salt[40]. Hence, the faith of the calcium superoxide results to be heavily dependent on the cathode surface. Bawol et al.[94] reported that $Ca(ClO_4)_2$ salt in DMSO forms dissolved superoxide when reduced on a Pt or glassy carbon electrode, which remains as an undissociated contact ion-pair and need high overpotentials in order to be re-oxidized. On the other hand, on a Au electrode the calcium peroxide is formed, since the kinetic barrier for superoxide to disproportionate in presence of Ca^{2+} cations is no more an obstacle. In this situation, the authors revealed by mass-spectrometry a significant current of unexpected species, like CO_2, which are interpreted as products of

side reactions.The origin for this side reactivity was tentatively referred to the formation of singlet oxygen, as supported by the fact the CO_2 release resulted intensified upon adding a proton source to the solution, compatibly with increased superoxide disproportionation. Anyway, the 2-electron reduction process leading to CaO_2 only lasts as long as the peroxide product doesn't accumulate blocking the active sites on the surface of the electrode. When this happens, the second electron-transfer is hindered across the first layer of discharge products, and only superoxide is subsequently formed above that layer[95].

1.2 Parasitic reactivity and singlet oxygen

1.2.1 Evidences for parasitic reactivity

In a fully reversible cell, during discharge the transferred electron to oxygen ratio has to be $e^-/O_2 = x$ with $x = 1$ or 2 depending on whether molecular oxygen is discharged to superoxide or peroxide, and the same applies, on charge, for the passed electron to consumed (su)peroxide ratio, e^-/M_xO_2[96]. In LOBs, the deviations from reversibility are dramatically

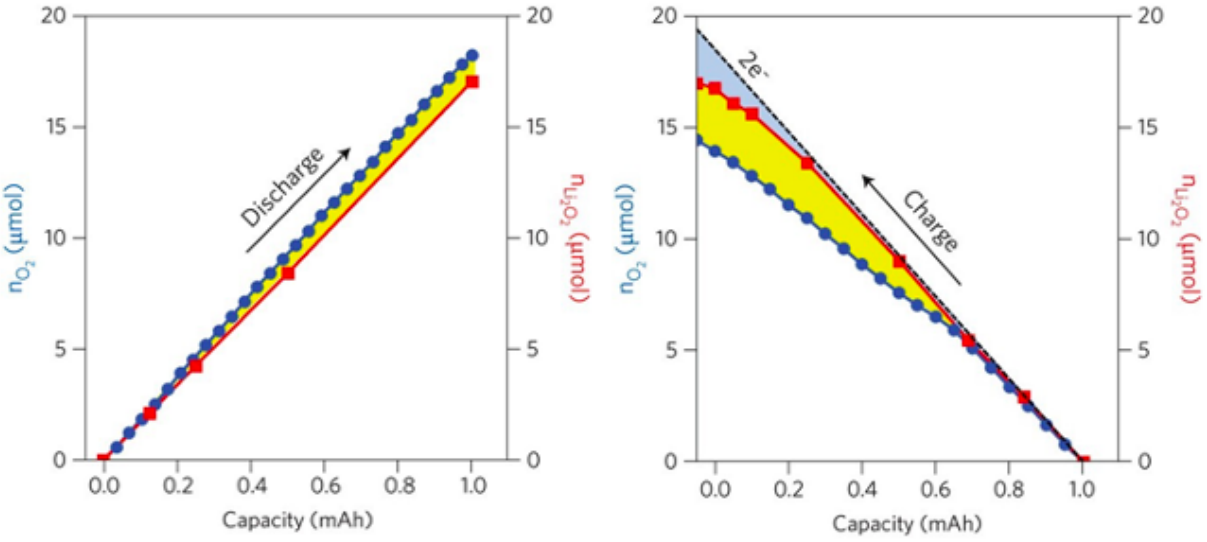

Figure 1.4: Deviation from reversibility in Li-O_2 electrochemistry. On the left: number of moles of O_2 consumed (blue) and Li_2O_2 formed (red), during discharge. On the right: number of moles of O_2 evolved (blue) and Li_2O_2 consumed, during recharge. The regions in yellow give a measure of the contribution by parasitic reactions. Reproduced from ref.[97]

displayed, particularly for charging[98]. The leading culprit for this lack of reversibility is the amount of unwanted side reaction that take place during ORR and OER. This entails, in

first place, the progressive degradation of cell materials and, in second place, the release of side-products which often happen to be electrical insulators[99]. LOBs were soon found to be severely plagued by parasitic reactivity, where most of organic solvents proved to be unstable upon cycling[100]. Large amounts of side products coming from electrolyte degradation were found with traditional Li-ion carbonate-based electrolytes, but also with various ethers and DMSO[101–104]. Ionic liquids were found to produce much less carbonates side products[105], but the improved stability is typically offset by poor transport properties. The amount of side reactions at the expense of the electrolyte is typically lower in Na-O_2 batteries, but still enough to seriously impact the cyclability of the cells[106,107]. K-O_2 batteries, instead, are relatively safe from this point, displaying a high reversibility[108,109]. The carbon-based part of the cathod is also widely reported to undergo intense parasitic reactions in the environment of alkali MOBs, causing the polarization to rapidly increase and accelerating the fading of capacity during cycling[110].

1.2.2 Discovery of singlet O_2

For many years the parasitic chemistry of LOBs was mainly believed to arise from the chemical reactivity of reduced oxygen products and intermediates, and the nucleophilic attack of peroxides and superoxides against different electrolytes was investigated[111–114]. For what concerns the degradation of the cathode, the voltage of 3.5 V vs Li^+ was identified as the threshold for charging before serious degradation of the carbon cathodes starts to take place[115]. The occurrence of side reactions with some form of reduced oxygen species was consequently addressed[116], since carbon electrode materials are generally known to be electrochemically stable below 4 V. In 2016, Wandt et al.[117] made the unprecedented finding of significant production of singlet oxygen, that is, the O_2 molecule in its first singlet excited-state. It was readily recognized that this result paved the road for a new and deeper understanding of the cell chemistry. The release of singlet oxygen was clearly confirmed in later works[81,118,119], and analogous phenomenon was later find to impact Na-O_2 batteries as well[120]. K-O_2 systems, instead, seem to be free from this problem[121].

The electronic ground state of the O_2 molecule has a triplet spin multiplicity, $^3\Sigma_g$, with two unpaired electrons in the two degenerate frontier orbitals π^*. The first excited state is a singlet, $^1\Delta_g$, which lies 0.98 eV above the triplet. Because of the spin-forbidden transition to the ground state, it is a metastable state whose lifetime in solution can reach the order of 10^{-3} s[123]. The next singlet, $^1\Sigma_g$, has a vertical excitation energy of 1.65 eV, and it is highly unstable as it immediately decays to the lower singlet. The electronic configuration of these three lowest states can be represented with a minimal orbital space made up of

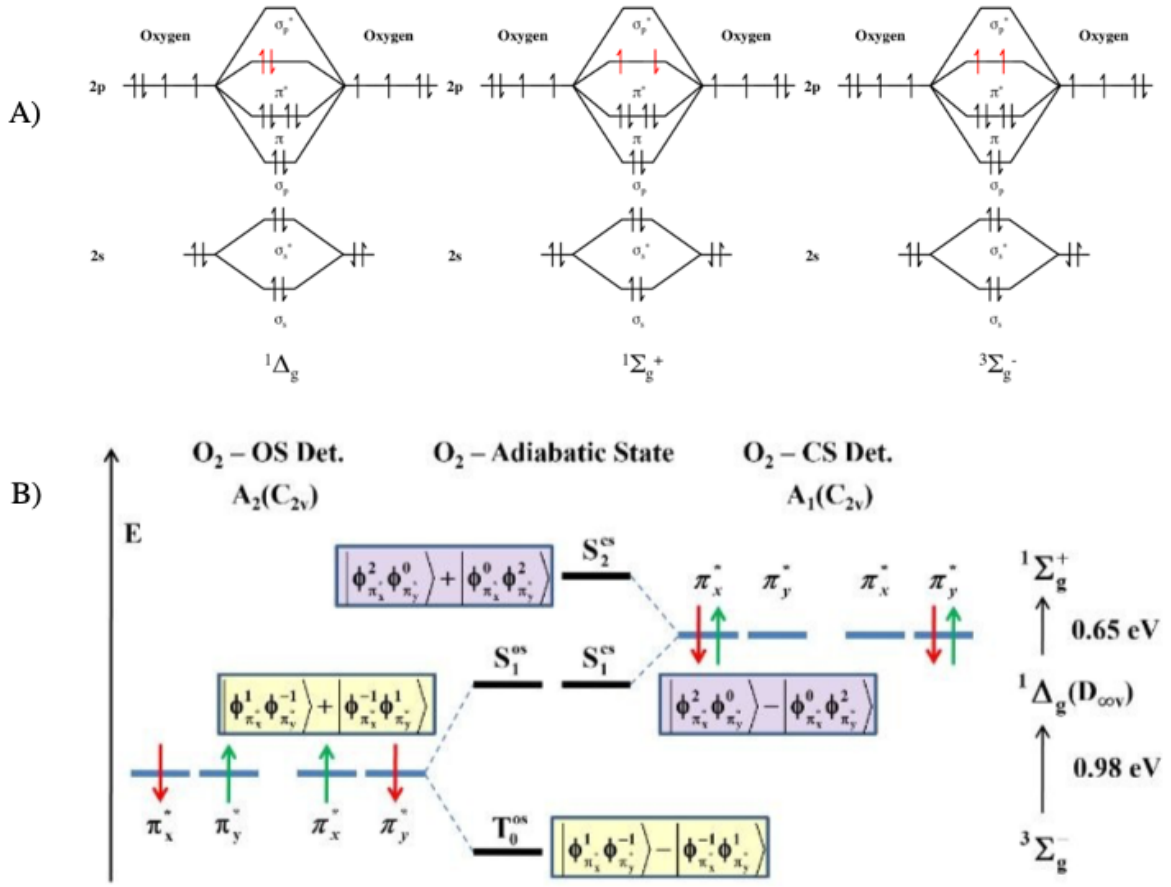

Figure 1.5: Scheme of the electronic structures of the first three electronic state of O_2. A) Molecular orbitals occupations, with the traditional representation of the $^1\Delta$ state as a closed-shell conifugration. B) The more accurate representation given in ref.[122].

the two π_g^* antibonding frontier orbitals. In a traditional picture, the two singlet $^1\Delta_g$ and $^1\Sigma_g$ states are represented as a closed-shell and a singlet-open shell configuration, respectively[124,125]. However, more recent theoretical studies pointed out that the actual situation is more complicated: the $^1\Delta_g$ in $D_{\infty v}$ is doubly degenerate, and the two components have contributions by both the open-shell and the closed-shell configurations[126,127]. This higher-level description is actually able to better rationalize the reactivity of $^1\Delta_g$ oxygen toward different substrates, since the two configurations can be shown to gain different weights depending on the reaction mechanism in which they are involved[122]. Summing up, it is clear that the electronic structure of singlet oxygen is inherently multiconfigurational, hence multireference methods are required in ab-initio calculations in order to obtain a qualitatively correct wave function. Despite the fundamental inadequacies of single-determinant methods in representing the correct electronic structure of singlet states in molecular oxygen,

many computational works opted for a DFT approach when studying reactions involving $^1O_2$. In these cases, usually a broken-symmetry wave function is employed, together with a spin-projection correction of the energy[128,129]. Alternatively, a constant shift of approximately 0.98 eV may be applied to the electronic energy of the triplet ground-state[130–132], but this approach is limited for it inherently fails to locate transition states or regions of the PES where the vertical excitation $^3\Sigma_g \rightarrow {}^1\Delta_g$ could be significantly altered.
The chemical reactivity of singlet O_2 is that characteristic of an electrophile. Typical substrates that easily react with $^1O_2$ are therefore those presenting electron-rich moieties such as double bonds and π systems. Double-bonds can react with $^1O_2$ through stereospecific ene-reactions, leading to the formation of reactive hydroperoxides[133,134]. Endoperoxides instead are formed by cycloaddition to dienes or aromatics[135–137], as in the case of [4+2]-cycloaddition reaction with napthalene derivatives, which is exploited to detect singlet oxygen by fluorescence or UV-vis absorbance spectroscopy. Diels-Adler reactions can also occur between a diene and singlet oxygen acting as the dienophile[138]. $^1O_2$ has also proved to be reactive towards organic sulfides[139,140], and even weakly activated C-H bonds of saturated hydrocarbons[141]. This implies that most of the solvents employed as electrolytes, be them organic or ionic liquids, are potentially unstable and are likely to undergo parasitic reactions upon evolution of $^1O_2$.
Today, the main source is thought to be the superoxide disproportionation, the same reaction that plays a fundamental role in the redox chemistry and guarantees a high discharge capacity.

1.2.3 $^1O_2$ from superoxide disproportionation

The relation between superoxide disproportionation and singlet oxygen has been long debated in the past, well ahead of the raise of MOBs, also because of an implication in some biological processes[142]. Whether a proton-induced disproportionation of superoxide anions can be regarded as a relevant source of $^1O_2$ has been a controversy for decades, with both affirmative[143–147] and negative[148–152] claims repeatedly proposed by many authors. In these works, now considerably outdated, the main source of disagreement typically focused on the reliability of the experimental procedure employed for the detection of the highly reactive $^1O_2$.
From a thermodynamic standpoint, it is possible to generate O_2 in the first excited state starting from $2O_2^- + 2H^+$ reactants, because the triplet ground state of the products is exoergonic by 37 kcal/mol[148,153,154]. Even if the $^1\Delta_g$ singlet lies about 22 kcal/mol above the $^3\Sigma_u$ triplet, the production of an electronic excited state can be favored over the thermal

dissipation of the reaction energy if a very fast electron transfer takes place[155].
The release of singlet oxygen upon exposing O_2^- anions to protic solutions was also claimed in more recent publications. As an example, Lozano at al.[156] observed that the addition of protic substrates to a Na-O_2 battery not only increases the capacity, because it promotes a solution-mediated mechanism (as also in ref.[72]); but, at the same time, it hampers the cell cycling because of more singlet oxygen is produced. The reason for this is the protonation of O_2^- to form HO_2, even with acids as weak as ammonium salts, which readily reacts according to eq. (1.9) or (1.10) to release a significant amount of $^1O_2$.
Singlet oxygen inside the aprotic environment of aprotic LOBs was first reported in 2016 by Wandt et al.[117]. The hypothesis about its origin readily pointed toward the superoxide disproportionation reaction[97,118], at least as a main source, since it is expected to carry a major contribution on O_2 gas evolution during both charge and discharge. Little later, also sodium-O_2 batteries were found to be affected by the same phenomenon[120]. Whereas most of $^1O_2$ is detected on charging, prompted by need for high overvoltages, Cordoba et al.[81] clearly proved that significant amounts are also produced by ORR during discharge.
Mourad et. al.[39] made the unprecedented claim that the fraction of singlet oxygen evolved increases following the order of the weakest Lewis acid, that is, in a reverse order with respect to the superoxide disproportionation reactivity. In fact, in their experiments, the addition of Na^+ salts to a KO_2 solution in TEGDME resulted to produce, upon disproportionation, a significantly higher quantity of $^1O_2$ than Li^+ salts, despite the overall evolved molecular oxygen being much less in the former case. In addition, a far superior $^1O_2$ yield was detected when charging a Li-O_2 battery with a mixed Li^+/TBA^+ electrolyte. If unknown side-reactions are excluded, this effect is not compatible with the neat increase of ca. 1 eV (the $^3\Sigma \rightarrow {}^1\Delta$ excitation energy) on the ground-state $^3O_2$ evolution threshold. The authors hence conclude that i) cations which behave as weak Lewis acids can favor the formation of $^1O_2$ in a chemical way, and ii) the maximum $^1O_2$ yield is reached by combining into the electrolyte weak Lewis acids with harder cations, which give high disproportionation rates (like Li^+). As a practical consequence, big care must be taken with the choice of lithium salts and IL solvents in the electrolyte, since these often employ weak Lewis acid as cations in the ion pair. The study clearly point to the direction of the cation exerting an active influence on the reaction barrier towards excited-state O_2 through some chemical mechanism, which nevertheless remains unclear. DFT calculations were also carried out in the aforementioned work, in order to sustain this hypothesis. Differently from other previous theoretical studies on LiO_2 disproportionation[157,158], these calculations did also take into account the singlet excite state.
Under a mechanistic point of view, the superoxide disproportionation has been generally

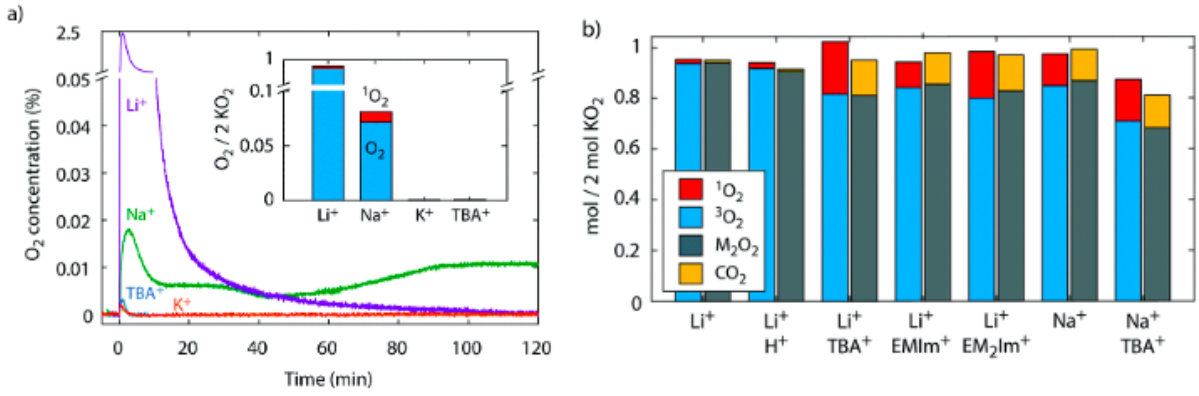

Figure 1.6: Singlet oxygen from superoxide disproportionation in TEGDME electrolytes containing different cations. On the left: O_2 evolution over time. On the right: amounts of O_2, $^1O_2$, and Li_2O_2 (or Na_2O_2) obtained from reacting different cations with free O_2^- anions (KO_2 dissolved in presence of 18-crown-6). Reproduced from ref.[39].

treated as an electron-transfer process. As such, Houchins et al.[159] applied the semiclassical Marcus theory in order to analyze the kinetics of the disproportionation, and came to the conclusions that $^1\Delta$ oxygen becomes more kinetically favored with increasing fraction of superoxide present as dissociated free O_2^- anions, instead of $Li^+O_2^-$ or $Na^+O_2^-$ ion pairs.

A novel mechanism for the reaction of eq. (1.10) has been recently proposed by Dong et al.[160], where the simple electron-transfer scenario gets considerably complicated by evidences of the cleavage of oxygen-oxygen bonds (fig. 1.7). By discharging a cell using an isotopic mixture of $^{16}O^{16}O$ and $^{18}O^{18}O$, the authors found that 4.5% of the evolved oxygen presents the $^{16}O^{18}O$ isotopic composition. This result implies the scrambling of oxygen atoms belonging to distinct superoxide molecules, something that can occur as a result of the formation of a LiOOOOLi tetroxide intermediate by coupling two isotopically pure $^{18}O^{18}OLi$ or $^{16}O^{16}OLi$ radicals (eq. 1.17):

$$^{18}O^{18}OLi + {}^{16}O^{16}OLi \longrightarrow Li^{18}O^{18}O^{16}O^{16}OLi \longrightarrow Li^{18}O^{16}OLi + {}^{16}O^{18}O \qquad (1.17)$$

Moreover, the detected fraction of isotopic $^{16}O^{18}O$ accounted for more than 40% of the singlet oxygen produced, making the bond-cleavage mechanism a possible major source for the generation of singlet oxygen in LOBs. It is important to mention that analogous evidences were already produced back in 1988 by Sugimoto ans Sawyer[152] for the reaction of two hydroperoxyl radicals (or hydrogen superoxide, HO_2). These authors claimed that the formation of a HOOOOH tetroxide intermediate (similar to eq. 1.17) was responsible

for the large majority of $^1O_2$ yield during the electrolytic reduction of H^+ in acetonitrile in the presence if dissolved O_2, whilst the electron-transfer and hydrogen-transfer mechanisms only contributed to the evolution of ground-state triplet oxygen. Similar conclusions have also been drawn in the case of ROO· peroxyl radicals, which can release singlet oxygen by forming a ROOOOR tetraxoide[161]. Theoretical calculations[162] have shown that HOOOOH is expected to be a more stable reaction intermediate in HO_2 self-reaction than the $HO_2 \cdots HO_2$ dimer, in both gas and aqueous phase. Moreover, its decomposition was later reported to be an effective source of singlet oxygen in organic synthesis[163]. While hydrogen tetroxide has been the subject of many studies, both computational and spectroscopic, it has to be noted that the existence of LiOOOOLi-like species has never been addressed before.

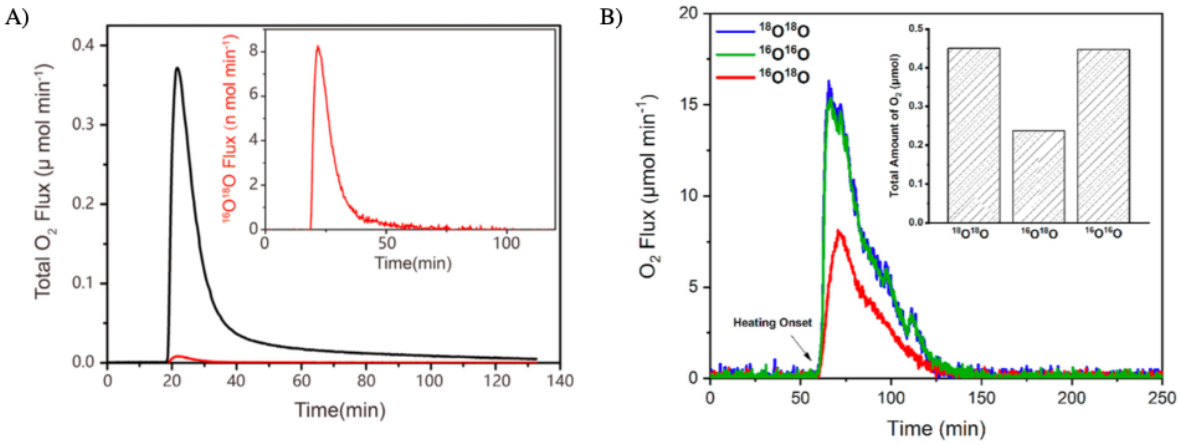

Figure 1.7: Oxygen gas evolution from the scrambling pathway. A) Total oxygen (black) and $^{16}O^{18}O$ (red) measured through on-line mass spectrometry, after mixing a superoxide solution with LiTFSI. B) $^{16}O^{16}O$, $^{18}O^{18}O$ and $^{16}O^{18}O$ gas evolution from a cell discharged with a 1:1 mixture of the two isotopically pure gases. Reproduced from ref. [160]

The role of surface chemistry is still not well clarified, though many evidences suggest an interplay of heterogeneous routes and singlet oxygen release. Some commonly employed solid catalysts, from noble metals to transition metal oxides, were reported to lower the activation barrier of the singlet pathway[164]. The role of surface was also discussed as related to the aforementioned bond-cleavage mechanism of disproportionation. In ref. [152] the reaction is proposed to proceed via adsorption of the H terminations in HO_2 to the surface, while the authors of ref. [160] excluded an active involvement of the surface during the formation and braking of LiOOOOLi, which then has to proceed as a solution homogeneous process.

In conclusion, the disproportionation reaction is fundamental to achieve a high capacity,

allowing the decomposition of the discharge products, but it also contributes to increase the irreversibility of charge-discharge cycling. This situation has been summed up as the dilemma of disproportionation[39,124]. Ideally, new strategies to deactivate the $^1O_2$ are necessary, while still allowing the disproportionation and without altering the underpinning chemistry in order to fully exploit the superior potential of LOBs.

1.2.4 $^1O_2$ from other sources

Alkali carbonates are regularly detected by X-ray diffraction as a side-product of the ORR in lithium- and, to a lesser extent, sodium-oxygen aprotic batteries (see section XX). As in the case of alkali peroxides, those carbonates are insulators and their decomposition requires high overvoltages during the charging. Li_2CO_3 is decomposed with CO_2 evolution upon charging at 3.8 - 4.0 V according to the semi-reaction[165]:

$$Li_2CO_3 + 2\,e^- \longrightarrow 2\,Li^+ + CO_2 + \frac{1}{2}\,O_2 \tag{1.18}$$

In contrast with eq.(1.18), many studies reported the absence of conjoint CO_2 and O_2 gas evolution[165],[166]. By using 9,10-dimethylanthracene as a singlet oxygen trap, Mahne et al.[119] discovered instead a peak of $^1O_2$ at the onset of CO_2 evolution, which coincides with electrochemical oxidation of Li_2CO_3. Ground-state $^3O_2$ is evolved, instead, if the battery is charged over 3.8 V in presence of a singlet oxygen quencher (DABCO). This allowed the authors to suggest a proposed mechanism where new O-O bonds are formed, namely through a Li peroxodicarbonate intermediate (fig. XX). Similar findings were then confirmed by Cao et al.[167], who showed that, during the decomposition of lithium carbonates, an important contribution to the evolved CO_2 is originated from side-reactions of singlet O_2 with the electrode carbon substrate. The addition of Co_3O_4 nanoparticles, a well-known oxygen evolution catalyst, was found to significantly suppress singlet oxygen, by stabilyzing the reaction intermediates of forming $^1O_2$, as already observed in ref.[168].

Apart from promoting disproportionation (see section 1.2.3), the presence of trace water can also contribute through the formation of H_2O_2 product. The contact with many inorganic catalysts is well-known to induce a peroxide disproportionation reaction, which yields H_2O and O_2, this latter one possibly in the singlet excited state[169,170]. Samojlov et al.[164] revealed that the nature of the cathode and of the solid catalysts deposited above has large impact on the fraction of $^1O_2$ generating from this reaction, with transition metal compounds generally showing a tendency to increase it.

Finally, an impactful role on the generation of singlet oxygen can be exerted by homogeneous

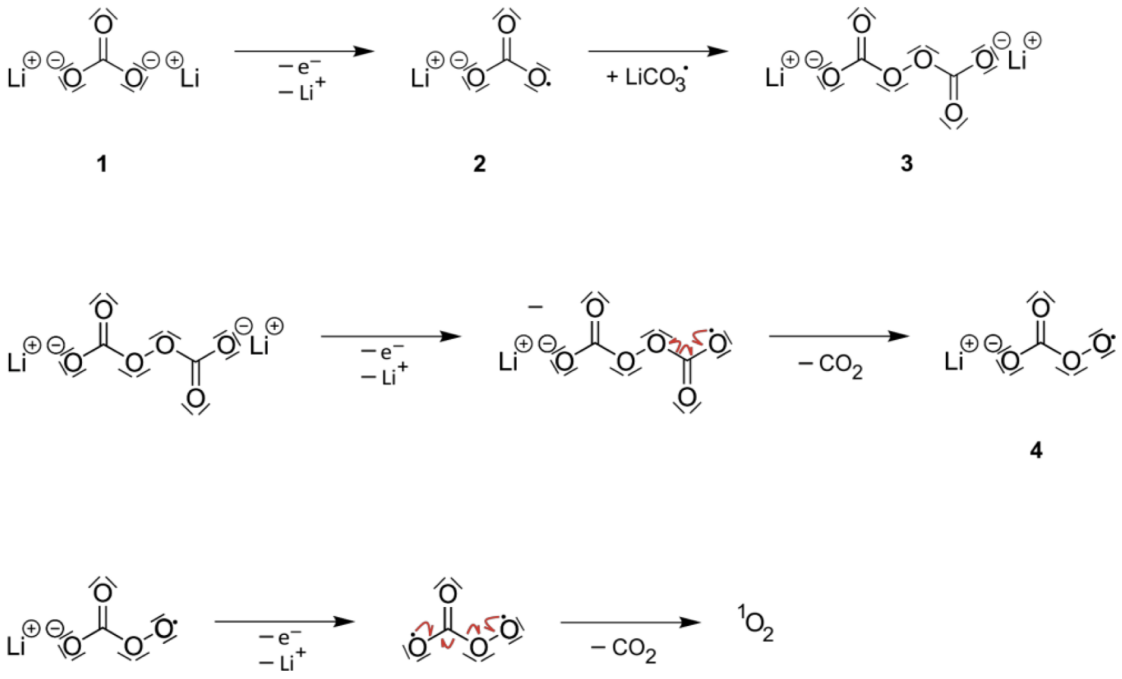

Figure 1.8: Proposed reaction mechanism of the electrochemical oxidation of lithium carbonate. A peroxodicarbonate intermediate LiO_2COOCO_2 is formed (3), and the homolytic cleavage of its O-O bond leads to stepwise elimination of 2 CO_2 and $^1O_2$. Reproduced from ref.[119].

redox catalysts, usually referred to as redox mediators, that are intended to ease the transfer of electric charge from the discharge products to the electrode during charging. A more detailed discussion about this topic is deferred to section 1.3.2.

1.2.5 Strategies against $^1O_2$

The long lifetime of the $^1\Delta_g$ O_2 excited state implies that deactivation can be an effective strategy in order to suppress the parasitic chemistry originated by singlet oxygen. Deactivation of $^1O_2$ can be accomplished either by chemical or physical quenching, as summarized by Ruiz de Larramendi and Ortiz-Vitoriano[124]. In chemical quenching, the target specie undergo a chemical reaction with a quencher or molecular trap, leading to the formation of a compound which can be stable or evolve into other products that do not yield O_2 back. A well known chemical quencher in the field of LOBs is dimethyl-antracene (DMA), which is widely used as a singlet oxygen trap for it forms a endoperoxide which can be accurately

revealed by a characteristic fluorescence emission peak between 300 and 500 nm[171]:

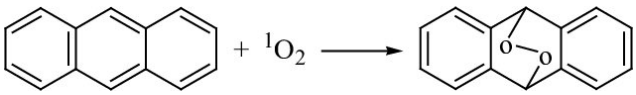

(1.19)

While this process can be useful for revealing and quantifying the formation of parasitic $^1O_2$, the clear downside is that O_2 is progressively consumed, hence a systematic suppression by chemical trapping would lead the cell to premature death. Also, the quenching reaction can form intermediate species which can result to be insoluble and block the air cathode pores. Physical quenching, on the other hand, preserves the species chemically unaltered, because it simply acts on the relaxation rate of the excited-state to the ground-state. This can happen through the two limit mechanisms: energy-transfer or charge-transfer. Deactivation by energy-transfer can take place as the inverse of the $^1O_2$ generation process via photosensitization[172]:

$$^1O_2 + {}^1Q \longrightarrow {}^3O_2 + {}^3Q \tag{1.20}$$

which means that the excited state relaxes to the ground state dissipating its excess energy without any change in the global spin multiplicity (in the example equation above, the two triplets are coupled in order to give a global singlet). Alternatively, physical quenching can occur via charge-transfer, where a charge-transfer complex intermediate is formed between the quencher (Q) and the electron-deficient $^1O_2$:

$$^1O_2 + Q \longrightarrow [O_2{}^- \cdots Q^+] \longrightarrow {}^3O_2 + Q \tag{1.21}$$

What makes this mechanism effective is the property of the charge-transfer complex to undergo fast and radiationless spin transition between states with different multiplicities, which requires intersystem crossing (ISC) in order to happen. As an example, triphenylamine (TPA) was reported by Jiang et al.[173] to form a singlet charge-transfer complex with $^1O_2$, which can easily decay to a triplet complex via ISC, and ultimately free up ground-state $^3O_2$. Owing to this mechanism and its fast kinetic, the cycle-life of a same LOB with LiTFSI/tetraglyme electrolyte and carbon nano-tubes air cathode was prolonged from 20 to 310 cycles, before a large increase in the charge-discharge voltage gap could take place. Fast quenching rates by charge-transfer generally require high electron donicity[174], but this results in low anodic stability[175].

The addition of appropriate catalysts for ORR or OER can also contrast singlet oxygen. Co_3O_4 solid nanoparticles deposited on a carbon nanotubes cathode, for instance, alters

the nature of the discharge products, as well as their morphology and electronic structure, with the net result of suppressing large part of $^1O_2$ detected by EPR spectroscopy[168]. The authors came to the conclusion that this is related to the presence/formation of LiO_2-like species after discharging or during the first stages of charging. In general, solid catalysts can reduce the overpotentials during charging by enhancing the charge transfer through the discharge products phase or by accelerating the kinetics of Li_2O_2 de-lithiation. Central role of superoxide, either by direct oxidation or by disproportionation.

1.3 Redox mediators

1.3.1 Mechanisms of mediated oxidation

As detailed in section 1.1.3, peroxides are generally the favored discharge product in lithium-oxygen batteries, being formed through either the mechanism of eqs. (1.3), the "surface route", and (1.4), the "solvent route". This two-electron reduction, $O_2 \rightarrow O_2^{2-}$, is positively regarded for it guarantees a large battery capacity. The serious drawback is that peroxides form an insulating deposit over the cathode surface. Lithium peroxide is an insulator with a band-gap of 4-5 V, which clearly hinders the efficient transport of electrons that is needed during charging. The characteristic morphology of the deposited peroxide is also a relevant factor. The prevalence of one or the other of the growth modes, i.e. as a thin film or as nano-sized particles, is supposedly related to which one of the solution/surface mechanisms is the dominant one. While a film-like growth causes a more severe electrical passivation of the cathode surface, an irregularly grown particulate of Li_2O_2 leads to a progressive clogging of the porous structure. This limits the mass transport of ions and oxygen[63,176], thus contributing to the sluggish OER and reduced capacity. Hence, the process of oxidizing the peroxide back to gaseous O_2, which is required during the charging of the battery, is seriously hampered and very large overpotentials are needed, often 1 - 2 V above the theoretical voltage threshold for Li_2O_2 oxidation. Not only this has a bad impact on the side of energy efficiency, because of high round-trip voltage hysteresis; also, it promotes the degradation of electrochemically unstable molecules, whose voltage stability window does not usually span up to the range of 4 - 5 V vs Li^+/Li. Such an increased degradation leads, in turns, to the deposition of more insulating side-products, thus triggering a vicious circle of cascading adverse effects which definitively hamper any long-term cyclability of the cells. For this reason, solutions have been devised, on both the chemical and the manufacturing sides, in order to minimize as possible the problem of charging overpotentials.
The addition of redox catalysts, both heterogeneous or homogeneous, has been the most

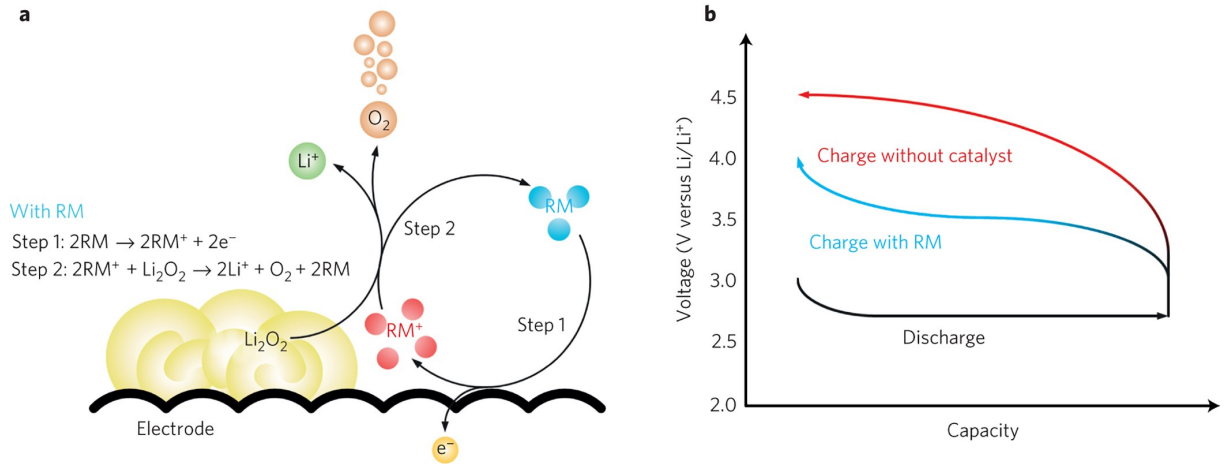

Figure 1.9: The oxidation mechanism assisted by redox mediators. On the left: reaction scheme, showing the cyclic regeneration of the mediator passing through the reduced RM (blue circles) and oxidized RM^+ (red circles) forms. On the right: voltammogram showing the the typical voltage profiles when charging a LOB with and without redox mediators. Reproduced from ref.[177].

investigated strategy. Heterogeneous electrocatalysts are loaded onto the cathode substrate, with the aim of enhancing the charge transport through the Li_2O_2 passivating layer and/or the delithiation kinetics. Many transition metal oxides have displayed good catalytic activity when decomposing Li_2O_2 at charge[178]. The drawback is that they also induce parasitic reactions, leading to additional side-products and to the decomposition of the electrolyte[179,180]. Redox mediators instead are homogeneous catalysts with good solubility in the electrolyte phase. They act as a shuttle for the electrons from the electrode to the discharge product, at a lowered voltage, as described by the following equations (where it is assumed, for simplicity, a mediator exchanging one single electron):

$$RM \longrightarrow RM^+ + e^- \tag{1.22}$$

$$2\,RM^+ + Li_2O_2 \longrightarrow 2\,RM + O_2 + 2\,Li^+ \tag{1.23}$$

The redox mediator (RM) is added to the electrolyte in its reduced form. As a first step in the charging process, the RM is electrochemically oxidized according to its own redox potential (eq. 1.22). This oxidized form of the RM is then able to chemically react with the alkali peroxide by spontaneous electron-transfer, to release molecular oxygen and return to its reduced form (eq. 1.23). As a result, the overall redox potential of the OER now is solely determined by that of the RM^+/RM couple, which can be chosen to fulfil specific requirements. For instance, the oxidized RM^+ should be able to read-

ily attack both surface agglomerates and detached particles in solution, and also provide a high Coulombic efficiency[181]. The optimal RM for LOBs has been searched among many different chemical classes. Among the more frequently cited, organic heteroaromatics (tetrathiafulvalene, TTF, 5,10-dihydro-5,10-dimethyl phenazine, DMPZ), oxyl radicals ((2,2,6,6-tetramethylpiperidin-1-yl)oxyl, TEMPO, 1-methyl-2-azaadamantane-N-oxyl, MAZO), aliphatic hydrazines (1,1'-bipyrrolidine, BP55, 1,1'-bipiperidine, BP66), phenyl amines (tris[4-(diethylamino)phrnyl]amine, TDPA, N,N,N',N'-tetramethyl-p-phenylenediamine, TMPD), quinones (2,5-di-tertbutyl-1,4-benzoquinone, DBBQ) halide salts (LiI, LiBr) and iron metalorganics (ferrocene, Fc, iron phtalocyanine, FePc). In order to chemically decompose Li_2O_2, the RM has to be oxidized at a voltage higher than 2.96 V, which is the theoretical formation voltage of lithium peroxide according to the half-reaction:

$$O_2 + 2\,Li^+ + 2\,e^- \longrightarrow Li_2O_2 \tag{1.24}$$

However, for maximizing the energy efficiency, the RM^+/RM potential would be required to be only slightly above that threshold. So, the optimal window for the redox potential is expected to lie somewhere between 3 and 4 V (vs Li^+/Li)[177,182]. Though, as shown by Kwak et al.[183], a high round-trip energy efficiency has no direct correlation with the catalytic efficiency of Li_2O_2 decomposition, as measured for example by O_2 gas evolution. Hence another crucial requisite of the RM is its chemical stability in the Li-O_2 cells. Stability towards reduced oxygen species (Li_2O_2, O_2^-) usually is not a major concern; singlet O2, instead, has been found to react with many organic mediators like TTF, DMPZ and PPT[183]. As an electrophilic specie, $^1O_2$ is supposed to act as an enophile or dienophile with the electron-rich C=C double-bonds of TTF and DMPZ, respectively[132], forming reactive ROOH, ROO· and R· intermediates that can in turn propagate the side reactions and lead to a wide spectrum of by-products. This kind of reactivity is found to affect the reduced form RM much more than the oxidized RM+ one, because of the different electron-richness of the two substrates. The chemical inertness of both the RM/RM^+ forms with respect to the different electrolytes has also been addressed[177]. At the same time, metal anodes showed to be reactive substrates for halogen-based mediators, thus calling for solutions based on separators or protective membranes[184].

The choice of the ideal redox potential of the selected RM needs to take into account the many processes taking place in the RM-free cell during charging. During pure electrochemical oxidation of the discharge products, the evolution of harmful $^1O_2$ was reported upon 3.5 V (vs Li^+/Li), so that to avoid the most of parasitic reactions, RM couples should better activate below this threshold. Anyway, the decomposition of carbonate side-products (like

Li_2CO_3) is also important for the efficiency and cycle-life of the battery. The electrochemical potential for the decomposition of lithium carbonate to CO_2 and O_2 is 3.8 V, and above this voltage CO_2 evolution is usually detected together with significant amounts of $^1O_2$ (see section 1.3.3). When the charging voltage goes as high as 4.2-4.6 V, the evolution of H_2 gas is triggered in some cases[119,165]. This happens because to side-reactions occurring at the cathode and involving electrolyte solvents which result to be unstable towards H-abstraction[99,185].

The number of studies about RMs for aLOBs has seen an outstanding increase across the last decade. Nevertheless, the research in this field is still significantly slowed down because of the very many variables which have to be accounted for, in order to project the results of single experiments outside the narrow range of validity dictated by specific choices of cell setup and operating conditions. As pointed out by Dou et al.[186], at present "the general principles of seeking and designing a new type of RMs remain a mystery". In general terms, the sequence of necessary experiments to fulfil this goal may be rationally reduced with a combination of computational screening procedures, an approach which is being applied increasingly more often in the field of materials for electrochemistry. An example of screening of suitable RMs by means of a computational scheme is given in ref.[177]. For several organic mediators, the chemical stability in TEGDME solvent was estimated on the on the basis of the HOMO and LUMO energies of donor/acceptor couples. Regardless of the validity of this choice of parameters, it is clear that many other parameters need to be taken into account in order to simultaneously screen different aspects like stability, transport properties and catalytic activity. This suggests that big steps forward still have to be taken in that direction.

1.3.2 Implications of RMs in $^1O_2$ release

The problem of singlet oxygen evolution is a major issue observed during charging of Li-O_2 batteries. In absence of redox mediators, the voltage is easily seen to raise well above 3.5 V, where $^1O_2$ formation is thermodinamically favorable and the excited state product is consequently detected. In principle, the use of RMs is expected to affect the $^1O_2$-induced parasitic reactivity only by anchoring the charging voltage to the redox potential of the RM^+/RM couple. Actually, this means neglecting the interaction of produced $^1O_2$ with the RM itself, as well as any direct involvement of the mediator's reactions in the production of $^1O_2$. As briefly discussed in the section (1.3.1), singlet oxygen is able to react with some electron-rich organic RMs trough "ene" or "diene" addiction, leading to the progressive deactivation of the redox catalytic action. On the other hand, many RMs

have been found to behave as singlet oxygen quenchers[182,187], thus directly suppressing the singlet oxygen reactivity without the need for an apposite quenching additive. Efficient $^1O_2$ quenchers, in fact, may suffer the limitations of a narrow electrochemical stability window, like the DABCO which is irreversibly oxidized over 3.6 V[118]. The problem can be mitigated through the joint use of a RM and a quencher[188], but a simpler solution would be to use a same chemical in order to obtain both of the effects[189]. Iodine, for instance, has a high quenching rate, tentatively ascribed to the heavy atom mass, thus yielding low $^1O_2$ despite a redox potential > 3.5 V[182]. Liang et al.[187] also attributed relevant quenching abilities to LiBr, AZADO, TDPA and TEMPO. The authors of this work proposed a reaction mechanism which unifies the catalytic oxidative activity and the suppression of singlet oxygen. They hypothesize that the oxidized RM forms an intermediate complex with the reduced substrates (for example, O_2^- as in eq. 1.25), which can undergo a spin transition suppressing the release of singlet spin-multiplicity products:

$$RM^+ + O_2{}^- \longrightarrow {}^1[RM{-}O_2] \longrightarrow {}^3[RM{-}O_2] \longrightarrow RM + {}^3O_2 \tag{1.25}$$

For this mechanism to take place, an intersystem crossing has to occur between a high-energy singlet and a low-energy triplet electronic states. This would explain the $^1O_2$ suppression by LiI and, to a lesser extent, by LiBr: their high atomic mass would in fact be sufficient to support the occurrence of large spin-orbit couplings. For the organic RMs, mostly made up of light-element atoms, this does not hold; hence, a vibronic spin-orbit coupling has to be invoked, where the presence of specific functional groups would be a key factor in promoting significant spin transition rates.

In addition to the interaction or reactivity with the singlet O_2 already present, the possible implication of redox mediators in its formation was also discussed. Petit et al.[182] pointed out that, with most of RMs, the mediated oxidation must follow a mechanism where the contribution of one-electron transfers is overwhelming with respect to a direct two-electron oxidation (i.e. from peroxide to O_2, whether triplet or singlet). Thus, partially oxidized superoxide species, either free $LiO_{2(solv)}$ or mixed $Li_{(2-x)}O_2$ solid phases, must form:

$$Li_2O_2 + RM^+ \longrightarrow Li^+ + RM + LiO_2 \tag{1.26}$$

As more charge is transferred from the peroxide to form superoxides, the disproportionation reaction can be triggered and this can lead, as argumented in section XX, to the release of singlet oxygen, even when the redox potential RM+/RM is well below 3.5 V, so that electrochemical oxidation to produce $^1O_2$ would be thermodinamically unfeasible. The

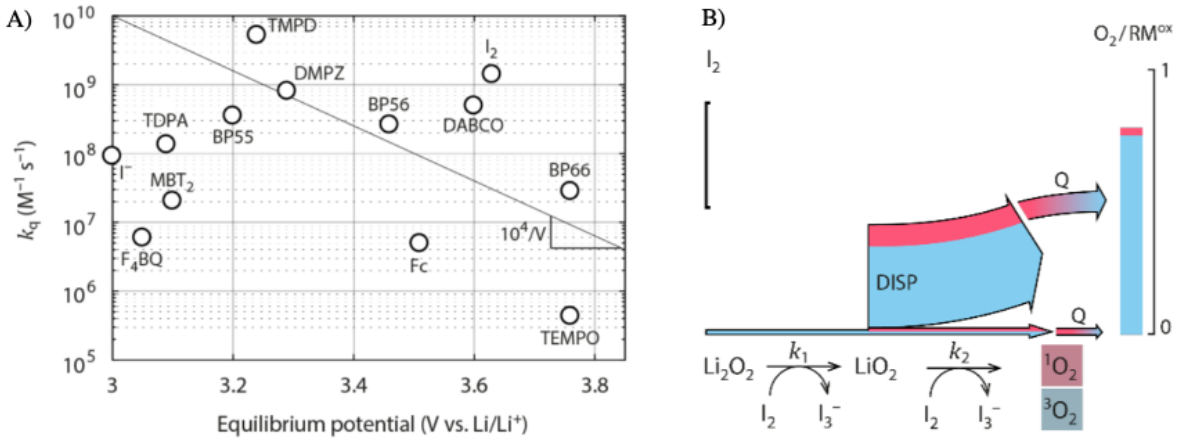

Figure 1.10: Involvement of redox mediators in singlet oxygen release. A) Quenching rate constants of several mediators toward $^1O_2$. B) Relative kinetics of Li_2O_2 oxidation steps and $^1O_2$ yield. The width of the arrows is proportional to the rate (Sankey plots). Reproduced from ref.[182].

competition between the kinetics of the two processes leading to free molecular O_2, namely, the superoxide oxidation and the superoxide disproportionation, is then recognized to be a key factor in determining the release of $^1O_2$. Accordingly, the authors found out that the disproportionation kinetics is slowed down for RM+/RM potentials > 3.2 V, hence the minimum $^1O_2$ release was detected inside the 3.2 - 3.5 V window.

1.3.3 Halogen/halide mediators

Redox mediators based on the different oxidation states of halogens were among the first solutions to be studied for the overpotentials issue in Li-O_2 batteries[190–192]. The RM is typically added into the electrolyte in its reduced form as salts, LiI or LiBr. These RMs are economic, easily soluble in common solvents, and do not suffer side-reactions with $^1O_2$[191], displaying prolonged stability upon repeated cycling[193]. Apart from organic RMs, most of studies so far have been focused on iodine-based mediators, with a less accent on bromine. Only a minor interest has been put on chlorine, although recent results seem to raise the potentiality of LiCl additive for promoting the decomposition of the discharge products[194]. For LiI and LiBr, the chemical nature of the active redox species is not unambiguously determined, as it seems to be heavily dependent on the specific choice of solvent, salt concentration, electrode, voltage and current density. Pande and Viswanathan[195] have discussed how the solvating properties of the electrolyte solvent should influence the redox potential for different kinds of redox couples. Their analysis is based on two considerations:

a) the anionic forms of the RM interact more strongly with solvents or salt counter-anions showing a large Gutmann acceptor number (AN, which quantifies the Lewis acidity), while its neutral forms are much less sensible to a change in the AN, and b) for anions, the effect of a large or small AN of the solvating species is more pronounced the more the charge is localized. Hence, in the case of the I_2/I^- redox couple, an increase in the AN of the electrolyte will establish a stronger interaction with the reduced form (I^-), rather than with the oxidized one (I_2), so that the lowering in the Gibbs free energy of the former is more pronounced; the ΔG of the reduction semi-reaction is then increased, and so is the oxidizing power of the couple. The same should apply only qualitatively for the I_3^-/I^- couple; in this case, the different stabilization of the two species will be only due to the -1 charge of I- being more localized than in I3-, so the increase of oxidizing power with higher AN is expected to be less pronounced (for example, DMSO=19.3 and G4=10.5). As a matter of fact, the experimental literature, although vast, is still controversial about the reaction mechanism of LiI redox mediator, and the identity of the effective oxidizing species is debated. In particular, different authors came to disagreeing conclusions about whether it is I_2 or I_3^- to be the most oxidized iodine species formed during Li-O_2 charging[196–198]. They are generated starting from iodide:

$$3\,I^- \longrightarrow {I_3}^- + 2\,e^- \tag{1.27}$$

$$2\,{I_3}^- \longrightarrow 3\,I_2 + 2\,e^- \tag{1.28}$$

The two species I_2 and I_3^-, once electro-generated, are then both able, in principle, to oxidize Li_2O_2, since both the redox couples I_2/I_3^- and I_3^-/I^- have a redox potential higher than O_2/Li_2O_2 (around 3.3 V and 3.0 V, respectively, in ref.[199]):

$$Li_2O_2 + {I_3}^- \longrightarrow 2\,Li^+ + O_2 + 3\,I^- \tag{1.29}$$

$$Li_2O_2 + 3\,I_2 \longrightarrow 2\,Li^+ + O_2 + 2\,{I_3}^- \tag{1.30}$$

Nakanishi et al.[199] investigated the effect of varying electrolyte compositions on the oxidizing power of the two species I_2 and I_3^- towards Li_2O_2. I_2 was found to be the most active oxidizer in a tetraglyme/LiTFSI electrolyte, at all concentrations of the salt, while the reactivity of I_3^- was negligible. A similar inactivity of I_3^- as an oxidant was also previously reported in refs.[196,197]. Higher polyiodides (e.g. I_5^-, I_7^-, ...) were also shown to have little to no relevance. Switching to DMSO as a solvent, the increased stabilization of the small iodide anion deeply affects the redox potential of the I_3^-/I^- couple, shifting it to more pos-

itive values. In fact, in the LiTFSI 1.0 M electrolyte I_3^-/I^- turns to be the effective redox couple, with almost no formation of I_2. However, when the salt concentration of the salt is raised to 2.8 M, the oxidative power of I_3^- is drastically reduced, for both thermodynamic and kinetic reasons, while the majority ot the current is carried by the I_2/I_3^- redox couple again. Conversely, the potential of the I_2/I_3^- is reported by Leverick et al.[200] to be largely solvent-independent, because both of the species are weakly solvated. These last authors also extended the range of solvent tested, and the redox potential of I_3^-/I^- was confirmed to shift positively moving from DME to DMA to DMSO, with increasing oxidizing power. The superior oxidant activity of I_2 in TEGDME solvent was also confirmed by Li et al.[201], who attempted to simplify the redox chemistry of iodine by introducing a chelated form of the iodide salt, LiI(hydroxipropionitrile)$_2$. This way, the dissociation of the salt is lowered, if compared to LiI, in such a way that the free iodide concentration remains low and the oxidized RM is all I_2 and almost no I_3^-, with improved the oxidation efficiency. From the evidences reported above, it is clear that the very specific combination of cell setup and operating conditions plays a decisive role, from case to case. This unavoidably complicates the hard task of devising a unified mechanism for the understanding of iodine RMs complex activity in Li-O_2 batteries.

Another topic that has been at the center of the discussion about iodine-based redox mediators is the nature of the discharge products. Many authors have reported the presence of LiOH as an additional product after discharging a Li-O_2 battery in presence of LiI redox mediator[202]. LiOH is insoluble in most of the commonly employed aprotic solvent. When compared to Li_2O_2, it shows higher ionic and electronic conductivity[194], a better filing of the macroporous structure of the electrode[192], leading to an improved capacity, and the battery is able to tolerate larger amount of water. Despite these benefits, the formation of solid LiOH could represent a formidable obstacle for an efficient battery cycling. In fact, according to ref.[200], the oxidized iodide may be involved in heterogeneous side-reactions with LiOH leading to the formation of $LiIO_3$-like species, which are insoluble and hence deactivate the RM without evolution of O_2. However, the formation of LiOH has been showed to be strongly related to the presence of even trace amounts of water when adding LiI[203], which occurs because of very strong interactions between water molecules and I^- anions. When a very careful procedure for keeping the environment as anhydrous as possible, no LiOH is observed in the discharge products[199].

Bromine is known to be a stronger oxidant than iodine. LiBr can be oxidized to Br_3^- and Br_2, according to the two semireactions:

$$3\,Br^- \longrightarrow {Br_3}^- + 2\,e^- \tag{1.31}$$

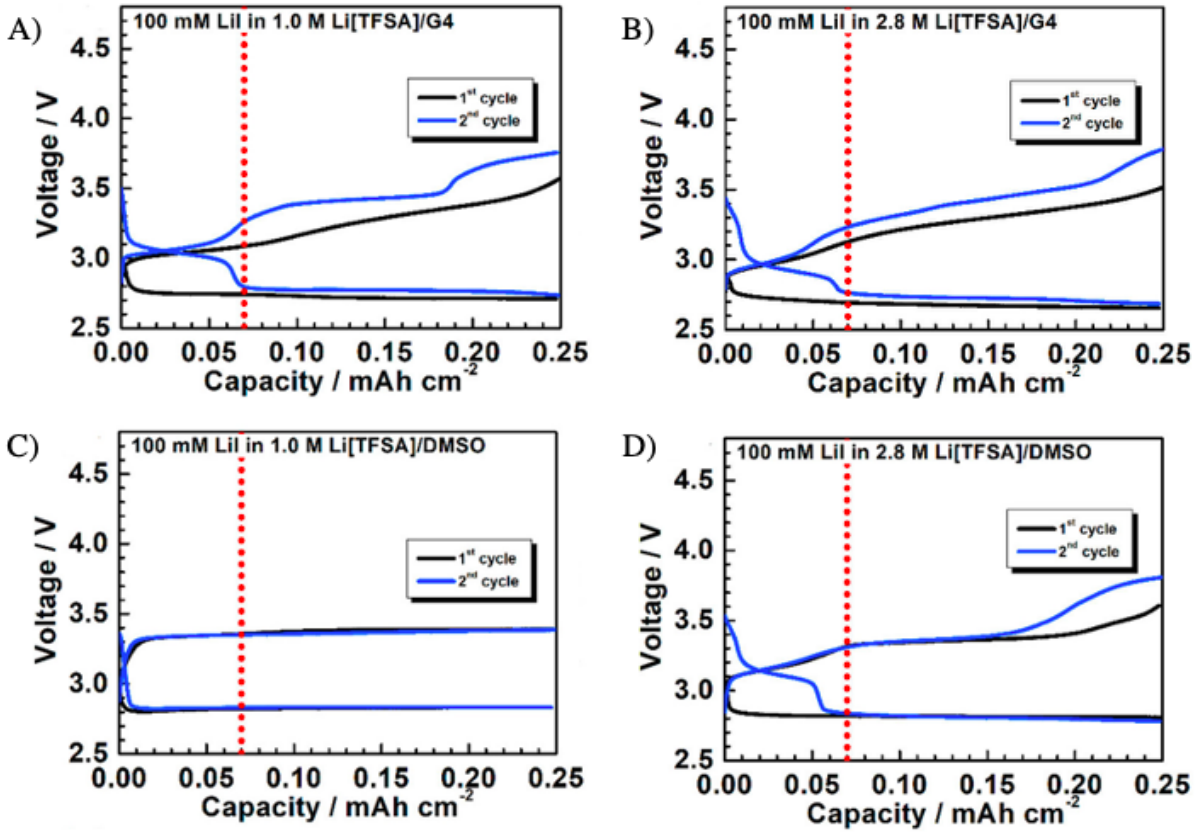

Figure 1.11: Cyclic voltammetry (first two cycles) of LiI redox mediator in Li-O_2 batteries with containing: A) 1.0 M Li[TFSA] in G4; B) 2.8 M Li[TFSA] in G4; C) 1.0 M Li[TFSA] in DMSO; D) 2.8 M Li[TFSA] in DMSO . The two plateaus are tentatively assigned to the oxidation of I^- to I_3^- and of I_3^- to I_2. Reproduced from ref.[199].

$$2\,Br_3^- \longrightarrow 3\,Br_2 + 2\,e^- \tag{1.32}$$

whose redox potential is, respectively, about 3.5 V and 4.0 V (vs. Li^+/Li, in diglyme/LiTFSI 1M[185]). With the Br_2/Br_3^- couple operating only at such a high voltage, the redox chemistry of LiBr inside the cell should be easier to understand, if compared to LiI. Anyway, due to this relatively high voltage, the use of LiBr mediators is found to be effective also in promoting the decomposition of Li_2CO_3, which is one of the common discharge by-products. For instance, Liang et al.[185] noticed that CO_2 gas evolution started at 3.9 V during LiBr-assisted charging, in contrast with the value of 4.3 V observed in the same cell iwithout RMs. Another attractive reason for riding the way of LiBr is the enhanced chemical stability of bromine species (over iodine) towards nucleophilic attack by reduced-oxygen intermediates[186]. Moreover, the major discharge product in presence of LiBr is

always Li_2O_2, without significant amounts of LiOH, even in presence of water inside the electrolyte[186,204]. As a downside, the onset of 3.5 V where the Br_3^-/Br^- redox couple is expected to activate as redox mediator system is close to the known threshold of singlet O_2 evolution by electrochemical oxidation of Li_2O_2, which is expected to hold until Br^- starts to get oxidized.

Interestingly, as opposed to organic RMs, halogen/halide RMs offer the opportunity to design new mediators upon mixing. It has been recently advanced by Leverick et al.[205] that the properties, and in particular the oxidizing power of the RM system, can be tuned by interhalide compounds obtained by simply mixing LiI, LiBr and LiCl salts directly into the electrolyte. The formation of interhalide XY_2^- compunds was confirmed by comparing Raman spectroscopy and DFT calculated spectra. The appealing characteristic of these compounds is that they show, as expected, intermediate redox potentials between those of the Br_3^-/Br^- and I_3^-/I^- couples, as well as a tunable oxidizing power towards Li_2O_2 and LiOH. Consistently with the higher potentials of the bromine redox couples, the oxidizing power is seen to increase with increasing Br content in the I-Br interhalide mixture.

Chapter 2

Theory and Methods

This chapter presents a brief recap on the basics of molecular electronic structure theory and their applications in the computational quantum chemistry methods that have been used for the research work of this thesis. The concepts of single-reference SCF wave function and electron correlation are first introduced. Methods for recovering the correlation energy are then presented, putting an emphasis on the problem of static correlation in single-reference theories. Multiconfigurational computational methods are then discussed, presenting only the conceptual key points and without deepening in mathematical derivations. The section is closed by a short introduction on implicit solvent models and the nudged elastic band method, which were usefully adopted in our calculations.

2.1 Electronic structure methods

2.1.1 Single-determinant wave functions and electron correlation

For a molecular system containing N electrons and M nuclei, the total non-relativistic energy is determined by its Hamiltonian operator (in atomic units):

$$\hat{H} = -\frac{1}{2}\sum_{i=1}^{N}\nabla_i^2 - \frac{1}{2}\sum_{A=1}^{M}\frac{1}{M_A}\nabla_A^2 - \sum_{i=1}^{N}\sum_{A=1}^{M}\frac{Z_A}{r_{iA}} + \sum_{i=1}^{N}\sum_{j>i}^{N}\frac{1}{r_{ij}} + \sum_{A=1}^{M}\sum_{B>A}^{M}\frac{1}{R_{AB}} \tag{2.1}$$

Under the Born-Oppenheimer approximation, which allows for a factorization of the total wave function, a complete separation can be made between the electronic and the nuclear coordinates in the system. The previous expression then reduces to the electronic

Hamiltonian:

$$\hat{H}_{el} = -\frac{1}{2}\sum_{i=1}^{N}\nabla_i^2 - \sum_{i=1}^{N}\sum_{A=1}^{M}\frac{Z_A}{r_{iA}} + \sum_{i=1}^{N}\sum_{j>i}^{N}\frac{1}{r_{ij}} \equiv \hat{T} + \hat{V}_{Ne} + \hat{V}_{ee} \tag{2.2}$$

Solving the Schrödinger equation $\hat{H}_{el}\Psi_{el} = E_{el}\Psi_{el}$ with the differential operator of eq. 2.2, however, is a mathematically unmanageable problem for all but the simplest of the molecular systems. The reason for this lies in the non-separability of the electronic coordinates inside the $\hat{V}_{ee}$ potential energy term. Owing to the Coulombic operator acting at every instant between two charged particles, the electronic positions are mutually dependent, and no methods are available to analytically evaluate terms depending on $1/r_{ij}$ for multi-electron systems.

The most widely used approach for treating the electron-electron potential energy consists in considering the electrons as non-interacting: this allows to replace the instant Coulombic repulsion of the $1/r_{ij}$ operator with an interaction between any individual electron with the average charge distribution of each of the remaining N-1 electrons. The total wave function Ψ is consequently represented as factorized into N single-particle eigenstates, the spin-orbitals ϕ_i and, owing to the anti-symmetry requirements, it finally takes the well-known form of a Slater determinant:

$$\Psi_0 = \frac{1}{\sqrt{N!}}\begin{vmatrix} \phi_1(\vec{x}_1) & \phi_2(\vec{x}_1) & \cdots & \phi_N(\vec{x}_1) \\ \phi_1(\vec{x}_2) & \phi_2(\vec{x}_2) & & \phi_N(\vec{x}_2) \\ \vdots & & \ddots & \vdots \\ \phi_1(\vec{x}_N) & \phi_2(\vec{x}_N) & \cdots & \phi_N(\vec{x}_N) \end{vmatrix} \tag{2.3}$$

When the Slater determinant of eq. (2.3) is used as the trial wave function, the expectation value of the electronic Hamiltonian becomes:

$$E_{HF} = \langle\Psi_0|\hat{H}|\Psi_0\rangle = \sum_{i}^{N}\langle\phi_i|h|\phi_i\rangle + \frac{1}{2}\sum_{i}^{N}\sum_{j}^{N}[\langle\phi_i\phi_i|\frac{1}{r_{12}}|\phi_j\phi_j\rangle - \langle\phi_i\phi_j|\frac{1}{r_{12}}|\phi_j\phi_i\rangle] \tag{2.4}$$

The optimal spin-orbitals ϕ_i are determined in a variational fashion by iteratively solving the set of coupled eigenvalue equations of the Fock operator $\hat{f}\phi_i = \epsilon_i\phi_i$, until a convergence criterion is satisfied. In the practice, this is accomplished by expanding the spin-orbitals

over a basis of M well-behaving functions, the basis set:

$$\phi_i = \sum_a^M c_{ia}\chi_{ia} \tag{2.5}$$

By this definition, the search for the optimal molecular orbital (MO) functions is replaced by the search for the optimal coefficients c_{ia} and efficient matrix algebra operations in an M-dimensional vector space can be exploited. Since the Fock operator is itself dependent on the spin-orbitals, the average field in which the electrons move is adjusted at each iteration, and the whole iterative procedure is called *self-consistent field* method (SCF).
Summing up, Hartree-Fock method approximates the wave function assuming that it can be represented by just one single Slater determinant, and neglects electron correlation by replacing instantaneous electron-electron repulsion with the repulsion between electronic averaged clouds. Accordingly, the *correlation energy* is defined as the difference between the true (non-relativistic) energy and the Hartree-Fock energy, in the complete-basis limit. When this deviation from the true energy is ascribed to the lack of instantaneous correlation between the motions of electrons, this is referred to as *dynamical* correlation. Sometimes a large difference from the exact energy is also due to the state of the system not being suitably represented by a single electronic configuration, typically because of near-degeneracy phenomena; in this case we speak of *static* (or *strong*) correlation.

2.1.2 Basis sets and Density fitting

Basis sets allow to expand the spin orbitals in the Slater determinant over a batch of fixed functions (eq. 2.5), of arbitrary size. Historically the most widely used type of basis functions for performing numerical calculations on atoms and molecules are the gaussian-type orbitals (GTOs), that is, functions of the form:

$$g_i(r) = \sqrt{\frac{(8\zeta)^{l_x+l_y+l_z} l_x! l_y! l_z!}{(2l_x)!(2l_y)!(2l_z)!}} \left(\frac{2\zeta}{\pi}\right)^{3/2} x^{l_x} y^{l_y} z^{l_z} e^{-\zeta r^2} \tag{2.6}$$

In order to reduce the number of functions that must be handled during the calculation, groups of gaussian functions (*primitive* GTOs) can be contracted to form linear combinations with fixed and unmutable coefficients (*contracted* GTOs). Even if molecular electronic integrals involving primitive GTOs still have to be evaluated, the use of contractions allows to greatly reduce the size of the calculations, because the time of the SCF method scales on the total number of CGTOs. Split-valence basis sets allocate only one shell of GTOs to

each atom to model its core-electrons charge density, while two or more shells are allocated for the valence electrons, which require more flexibility in order to correctly reproduce the charge fluctuations associated with chemical bonding and weak interactions. A basis with two, three or four valence shells will then be called a double-, triple- or quadruple-ζ basis set. Extra functions can also be added in order to provide a more flexible basis. Polarized basis sets include an additional shell of GTOs with higher angular momentum than the valence shell (*polarization* functions), which is almost always needed for an accurate description of bondings. Augmented basis sets have additional GTOs with a very small α exponent (*diffuse* functions), useful for example with anions whose charge density exhibits a slow radial decay.
Two-electron integrals like in the last term of eq. (2.4) are required in SCF and post-SCF calculations. Their handling can represent a bottleneck in the calculation, particularly when it comes to transforming them from the atomic orbitals basis to a molecular orbitals representation. An alternative way to treat those integrals is to use *density fitting* (note: in most of the quantum chemistry codes, density fitting is often referred to as *resolution of identity*, RI). Basically, two-electron four-center integrals can be expressed in terms of reduced density matrix elements:

$$(pq|rs) = \int dr_1 \int dr_2 \phi_p(r_1)\phi_q(r_1)\frac{1}{r_{12}}\phi_r(r_2)\phi_s(r_2) = \int dr_1 \int dr_2 \rho_{pq}(r_1)\frac{1}{r_{12}}\rho_{rs}(r_2) \quad (2.7)$$

and these densities can be approximated by fitting over an auxiliary set of basis functions:

$$\bar{\rho}_{pq}(r) = \sum_{P}^{N_{fit}} d_P^{pq}\chi_P(r) \quad (2.8)$$

where the χ_P are the auxiliary functions and the d_P^{pq} are the fitting coefficients. These latter are then expressed as sum over three-center integrals, which globally require less memory and are significantly cheaper to evaluate. In fact, despite the intensive floating-point operations required for the fitting, this is still remarkably faster than the massive I/O operations needed when handling the 4-center integrals. As an example, through density fitting the 4-index transformation of two-electron integral from the AO to the MO basis goes from formally scaling as N^5 to scaling as N^4.

2.1.3 Post-Hartree-Fock methods

The HF wave function can be used as a reference for further calculations (post-HF methods) aiming at recovering the dynamic correlation energy. A straightforward way to lower the

energy of the HF wave function is to substitute the ground-state Slater determinant Φ_0 with a linear combination of determinants built from the same set of MOs:

$$\Psi_{CI} = c_0\Phi_0 + \sum_k c_k\Phi_k \tag{2.9}$$

These are "excited" determinants (Φ_k), built by promoting electron from occupied orbitals of the HF solution to unoccupied (virtual) orbitals. The variational optimization of the linear expansion coefficients c_i goes under the name of *configurations interaction* method (CI). The expectation value $\langle\Psi_{CI}|\hat{H}|\Psi_{CI}\rangle$ displays a slow convergence toward the exact energy, for an increasing number of excited determinants included in the summation of eq. (2.9). Therefore, for practical calculations it is absolutely mandatory that the MOs, which are used to build the basis of Slater determinants, be such to give the best single-determinant representation of the ground-state of the system. CI methods typically include a number of determinants in eq. (2.9) only up to a given order of electronic excitations (eg. singly, doubly or quadruply excited determinants). Conversely, the inclusion of all possible determinants, of any order of excitations, is called full-CI, and it is guaranteed to converge to the exact energy of the system, but only inside the limits imposed by the finite size of the basis set.

An alternative approach for including the correlation energy is offered by many-body perturbation theory (MBPT). The central idea is to use as reference a Schrödinger equation (the unperturbed system), for which the solutions are known, to obtain approximate solutions to another equation (the perturbed system), assuming that the solutions of the two equations are close "enough" in some sense. If $\hat{H}_0$ is the unperturbed Hamiltonian, whose eigenfunctions are already known, and $\hat{H}'$ is a "small" perturbation, then the perturbed Hamiltonian can be written as a combination of the two:

$$\hat{H}\Psi = (\hat{H}_0 + \lambda\hat{H}')\Psi = W\Psi \tag{2.10}$$

where λ is a parameter which determines the strength of the perturbation. The energy and wave function of the perturbed system described by the eq. (2.10) can therefore be expanded as Taylor series in powers of the parameter λ:

$$\begin{aligned} W &= \lambda^0 W_0 + \lambda^1 W_1 + \lambda^2 W_2 + \dots \\ \Psi &= \lambda^0 \Psi_0 + \lambda^1 \Psi_1 + \lambda^2 \Psi_2 + \dots \end{aligned} \tag{2.11}$$

Substituting eq. (2.11) into eq. (2.10) and collecting together terms with the same power

of λ, a set of n-th order perturbation equations are obtained, where the $(n-1)$-th order wave function is required in order to calculate the n-th order energy (hence the requisite of a known zeroth-order, unperturbed wave function). Möller and Plesset applied this general theory using the Hartree-Fock solution as the unperturbed wave function Ψ_0 and the sum of Fock mono-electronic operator as the unperturbed Hamiltonian. The perturber is then given by:

$$\hat{H}' = \sum_{i}^{N}\sum_{j>i}^{N}\frac{1}{r_{ij}} - \sum_{i}^{N}\sum_{j}^{N}\left\langle\frac{1}{r_{ij}}\right\rangle \tag{2.12}$$

where the second herm in the right-hand side represents the electron-electron repulsion operator in the Fock operator. Möller-Plesset theory has become very popular in its second-order solution (MP2), which gives the following correction for the correlation energy:

$$E_{MP2} = \sum_{i<j}^{occ}\sum_{a<b}^{vir}\frac{(\langle\phi_i\phi_j||\phi_a\phi_b\rangle\langle\phi_i\phi_j||\phi_b\phi_a\rangle)^2}{\epsilon_i+\epsilon_j-\epsilon_a-\epsilon_b} \tag{2.13}$$

MP methods are based on the assumption that the reference wave function, i.e. the HF Slater determinant, is a "good" representation of the ground-state. This means that these methods are excellent ways to recover a large portion of the dynamic correlation, but they are expected to fail whenever static correlation becomes relevant. This is quite often the case for excited-states and for molecular structures far from the geometry minimum, and in all those cases where more than one configuration is needed in order to give a qualitatively correct representation of the wave function.

2.1.4 Density Functional Theory

It can be demonstrated that all the terms inside the molecular Hamiltonian of eq. (2.2) stem from the information about the number of electrons and their spatial distribution. Based on this fact, a different approach to the calculation of the electronic energy can be adopted, that uses the electron density as the basic variable, thus giving up any required knowledge about the wave function. Hohenberg and Kohn demonstrated that, for a given ground-state electron density ρ, there exists only a unique external potential $\hat{V}_{ext}$ that fixes the Hamiltonian $H = \hat{T} + \hat{V}_{ee} + \hat{V}_{ext}$ in such a way to yield the correct density ρ. This external potential is then a unique functional of the density, and so is the total energy.
On a practical ground, the Kohn-Sham method provides an operative definition of such an external potential. A non-interacting system is taken as a reference, as in the Hartree-Fock

method, thus defining an Hamiltonian which is a sum of one-electron operators:

$$\hat{H} = \sum_{i=1}^{N} [-\frac{1}{2}\nabla_i^2 + v_s(\vec{r}_i)] \tag{2.14}$$

The eigenfunctions of these one-electron operators are the Kohn-Sham spin-orbitals (θ^{KS}), and their anti-symmetrized product forms a Slater determinant, as in HF theory. This Slater determinant represents the wave function of the reference (non-interacting) system and its electron density $\rho = \sum_i |\theta_i^{KS}|^2$ is assured to equal the exact electron density of the true (interacting) system, given that each electron moves under the effect of some appropriate potential v_s. The ground-state energy can therefore be evaluated from the density of the reference system:

$$E_0 = -\frac{1}{2}\sum_{i}^{N}\langle\theta_i^{KS}|\nabla_1^2|\theta_i^{KS}\rangle - \sum_{\alpha} Z_\alpha \int \frac{\rho(r_1)}{r_{1\alpha}} dr_1 + \frac{1}{2}\int\int \frac{\rho(r_1)\rho(r_2)}{r_{12}} dr_1 dr_2 + E_{XC}[\rho] \tag{2.15}$$

where the first term in the right-hand side is the kinetic energy of the non-interacting system, the second term is the electron potential energy due to the fixed nuclei, the third term is the potential energy due to the repulsion of the electronic clouds and the last term is the exchange-correlation energy. E_{XC} must include: the difference between the kinetic energy of the true system and that of the reference system (kinetic correlation energy), the difference between the electron-electron correlated energy and the averaged cloud-cloud interaction, and a correction for self-interaction due to the fact that the product of charge densities $\rho(r_1)\rho(r_2)$ also accounts for the repulsion of one electron with its own averaged charge. E_0 can be minimized variationally with respect to variations in the electron density ρ, hence in the KS orbitals. This leads to a rewriting of the KS operator in eq. (2.14) to give the self-consistent KS equations:

$$\left[-\frac{1}{2}\nabla_i^2 - \sum_{\alpha}\frac{Z_\alpha}{r_{1\alpha}} + \int \frac{\rho(r_2)}{r_{12}} dr_2 + v_{xc}(1)\right]\theta_i^{KS}(1) = \epsilon_1^{KS}\theta_i^{KS}(1) \tag{2.16}$$

where v_{xc} is the functional derivative of E_{XC} with with respect to the density:

$$v_{xc}(r) = \frac{\delta E_{xc}[\rho(r)]}{\delta\rho(r)} \tag{2.17}$$

The advantage of the non-interacting reference system introduced by Kohn and Sham is evident: the KS orbitals can be optimized variationally through the well established SCF procedure, the same already implemented in most codes which performs HF calculation,

which allowed DFT to rapidly gain a huge popularity. The drawback is apparent as well: no exact E_{XC} is actually known, and only approximation to its functional form can be used in practical calculations.
Approximate functionals can be approached either by analytical derivation or by fitting, and the latter is by far the most commonly adopted strategy. A gigantic amount of approximate functionals is available nowadays, which are usually classified according to a hierarchy based on how much physical information on the electron density is contained inside the expression for the exchange-correlation energy. In "pure" DFT functionals the E_{XC} term only contains physical information about the electron density. Functionals belonging to the local-density approximation (LDA) class solely depend on the value of the density itself at each point in space, while the generalized-gradient approximation (GGA) and meta-generalized-gradient approximation also include, respectively, first and second derivatives of the density. Hybrid functionals mix the exchange-correlation term from GGa or meta-GGA functionals with some amount of exact Hartree-Fock exchange. Double-hybrid functionals, finally, employ an hybrid functional definition for optimizing the KS orbitals, then introduce energy correction terms evaluated via MP2 perturbation theory.

2.1.5 Broken-symmetry solutions

When convergence is reached in the SCF procedure (both Hartree-Fock and Kohn-Sham methods[206]), the energy is stationary with respect to infinitesimal variations in the MOs composition. In order to represent a true minimum in the space of orbital coefficients, the Hessian matrix (that is, the matrix of second derivatives of the energy with respect to orbital variations) has to be positive-definite. When this condition does not hold, i.e. when the diagonalization of the Hessian yields at least one negative eigenvalue, the SCF solution is said to be "unstable". The presence of an instability means that a different solution, with lower variational energy, is guaranteed to exist. Finding this lower energy, stable solution may imply the removal of one or more of the constraints which are typically imposed during the SCF optimization of the MOs coefficients. The instability is then said to be "external"; the most common example of this kind of instabilities is the "triplet" instability, or RHF $\rightarrow$ UHF, which occurs when the energy of a closed-shell, restricted HF solution can be lowered by allowing an unrestricted HF solution to break the space symmetry of the α and β spin-orbitals[207]. In order to converge on such a solution an unbalanced guess must be provided from the beginning. Singlet diradical, for instance, can be represented in a single-determinant fashion by the spin-flip technique[208]: basically, it starts from a converged high-spin triplet solution and then rotates one singly occupied MO from α to β, and uses

this rotated orbitals as the initial guess for converging the UHF in a singlet multiplicity.

Not only these broken-symmetry solutions are not easy to converge toward a physically meaningful solution, but they also suffer from large spin contamination, because of the non-overlapping α and β corresponding orbitals[209]. While the spin-contamination problem may be mitigated by means of spin-projection procedures[210,211], the poor description of the multiconfigurational wave function remains a limiting issue, especially for the calculation of properties.

2.1.6 Multiconfigurational SCF

A system which presents (near-)degeneracy between different electronic configurations is intrinsically unsuitable to be represented by a single Slater determinant, as happens in HF and KS-DFT methods. The SCF procedure, in fact, optimizes the orbitals based on the field generated by the occupation numbers of just one single electronic configuration. Hence, such optimized orbitals are qualitatively wrong and cannot serve as an appropriate basis for electronic excitations in post-HF methods. The problem of near-degenerate configurations is tackled by the *multiconfigurational self-consistent field* method (MCSCF), where the optimal wave function is simultaneously parametrized over both the CI coefficients (eq. 2.18) and the orbitals parameters (eq. 2.19):

$$|\Psi_0\rangle = \sum_i C_{i0}|\Phi_i\rangle \tag{2.18}$$

$$\phi_r = \sum_a k_{ar}\chi_a \tag{2.19}$$

The most impactful choice on the outcome of an MCSCF calculation is the choice of the configurations that must be included into the expansion of eq. (2.18). Rather than a manual selection of individual configurations on the basis of qualitative considerations, the preferred way is actually to generate a large number of configurations by permuting electrons inside one or more spaces of active orbitals, eventually under some restrictions. In the *complete active space self-consistent field* (CASSCF), a space of active orbitals is defined such that all the possible electronic excitations are allowed among occupied and unoccupied orbitals belonging to the space (fig. 2.1). Occupations are kept frozen instead in the remaining orbital spaces, which are called inactive (n = 2) and virtual (n = 0) spaces. This way, the CI expansion grows as if a full-CI is carried out on the sole active-space. The

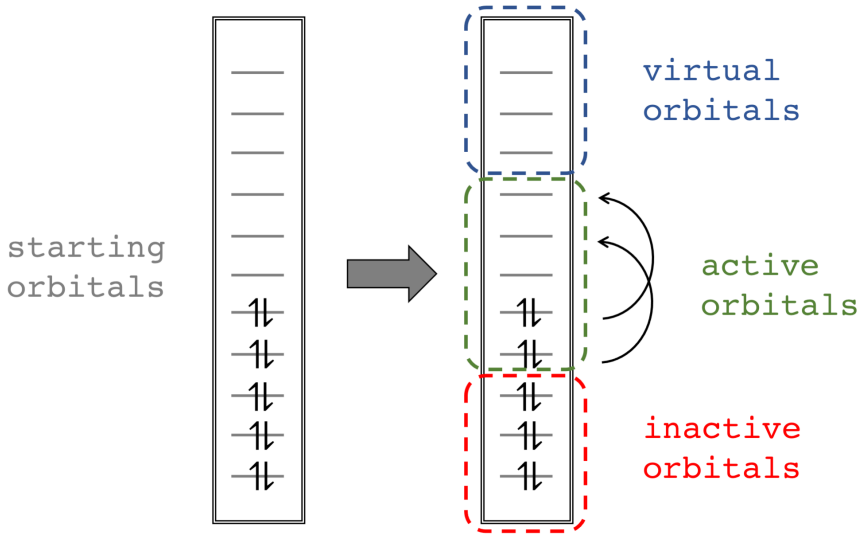

Figure 2.1: Partitioning of the orbital spaces in CASSCF. Inactive orbitals (red) have fixed n=2 occupation numbers; inside the active orbitals (green), all electronic excitations are allowed; virtual orbitals (blue) are kept unoccupied.

number of configurations is then given by:

$$N_{CAS} = \frac{2S+1}{m+1}\binom{m+1}{\frac{N}{2}-S}\binom{m+1}{\frac{N}{2}+S+1} \tag{2.20}$$

where N and m are the numbers of electrons and orbitals in the active space, respectively, and S is the total spin. Despite the very large number of configurations, in many cases very few of those assume a large weight in the total wave function, so CASSCF is often good for visualizing chemical states in terms of orbital occupancies, as it may be in the case of electron transfer reactions, where reactant and product states differ for a ± 1 electron in the donor and the acceptor orbitals[212]. The CAS scheme, however, doesn't solve by itself the problem of the choice of the more significant configurations. The stability of the active space is indeed very sensible to the choice of the orbitals that compose it. Ideally, when studying a chemical process, the active orbitals should be able to represent all of the chemically relevant features of the process, eventually taking into account the involvement of more than one state. The CASSCF method is in fact widely used for calculations over excited-state. In a *state-averaged* CASSCF, the optimization of eqs. (2.18) and (2.19) is carried out simultaneously for an arbitrary number of roots. This means that a common set of CAS natural orbitals is shared among all of the computed states. SA-CASSCF is often

an indispensable resource when calculating excited states, because the convergence on a single higher-root can be extremely difficult. Moreover, a significant benefit of this method over TD-DFT is that either the ground- and the excited-states energies are all computed at the same level of accuracy.

2.1.7 Multireference correlation

Because of the factorial scaling behaviour in eq. (2.20), active spaces in CASSCF are usually kept as small as the chemistry of the system allows. In the general case, the CAS includes a number of configurations that is not sufficient to recover a large part of dynamical correlation, for its main purpose is instead that of providing a qualitatively correct representation of the true wavefunction. Hence, multireference (MR) correlation methods were developed in order to recover static and dynamical correlation at the same time. In multireference configuration interaction (MRCI) an MCSCF (typically CASSCF) solution is used as reference wave function, and excitations are allowed out of any reference configuration included in eq. (2.18). This corresponds to the so-called *uncontracted* MRCI, which is its most expensive formulation. Contracted methods are also available, where the coefficients of the expansion space are fixed according to several different schemes, saving significant computational time but at the cost of introducing some "contraction" error. In the very most of practical cases, the excitation scheme is truncated to the second order (i.e. only single and double excitations), which is indicated as MRCISD[213]. A typical problem of truncated CI expansions is the lack of size-consistency, which means that the energies of two separated systems don't sum up to the energy of the two systems at infinite distance. The size-consistency problem in MRCI can be mitigated by a-posteriori corrections, like the Davidson correction with unlinked quadruple excitations.

Due to its highly time-consuming performances, other multireference methods have been developed to to be used more routinely than MRCI. Multireference perturbation theory is an adaptation of the MBPT mentioned in sec. 2.1.3 that uses a multi-configurational reference as the unperturbed wavefunction. Different variants of MR-MBPT are available, which mainly differ for their definition of the zeroth-order Hamiltonian. The second-order complete active space perturbation theory[214] (CASPT2) adopts a CASSCF reference wave function and follows a definition of purely mono-electronic unperturbed Hamiltonian, similar to that of Möller-Plesset theory. CASPT2 has become a popular way to treat multiconfigurational systems at a high computational level, but has some drawbacks like the problem of intruder states, a poor size-consistency and the dependece of energies on IPEA shifts[215]. These problems are overcome in the n-electron valence state perturbation the-

ory[216] (NEVPT2), which employs a zeroth-order Dyall Hamiltonian[217] containing also two-electron terms. Similarly to the case of MRCI, contraction schemes were designed in order to save computation time[218]. Both CASPT2 and NEVPT2 methods can be applied sequentially as state-specific corrections to each root of a SA-CASSCF wave function. This approach typically produces very good vertical excitation energies[219]; nevertheless, there are situations where the CASSCF wave functions are qualitatively wrong due to the lack of dynamic correlation. This can produce, for instance, a wrong mixing of states which cannot be corrected by state-specific MR-MBPT. Multistate theories are then introduced, like multistate CASPT2[220] (MS-CASPT2) or quasi-degenerate NEVPT2[221] (QD-NEVPT2), where an effective Hamiltonian is diagonalized that is constructed over the basis of reference states. This approach yield improved energies and is usually able to restore the correct interaction/mixing of states.

2.1.8 Implicit solvation models

Modeling the effects of the environment is a fundamental task in the simulation of chemical processes and spectroscopy. For homogeneous systems in solution, this implies in first place modeling the solvent and accounting for its interactions with the solute. In many cases, the explicit inclusion of a large number of surrounding molecules into an ab-initio calculation is prohibitive, because of the very unfavorable scaling behaviour. As one of the possible solutions to this problem, approximation schemes have been introduced that only include the field effects of the solvating environment, without adding new atoms into the calculation. These methods go therefore under the name of *implicit solvent* models. The solvent is considered as a uniform polarizable medium with an assigned dielectric constant ϵ. The solute is placed inside a hole of suitable shape and surrounded by the dielectric medium. A typical way to construct the hole is to add the atomic spherical volumes given by the respective Van der Waals radii (eventually scaled). In the general scheme of implicit solvation, the free energy of solvation is separated into additive contributions:

$$\Delta G_{solv} = \Delta G_{elec} + \Delta G_{cav} + \Delta G_{disp} \tag{2.21}$$

The first terms in the right-hand side accounts for electrostatic interactions between the charge distribution of the solute and the dielectric medium, which also include their mutual polarization. The second term is an estimate of the energy destabilization due to the creation of the cavity inside the unform medium. The last term adds up for dispersion forces acting between solvent and solute.

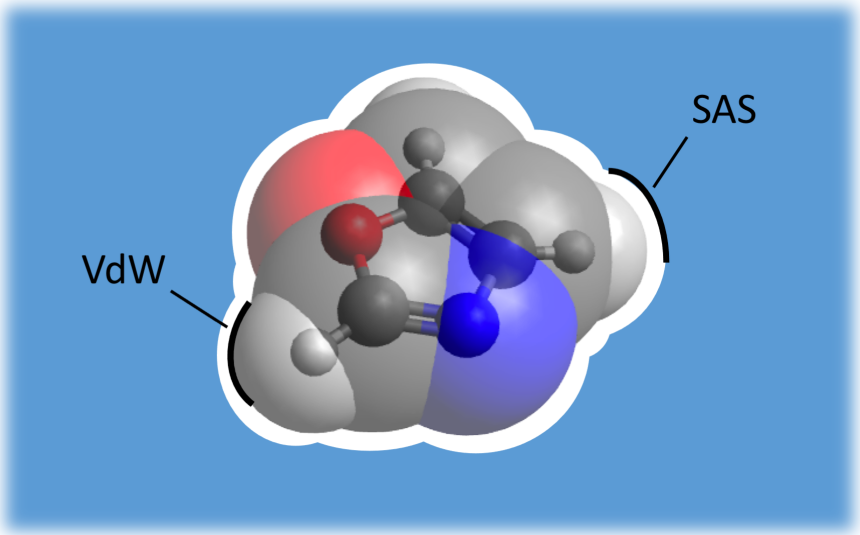

Figure 2.2: Implicit solvent model. The solute is placed inside a cavity in the continuum dielectric medium (blue), which is modeled on the Van der Waals surface of the solute atoms. The solvent accessible surface (SAS) delimits a volume where the dielectric continuum cannot penetrate.

The universal solvation model based on solute electron density (abbreviated as SMD) proposed by Cramer and Truhlar[222] uses the full quantum mechanical charge density of the solute without defining partial charges. In SMD the last two terms in eq. (2.21) are grouped into a cavity-dispersion term which is evaluated as:

$$\Delta G_{cds} = \sum_{i}^{N} \sigma_k A_k + \sigma^{[M]} \sum_{i}^{N} A_k \tag{2.22}$$

where σ_k and $\sigma^{[M]}$ are atomic and molecular surface tensions, and A_k is the solvent-accessible surface (SAS) area, which depend on the geometry, the atomic Van der Waals radii and a solvent radius. The definition of solvents in the SMD model requires a few parameters like the dielectric constant, the refractive index, the surface tension and acidity and basicity parameters.

2.1.9 Nudged elastic band

Multi-structure interpolation methods (often indicated as *chain-of-state* methods) make use of multiple geometry structures that connect reactants to products in a physico-chemical

process. The images connecting the two extremes are first generated as interpolations along a straight line, but then they are relaxed, according to several algorithms, in order to optimize the saddle point and/or to approximate the whole reaction path. *Nudged elastic band* (NEB) is a common technique for finding reaction paths and estimating the respective activation energy barrier. A target function (the *elastic band*) is defined as the sum of the energies of all the M images, plus a penalty quantity (the last term in eq. 2.23) that prevents the images from collapsing towards the energy minima, keeping them distributed along the path:

$$T_{NEB} = \sum_{i=1}^{M} E(x_i) + \sum_{i=1}^{M-1} \frac{1}{2} k (x_{i+1} - x_i)^2 \tag{2.23}$$

Given the functional shape of the penalty terms as harmonic potentials, the concept of "springs" connecting the images into a linear chain is often introduced, and an appropriate value for the spring constant k has a strong influence on the convergence of the NEB optimization. If it is too small, the springs are too "weak" and the images will tend to slide in the direction of the energy minima. If it is too large, the springs will be too rigid and the distribution of images will tend to cut corners along the path.

Chapter 3

Results and Discussion

This chapter presents all original research work conducted by the author of this thesis. The first section is dedicated to the mechanistic study of the disproportionation of superoxide and its connection to $^1O_2$ production. The competing metal-reduction route is introduced as well. In the second section, the oxidative route of Li_2O_2/LiO_2 discharge products assisted by halogen/halide redox mediators is duscussed.

3.1 Non-mediated Oxygen Reduction Reactions

3.1.1 Structures of reduced oxygen species

The basic chemistry of ORR is essentially that of reduced oxygen species in the aprotic electrolyte. The minimum energy geometries for alkali and alkline-earth metals superoxides and peroxides were optimized at different levels of theory: DFT with many different functionals, MP2 in the spin-component scaled variety (SCS-MP2) and CASSCF. The ma-def2-TZVP basis set was employed with any of these methods. The significant geometric parameters of gas-phase monomeric species are reported in table 3.1. These are relative to the MP2 minimum geometries (B2GP-PLYP double-hybrid DFT values in parenthesis for comparison), which have been chosen as representative because they are the closest to the geometries optimized for some selected compounds via numerical differentiation with the NEVPT2 method, which represent our standard of reference. CASSCF/NEVPT2 calculations make use of a 6-orbitals active space for these monomeric species, which includes the oxygen 2p molecular orbitals, hosting 7 or 8 electron.

Formula	r(O-O) [Å]	r(O-M) [Å]	A(O-O-M) [deg]
O_2	1.210 (1.208)	-	-
superoxide			
O_2^-	1.351 (1.346)	-	-
HO_2	1.317 (1.318)	0.976 (0.974)	104.83° (105.26°)
LiO_2	1.355 (1.347)	1.757 (1.744)	67.31° (67.28°)
NaO_2	1.358 (1.351)	2.135 (2.126)	71.45° (71.46°)
KO_2	1.352 (1.345)	2.460 (2.446)	74.04° (74.04°)
BeO_2^+	1.393 (1.383)	1.500 (1.492)	62.34° (62.38°)
MgO_2^+	1.382 (1.374)	1.890 (1.883)	68.55° (68.60°)
CaO_2^+	1.348 (1.338)	2.130 (2.116)	71.55° (71.58°)
peroxide			
HO_2^-	1.503 (1.504)	0.965 (0.960)	97.97° (98.78°)
LiO_2^-	1.582 (1.559)	1.691 (1.678)	62.11° (62.31°)
Li_2O_2	1.589 (1.567)	1.734 (1.721)	62.74° (62.90°)
NaO_2^-	1.587 (1.553)	2.057 (2.054)	67.31° (67.79°)
Na_2O_2	1.604 (1.583)	2.084 (2.076)	67.38° (67.93°)
KO_2^-	1.570 (1.550)	2.335 (2.319)	70.36° (70.48°)
K_2O_2	1.575 (1.554)	2.391 (2.369)	70.77° (70.85°)
BeO_2	1.689 (1.661)	1.434 (1.424)	53.92° (54.32°)
MgO_2	1.666 (1.643)	1.812 (1.804)	62.63° (62.91°)
CaO_2	1.551 (1.527)	2.001 (1.987)	67.19° (67.40°)

Table 3.1: Geometric parameters from MP2 (B2GP-PLYP in parenthesis) optimized energy minima for monomeric superoxide and peroxide structures (in vacuum).

Formula	r(O-O) [Å]		r(O-M) [Å]	
	b_1	b_2	r_1	r_2
HO_4^-	1.306	-	1.215	-
LiO_4^-	1.355	-	1.887	-
Li_2O_4	1.363	1.342	1.913	1.864
NaO_4^-	1.356	-	2.249	-
Na_2O_4	1.363	1.342	2.268	2.228
KO_4^-	1.352	-	2.618	-
K_2O_4	1.379	1.321	2.373	2.340
BeO_4	1.374	-	1.583	-
MgO_4	1.371	-	1.946	-
CaO_4	1.352	-	2.239	-

Table 3.2: Geometric parameters from MP2 optimized energy minima for dimeric superoxide structures in triplet spin multiplicity (in vacuum).

At a first glance, the main geometrical variation is represented by the elongation/shortening of the O-O bond distance, which falls into a characteristic range of lengths for each oxidation state: it is close to 1.2 Å for molecular O_2, between 1.3 and 1.4 Å for the superoxides and larger than 1.5 Å for peroxides. The metal cation is always symmetrical with respect to the two O atoms (see fig. 3.1, first and second row). Hydrogen compounds are an exception, since the optimal O-H distance is too short in order to have two equal bonds. As a consequence, the excess spin density in HO_2 is largely localized on the farthest O atom, which is roughly a localized radical, as opposed to metal superoxides where the extra electron is delocalized across the two O atoms. The O-M distance, on the other hand, is much more sensible to the size of the cation, as expected, even if a significant decrease can be seen when the oxidation number is lowered from superoxide to peroxide, as a result of the increased ionic attraction strength.

Superoxide dimers present structural parameters similar to those of the MO_2 monomers. As reported in table 3.2, both the O-O bonds fall into the same range of lengths, while the oxygen-cations distances result in average $\sim$ 0.1 Å longer, as a consequence of more

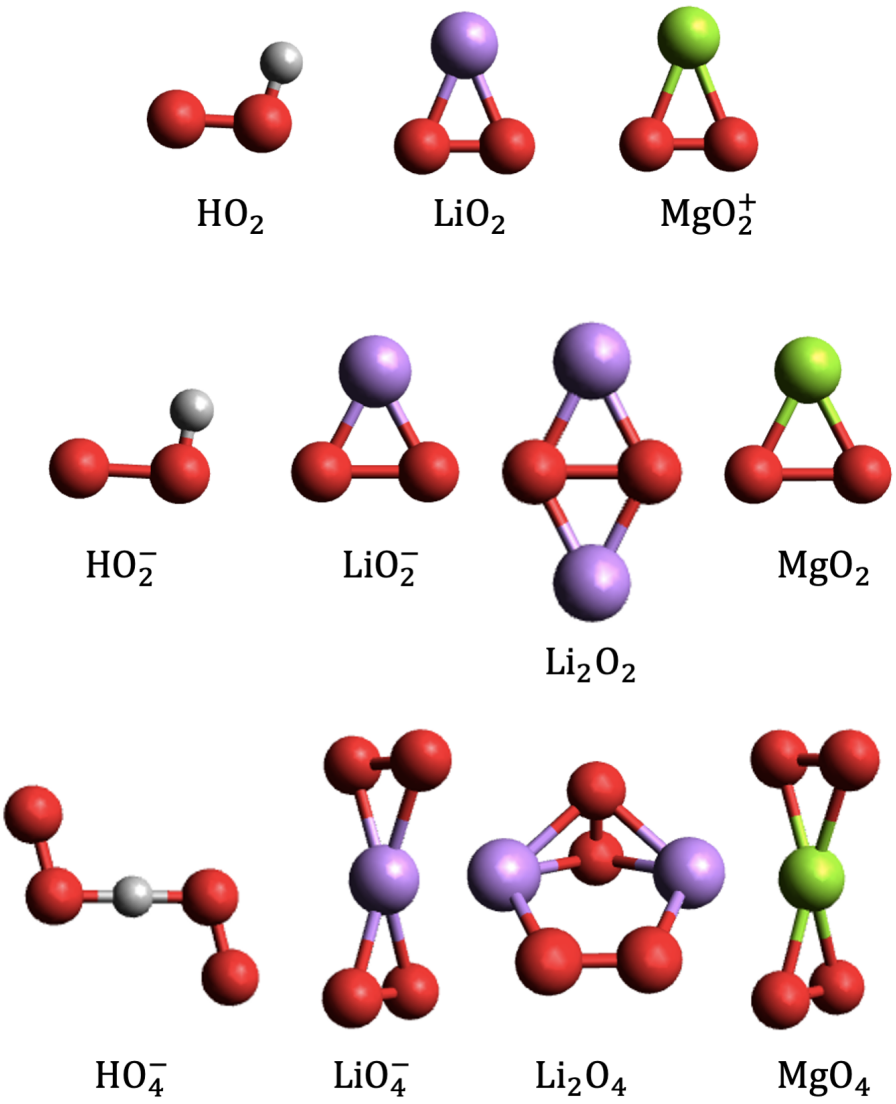

Figure 3.1: Optimized geometries of reduced oxygen species: superoxide monomers (first row), peroxide monomers (second row) and superoxide dimers (third row).

charge delocalization. Interestingly, MO_4-like stoichiometries, which are common to both alkali anionic $[MO_4]^-$ dimers and to alkaline-earth neutral MO_4 salts, present a symmetric minimum geometry in the D_{2h} point group (C_{2h} for HO_4^-), with the single cation at the center (fig. 3.1, lower row). Alkali neutral $[M_2O_4]$ dimers, on the other hand, share a C_{2v} point symmetry where the two O_2^- moieties are not equivalent, in agreement with previous computational studies[39,157,158], even if the the O-O bond lengths close to each other (for instance, 1.36 and 1.34 Å in Li_2O_4). Since the superoxide dimers are formed by coupling two spin doublet species, the resulting spin multiplicity can be either singlet or triplet. For each structure, the singlet and triplet complexes result to be almost equal in energy, as can be proved by CASSCF and NEVPT2 calculations which use a correct multireference wave function as required in general by open-shell singlet diradicals. However, this same result is also obtained with broken-symmetry MP2, which in this case can reproduce the correct degeneracy of the two spin states despite the multiconfigurational character of the singlet one.

3.1.2 Disproportionation route

The disproportionation reaction requires that the two superoxide anions are brought together overcoming their electrostatic repulsion (see section 1.1.4). Considering the reactive step of eq. (1.4) as an electron-transfer from one superoxide anion to the other, a dimeric complex is expected to form in order to achieve an effective overlap of donor and acceptor orbitals. A bridging cation hence mitigates the strong coulombic repulsion acting between the two anions. This model is clearly suited to represent the homogeneous/solution mechanism. Solid-phase and heterogeneous processes are beyond the purposes of this thesis. In solution, the two anions can react in presence of one or two cations, as for example in reactions (1.9) and (1.10); we will refer to the two cases as to ionic and neutral stoichiometry. Accordingly, in the case of first-group element (H and alkali metals), a dimerization step will take place that brings to a charged (eq. 3.2) or neutral (eq. 3.3) superoxide dimer structure:

$$M^+ + {O_2}^- \longrightarrow MO_2 \tag{3.1}$$

$$MO_2 + {O_2}^- \longrightarrow [MO_4]^- \tag{3.2}$$

$$MO_2 + MO_2 \longrightarrow [M_2O_4] \tag{3.3}$$

For alkaline-earth metals, on the other hand, the two monovalent superoxide anions are already brought together in the neutral formula of the superoxide salt:

$$M^{2+} + 2\,O_2{}^- \longrightarrow M(O_2)_2 \tag{3.4}$$

This latter process can be tentatively split into two consecutive ionic associations, for the sake of analogy with eqs. (3.1-3.3), but no mechanistic insights are known so far:

$$M^{2+} + O_2{}^- \longrightarrow MO_2{}^+ \tag{3.5}$$

$$MO_2{}^+ + O_2{}^- \longrightarrow M(O_2)_2 \tag{3.6}$$

All of these superoxide dimeric species represent a reactive complex for the subsequent transfer of electron. A typical minimum-energy conformer is found for each of the different stoichiometric complexes, which were exposed in the previous section.
Overall, the dimerization step is always predicted to be exoergonic, so that reactive complexes should always form unless transport limitations hinder the dimerization kinetics. The electronic energies calculated for this dimerization are reported in table (3.1.2). NEVPT2 single point calculations were performed on top of the ground-state MP2 geometries, and both the energies of the lowest triplet and singlet states are present.

As normally expected for gas-phase ionic reactions, the ΔE calculated in vacuum have all largely negative values, due to the electrostatic stabilization of the bare ions after they are brought together. Along a series of same-group metal cations, the lighter ones, Li^+ and Be^{2+}, with their high charge density, are the most unstable in vacuum and hence their reaction energies are lower then the those of the heavier cations. When involving alkali cations, the dimerization is 2.1 - 2.7 eV and 1.3 - 1.8 eV exoergonic, respectively, for the anionic and the neutral reactive complex. The formation of alkaline-earth metal $M(O_2)_2$ superoxide follows a different stoichiometry in table 3.4, and is thus difficult to compare. Anyway, gas-phase divalent cations undergo a huge stabilization when forming neutral $M(O_2)_2$, with energies relative to eq. (3.6) as low as -11 eV in the case of beryllium. Taking into account the solvation effects is therefore essential in order to have a more realistic estimate of the energy of formation of the $M_x(O_2)_2$ reactive complexes from isolated anions and cations. The implicit solvent model SMD was used with two different parametrized solvents, namely diethyl ether and acetonitrile. The former, despite not being used for the formulation of electrolytes in MOBs, was chosen for its chemical and polarity

M^+ cation	Solvation	MO_4^-	$MO_2^- \cdots O_2$	MO_2^- + O_2
H^+	gas	-1.33/-1.33	-0.63/+0.29	-0.58/+0.38
	Et_2O	-0.92/-0.93	-	-0.57/+0.39
	CH_3CN	-0.27/-0.28	-	-0.56/+0.40
Li^+	gas	-2.66/-2.66	+0.55/+1.51	+0.64/+1.60
	Et_2O	-1.65/-1.65	-	+0.71/+1.67
	CH_3CN	-1.28/-1.28	-	+0.67/+1.63
Na^+	gas	-2.48/-2.48	+1.61/+2.54	+1.34/+2.31
	Et_2O	-1.39/-1.39	-	+1.24/+2.20
	CH_3CN	-1.01/-1.01	-	+1.11/+2.07
K^+	gas	-2.11/-2.11	+1.61/+2.54	+1.72/+2.69
	Et_2O	-1.08/-1.08	-	+1.53/+2.49
	CH_3CN	-0.73/-0.73	-	+1.35/+2.31
M^+ cation	Solvation	M_2O_4	$M_2O_2 \cdots O_2$	M_2O_2 + O_2
Li^+	gas	-1.52/-1.51	-0.82/+0.14	-0.79/+0.17
	Et_2O	-0.91/-0.91	-	-0.30/+0.66
	CH_3CN	-0.71/-.070	-	+0.14/+0.82
Na^+	gas	-1.77/-1.77	-0.34/+0.61	-0.29/+0.67
	Et_2O	-1.07/-1.07	-	+0.24/+1.20
	CH_3CN	-0.82/-0.82	-	+0.40/+1.36
K^+	gas	-1.31/-1.31	+0.08/+1.04	+0.09/+1.05
	Et_2O	-1.18/-1.18	-	+0.62/+1.58
	CH_3CN	-0.94/-0.94	-	+0.79/+1.75

Table 3.3: Energy of reaction calculated with the NEVPT2 method (units are eV) for the different steps of the superoxide disproportionation of first-group cations. Both triplet/singlet energies are given, in this order.

affinity with the well-established glyme solvents (like TEGDME), for which ready-made parameters were lacking. When the implicit solvent is introduced, the stabilization effect is more pronounced on the isolated charged ions than on the reactive complexes, where the charge is much more diffused. The energies of eqs. (3.2),(3.3) and (3.6) are then greatly reduced, and this is more pronounced when passing to a solvent with a higher dielectric constant (ϵ_{Et_2O} = 4.2 and ϵ_{CH_3CN} = 35.7). As a result, the exoergicity of the reaction is significantly reduced in all of the cases. It is relevant to notice a difference between the lighter Li^+ and Na^+ cations and the heavier K^+. In the less polar medium (diethyl ether), reac. (3.2) is energetically favored over reac. (3.3) by 0.74 eV for Li+ and 0.32 eV for Na^+. These values in a higher polarity solvent (acetonitrile) are lowered to 0.57 eV and 0.19 eV respectively, because the isolated anion in the left-hand side of reac. (3.2) results to be increasingly stabilized, but still the anionic stoichiometry is clearly the one associated with a lower energy. Potassium, on the other hand, forms more stable neutral complexes $[K_2O_4]$ in both of the continuum environments (-0.1 eV and -0.21 eV , respectively in diethyl ether and in acetonitrile, referred to $[KO_4]^-$). Interestingly, potassium differs from lithium and sodium in that the reactive complex that is thermodinamically favored is also the one which requires more mass transport, namely two K^+ cations instead of one. When it comes to protons, only the anionic $[HO_4]^-$ was considered, because the presence of water as trace impurities makes unlikely the encounter of two protonated HO_2 in solution. Moreover, as discussed in sec. 1.1.4, one HO_2 reacts faster with an O_2^- anion, as in eq. (1.9), hence it will hardly be long-lived enough to form the $(HO_2)_2$ dimer. The $[HO_4]^-$ has a less negative energy than the 1st-group metals, going from -1.33 eV in vacuum to -0.92 eV and -0.27 eV in diethyl ether and acetonitrile, respectively.

For akaline-earth metals the formation of $M(O_2)_2$ superoxides displays a very strong exoergicity. Following eq. (3.6), the relative energies range from -5.75 eV of Be^2+ to -3.47 eV for Ca^2+ when in diethyl ether, and these become -3.89 eV and -2.06 eV in acetonitrile. During this reactive step, the energy results to be substantially independent of the total spin multiplicity. For any of the reactive-complexes, the coupling of the two unpaired spins residing on the O_2^- moieties results in a triplet or a singlet with almost identical energies (differences are in the order of 0.01 eV at most). This is correctly assessed only with the multireference NEVPT2/CASSCF method, since the wave function of the open-shell singlet made up of two unpaired electron spins is of intrinsic multiconfigurational character.
After the formation of the superoxide dimer complex, the disproportionation takes place through an electron-transfer reactive step, where an electron is transferred from one super-

M^{2+} cation	Solvation	MO_4	$MO_2 \cdots O_2$	MO_2 + O_2
Be^{2+}	gas	-11.51/-11.52	-9.01/-7.98	-8.60/-7.64
	Et_2O	-5.75/-5.76	-	-3.82/-2.85
	CH_3CN	-3.89/-3.90	-	-2.47/-1.50
Mg^{2+}	gas	-9.80/-9.81	-6.31/-5.36	-6.28/-5.32
	Et_2O	-3.76/-3.76	-	-1.85/-0.89
	CH_3CN	-1.99/-1.99	-	-0.63/+0.33
Ca^{2+}	gas	-8.17/-8.17	-5.50/-4.55	-5.45/-4.49
	Et_2O	-3.47/-3.47	-	-1.57/-0.63
	CH_3CN	-2.06/-2.06	-	-0.53/+0.43

Table 3.4: Energy of reaction calculated with the NEVPT2 method (units are eV) for the different steps of the superoxide disproportionation of second-group cations. Both triplet/singlet energies are given, in this order.

oxide unit to the other. The outcome of this process is a neutral/anion peroxide plus an O_2 molecule:

$$[MO_4]^- \longrightarrow MO_2{}^- + O_2 \tag{3.7}$$

$$[M_2O_4] \longrightarrow M_2O_2 + O_2 \tag{3.8}$$

The thermodynamics of such a process was already investigated in some theoretical works[157,158], where the energy of ground-state structures and intermediates poses no specific problem to the use of correlated single-reference computational methods. However, this does not also apply, in the general case, to the transition-state of an electron-transfer process; hence, the activation barriers and the kinetics of the reaction are tricky to estimate from this approach. Owing to the possibility of monitoring several excited states and their relative orbital occupations, we employed multiconfigurational ab-initio methods for exploring the evolution of the potential energy surfaces of reactants and products along the reaction coordinate. In order to obtain a reasonable reaction coordinate, the nudged elastic band (NEB) method was used. This essentially requires a minimum structure for the reactant species and another one for the products. The first is represented by the reactive $[M_xO_4]$ complex. For the products, a peroxide-O_2 complex with a very small potential-well can be optimized, where the two product molecules are already formed but still weakly bound at a relatively short distance (second column from right in tables 3.1.2 and 3.4). Between these two structures, a possible geometric evolution of the system was represented interpolating

12 intermediate "images", which are optimized under the NEB constraints to give the best approximation to the minimum energy path. This procedure was applied to the $[MO_4]^-$ (1st-group elements) and $M(O_2)_2$ (2nd-group elements) complexes. A typical NEB reaction path is exemplified in fig. 3.2 (right panel). As the cation is removed from its central

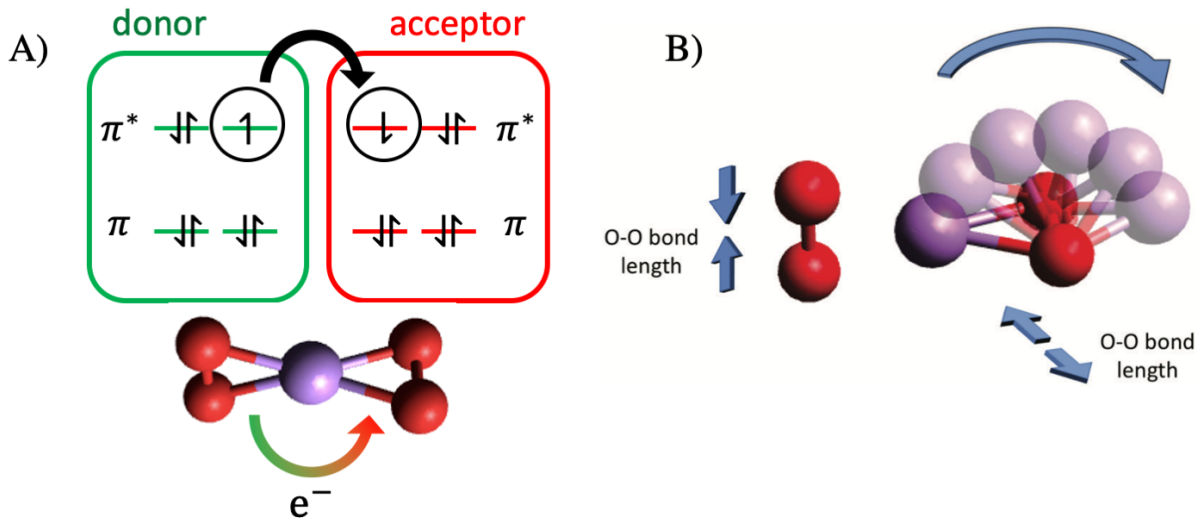

Figure 3.2: Scheme of the electron-transfer process. A) The jump of an electron between the two superoxides generates O_2 (the donor) and O_2^{2-} (the acceptor). B) Representation of the minimum energy reaction coordinate optimized by NEB. The O-O distance of the donor superoxide is shortened, while that of the acceptor superoxide is stretched.

symmetry, the O-O bond on the donor superoxide is shortened, approaching the final value of 1.2 Å as in the isolated O_2 molecule, while the bond distance of the acceptor superoxide is increased up to 1.5 - 1.6 Å, depending on the equilibrium geometry of the corresponding peroxide. The reaction path and its two extremes were optimized with MP2, in the ground-state spin multiplicity of triplet. Along this reaction coordinate, the NEVPT2 method was employed in order to calculate single-point energies in vacuum, at each of the intermediate images, for the first 5 triplet and 5 singlet SA-CASSCF roots while using a [18,12] active-space. Among all of the computed CASSCF roots, typically there is only a couple of them which is of interest: the ones representing the lowest "reactants" state and the lowest "products" state. In terms of active orbital occupation numbers, the two states are identified looking at those corresponding to the π^* anti-bonding orbitals on each of the O-O units (see fig. 3.2, left panel). The state of the reactants must present a $\boxed{2}\boxed{1}$ occupation scheme on both of the O-O moieties, which are then identifiable as two O_2^- superoxides. In the state of the products, instead, an O_2^{2-} peroxide corresponds to a $\boxed{2}\boxed{2}$ occupation in

the same orbitals, while the molecular oxygen corresponds to a $\boxed{1}\boxed{1}$ configuraation when in the triplet ground-state, and to two high-weight $\boxed{2}\boxed{0}$ and $\boxed{0}\boxed{2}$ configurations when in the lowest singlet, which is the $^1\Delta_g$ state. Because of the geometric conformation, the O_2 molecule is strongly perturbed with respect to its $D_{\infty v}$ symmetry group when isolated, so that the two closed-shell electronic configurations are no more energetically degenerate and their relative weights differ considerably, even if the smaller one is still clearly larger than any other minor configuration. Taking into account all the orbitals inside the active space, many permutations are possible that still produce O_2^- and O_2^{2-} charge density distributions, but represent excited states of these species. Such states may be energetically low-lying, or simply be wrongly ordered in energy at the CASSCF level. Hence, it is usually necessary to state-average over more than two roots in order to include both of the lowest reactants and products states, which are the ones we are interested in inside a two-state picture of the electron-transfer process. The number of five averaged roots, for each spin multiplicity, has shown to suffice for the purpose, so it was held constant in all of the scans for the sake of consistency. The potential energy curves are presented in fig. 3.3, showing only the two relevant states in both triplet (black line) and singlet (red line) multiplicity. The trend in the curve is general to all of the cases. Beginning from the left, the energy of the triplet and singlet superoxide states is equally lifted, showing a substantial degeneracy across all of the geometry change. The peroxide states grow approximately in parallel in energy in the opposite direction, having their minimum on the right of the reaction coordinate, and present a neat separation between the triplet and singlet curves, this latter being always higher in energy by 0.6 - 0.9 eV, which is all or part of the $^3\Sigma \rightarrow {}^1\Delta$ vertical excitation energy. At some point the curve intersect, making it possible for the system to transit from the potential well of the reactants to that of the products. The crossing point of curves with the same multiplicity can therefore be taken as an approximation to the energetic barrier required for the electron-transfer to proceed. With all of the metals this barrier is very high, going approximately from 2.6 eV to 4.0 eV, and it is close to the final energy of the product complex. The minimum in the lowest product curve is always in very good agreement with single-root calculations, which assesses the quality of the state-average results. Two relevant observation can be derived from the graphs of fig. 3.3. First, because of the product states raising in energy very slowly from right to left, the curve crossings always occur at very close energy with respect to the product minimum. This means that kinetic barriers due to the conformational changes along the reaction coordinate play an irrelevant role in the course of the reaction, if compared to the entity of the thermodynamic ΔE. Secondly, since the above consideration holds regardless of the spin multiplicity, the energy gap between the two triplet and singlet crossing points never differs very much from the

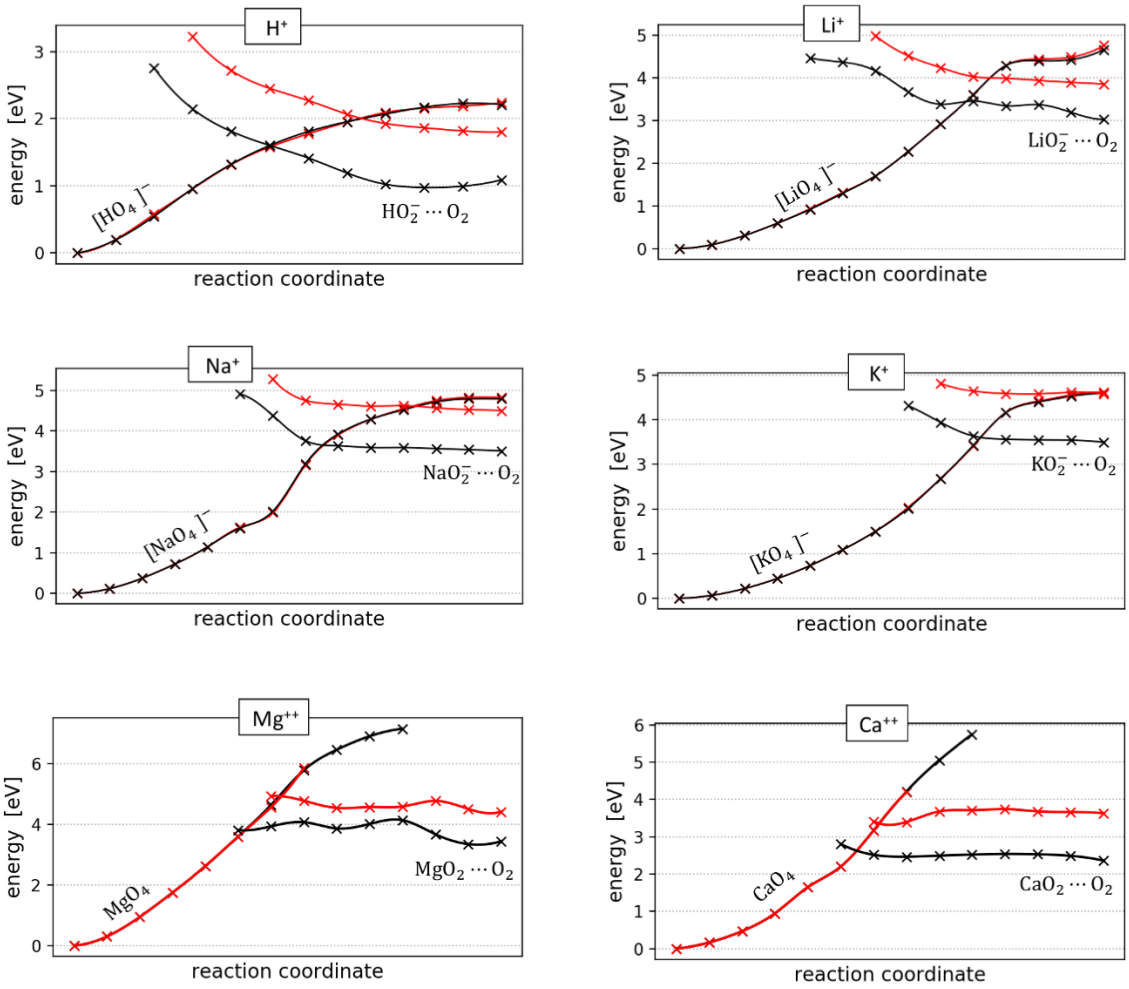

Figure 3.3: Potential energy curves of the electron-transfer step in proton, alkali and alkaline-earths superoxide disproportionation. Black curves are triplet states, while red curves are singlet ones.

gap at the equilibrium geometry. Therefore, from this electron-transfer route, no effects of the cation apparently emerge which could explain a trend in singlet oxygen production different from the overall trend in the disproportionation rate. The case of hydrogen is rather different from the others, for it displays a clear hill-shaped barrier at the point of crossing. A different geometry (see section 3.1.1), and hence a different NEB path, is also involved. The energy after the transfer of the electron is only 1 eV higher than in the reactant, and $^1O_2$ is formed just by reaching the top of the red barrier at 2 eV, which is much lower than with any of the alkali or alkaline-earth metals. This is consistent with experiments reporting protic contaminants as strong booster for both disproportionation and singlet oxygen release. In the framework of electron-transfer theories, a crossing of the curves like those in fig. 3.3 depicts a diabatic-like regime of reactive transition from the reactants to the products. The lack of interaction between pairs of same-multiplicity states is actually a spurious effect due to on-top perturbative corrections which are computed at the NEVPT2 level over the CASSCF solutions. In fact, when dealing with the present systems, CASSCF systematically fails to correctly estimate the state-averaged energies, and even the qualitative ordering of the roots. This leads to a lack of state-interaction, at the CASSCF level, in what should have been the actual region of avoided crossing. This interaction cannot be recovered by the original formulation of the NEVPT2 theory, which therefore yields diabatic-like energy curves which incorrectly intersect, ignoring the repulsion between the two levels. To restore the correct behaviour, quasi-degenerate pertubation theory can be adopted. Applying the QD-NEVPT2 formalism to restricted regions in the proximity of the curve crossing, we obtained a strong avoiding which makes the global minimum energy path entirely uphill from the beginning to the end. Quantitatively, however, the change is not important since, as mentioned before, the kinetic barrier already was almost coincident with the neat endoergicity of the reaction.

As pointed above, when the energy of the reactive complex matches that of the product, the system is ready to undergo disproportionation. We conclude that the reaction is dominated by its thermodynamics, and that, at this stage, the energy of the singlet state can be taken into account in a first approximation by shifting the ground-state triplet energy by ca. 0.9 eV upwards. Under this assumptions, we went forward analyzing the profile of the Gibbs free energy at each reaction step. Free energies at are evaluated at 298 K under the approximation of harmonic vibrations and assuming a perfect-gas molecular partition function. Since from a thermodynamic point of view we are interested in the ground-state alone, these free energies were calculated only for the triplet at the SCS-MP2 and DFT level, the latter employing the double-hybrid B2GP-PLYP functional with D3 dispersion corrections. The solvent is introduced, as before, through the SMD continuum model.

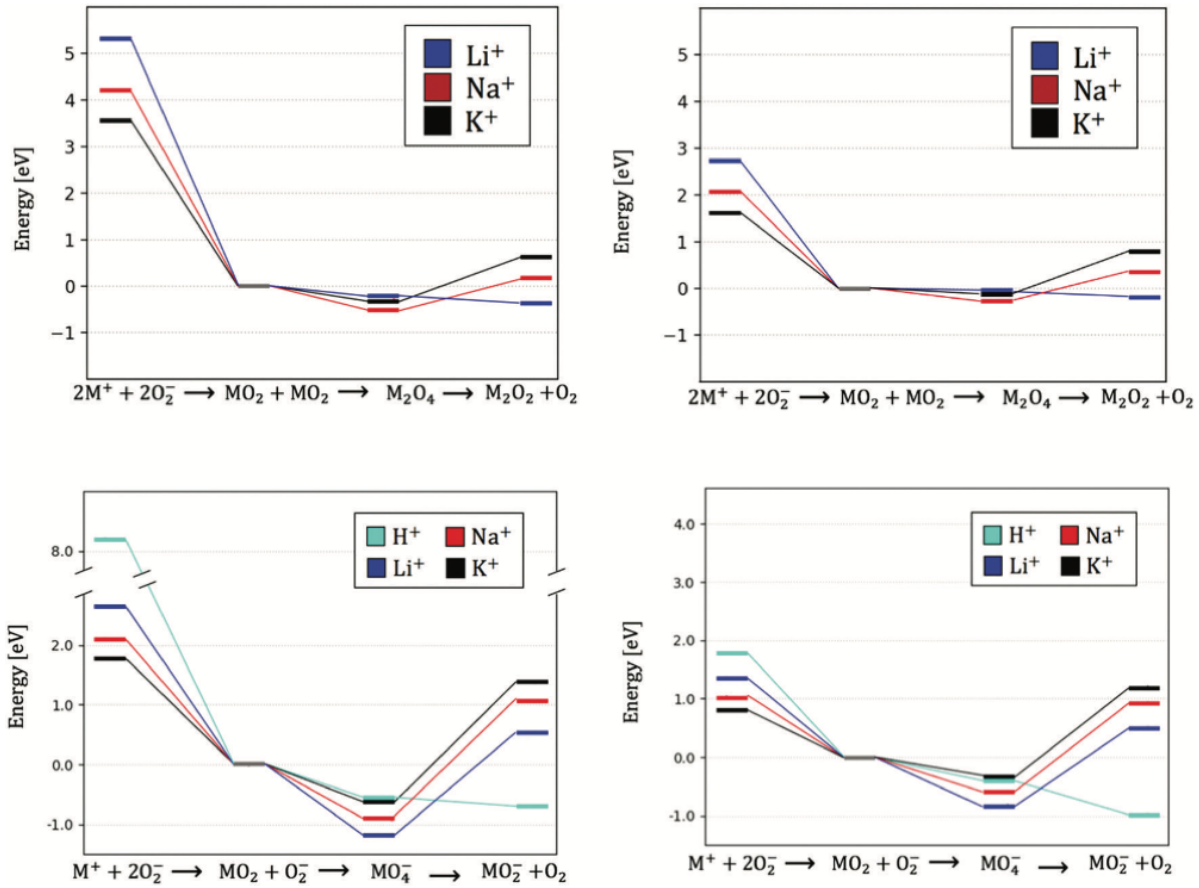

Figure 3.4: Free energy landscapes for the disproportionation of alkali metals in the neutral (upper panels) and anionic (lower panels) stoichiometries. Free energies are calculated in implicit solvent, namely diethyl ether (ϵ = 4.2) on the left and acetonitrile (ϵ = 35.7) on the right

The results are summarised in figs. 3.4-3.5, divided according to the different reaction stoichiometries. The global reaction is divided into three steps: 1) association of one or two superoxides with the M^{n+} cations, starting from the isolated ions; 2) combination of two superoxides to form a reactive dimer complex, $[M_nO_4]$; 3) disproportionation of the superoxide dimer to release peroxide (neutral or anion) and free O_2. In this last step, the product was considered as isolated molecules/ions. In fact, the weakly bound peroxide-O_2 complex is found to dissociate with negligible energy changes, so the presence of such an intermediate is not relevant for a discussion on the reaction thermodynamics, although the existence of such a relative minimum was useful for optimizing the NEB coordinates discussed above. The initial, fully dissociated ionic state is very high in energy, because of the Coulomb interactions. For the alkali metals, the first step is the ionic association of

reac. (3.1), repeated one or two times. In the neutral stoichiometry, two MO_2 superoxides are formed, which makes the first step exoergic by 3.5 - 5.3 eV in diethyl ether and 1.6 - 3.8 eV in acetonitrile, which is enough to yield a total negative ΔG for any of the metals. In the following step, the dimerization of reac. (3.3) takes place as already discussed before. However, the inclusion of entropic contributions now significantly changes the scenario given by the sole potential energy: as a result, the dimerization energy is strongly reduced, and the Li_2O_4 and K_2O_4 complexes are almost isoergic with the separated superoxides, while Na_2O_4 is slightly more exoergic. The third step, where the actual electron-transfer occur, presents a striking difference between lithium and the others: in fact, while Na_2O_2 and K_2O_2 require about 1 eV to form, Li_2O_2 is produced with a slightly negative ΔG. This difference is particularly relevant for it makes the energy profile of the whole $2Li^+ + 2O_2^-$ reaction entirely downhill in all of its steps. On the other hand, the anionic mechanism is not critically affected by the introduction of entropic contributions, with respect to the electronic potential energies analyzed before. In particular, the $[MO_4]^-$ dimers do all disproportionate with a large positive ΔG of $\sim$ 2.0 eV in diethyl ether and $\sim$ 1.5 eV in acetonitrile. The H^+ cation is the only one to behave in a different way, compared to Li^+, Na^+ and K^+, for its electron-transfer step is exoergic (-0.7 eV in acetonitrile) and the reaction is completely spontaneous.

Comparatively, the neutral stoichiometry is more exoergic, and has a less positive ΔG in electron-transfer step, which is even negative in the case of lithium. In the anionic case, the total exoergicity is much less pronounced, and the electron-transfer step presents a much higher positive barrier, except for the proton which is extremely effective in promoting the disproportionation even in absence of other cations.

Alkaline-earth metals display a different energy landscape (fig. 3.5), which is only marginally affected by the entropic contributions if compared to the data on electronic energy. The exoergicity of the MO_4 superoxide, with respect to $MO_2^+ + O_2^-$, is maintained for the reactions of both Mg^{2+} and Ca^{2+}, and the subsequent step which converts the MO_4 complex into the disproportionation products is endoergic by about 1 eV in Et_2O and slightly less in CH_3CN. As with alkali metals in the neutral reaction, the medium polarity has a stronger impact on the isolated neutral products, reducing the overall process exoergicity for larger dielectric constants.

Last, it should be noted that reversibility from peroxide to superoxide will be heavily influenced by the solubility of the neutral products. The precipitation of insoluble species can represent a strong, additional thermodynamic driving force. While peroxides are generally insoluble in all of the aprotic solvents employed in MOBs, the solubility of superoxide is more variable, so that at the end the equilibrium of the real process will be shifted towards

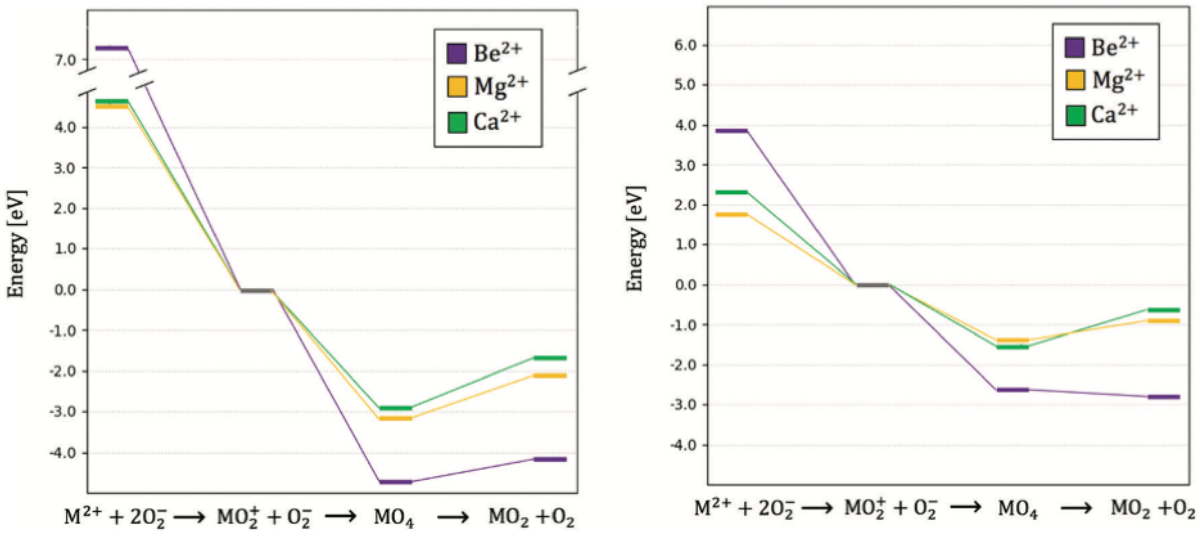

Figure 3.5: Free energy landscapes for the disproportionation of alkaline-earth metals. Free energies are calculated in implicit solvent, namely diethyl ether (ϵ = 4.2) on the left and acetonitrile (ϵ = 35.7) on the right

the formation of products, thus reducing the overall reversibility of the process.

3.1.3 Metal reduction route

During the study of the disproportionation route, an assumption is made that the MO_2^- product is a peroxide anion. Despite the intuitive closed-shell electronic configuration, with doubly occupied molecular orbitals on O_2^{2-} and a +1 charge on the metal cation, many problems were encountered when converging DFT optimizations, with many different funcitonals, of the peroxide anion MO_2^-, and this happened particularly in the case of sodium and potassium. These problematic optimizations ended in final structures which are hardly interpretable, with a strong asymmetry of the metal with respect to the O atoms, an exceedingly shortened O-O bond (around 1.3 Å instead of 1.5 - 1.6 Å) and partial charges far from reflecting the expected chemical identity of the species. SCF stability analysis was employed to verify if the closed-shell solution represents the actual minimum in the space of MO coefficients. SCF instabilities of the exeternal RHF/UHF kind were detected instead, something that implies the existence of lower energy solutions where the restrictions on the spatial part of the spin-orbitals are removed. Diradicals are typical systems where the singlet multiplicity cannot be enforced in a RHF formalism. In the context of single-reference SCF methods, this can be achieved instead by converging the

wave function to a broken-symmetry UHF solution. At the same time, the presence of such instabilities are also often interpreted as the sign of an underlying multiconfigurational character of the minimum-energy wave function[223]. We therefore treated the triatomic MO_2^- anion (for M = Li, Na, K) at the CASSCF level plus NEVPT2 or multireference SDCI correlation. Alongside with the six oxygen-p orbitals, the 2s, 3s or 4s orbital of Li, Na and K, respectively, was included in the active space, which then counts 10 electrons in 7 orbitals, that is [10,7]. As an unexpected result, we found that, depending on the geometry of the system and on the metal, the peroxide-like state, where all 10 electrons reside on oxygen orbitals leaving a +1 charge on the metal, is now flanked by a superoxide-like state, where 1 electron is promoted to the *n*s metal orbital, which becomes formally neutral. If we limit ourselves to the occupation numbers in the space of the two oxygen π^* and the metal *n*s orbitals, given in this order, the above states corresponds to $\boxed{2}\boxed{2}\boxed{0}$ and $\boxed{2}\boxed{1}\boxed{1}$ electronic configurations, respectively. To make it more explicit, a different product outcome is now

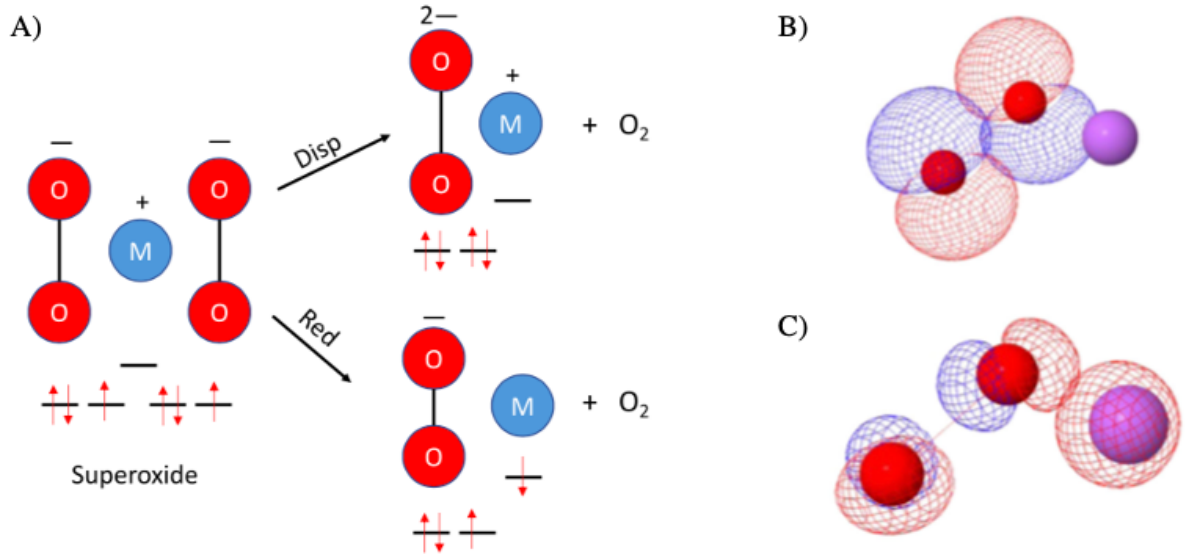

Figure 3.6: The competing forms of the MO_2^- product. A) Scheme of the different orbital occupation in the peroxide (upper arrow) and superoxide (lower arrow) states. B) Plot of the highest occupied molecular orbitals in the two cases: a doubly occupied oxygen π^* orbital for the peroxide state, C) a singly occupied s metal orbital for the superoxide state.

taken into account for the disproportionation (see also the scheme of fig. 3.6):

$$MO_2 + {O_2}^- \longrightarrow M^{(+1)}{O_2}^{(-2)} + O_2 \tag{3.9}$$

$$MO_2 + {O_2}^- \longrightarrow M^{(0)}{O_2}^{(-1)} + O_2 \tag{3.10}$$

Peroxide state	vacuum	diethyl ether	acetonitrile
$Li^{(+)}O_2^{(2-)}$	3.28 / 4.25	2.33 / 3.29	1.92 / 2.88
$Na^{(+)}O_2^{(2-)}$	3.85 / 4.80	2.67 / 3.63	2.15 / 3.11
$K^{(+)}O_2^{(2-)}$	3.82 / 4.78	2.61 / 3.57	2.10 / 3.06
Sueroxide state	vacuum	diethyl ether	acetonitrile
$Li^{(0)}O_2^{(-)}$	2.61 / 3.57	2.97 / 3.93	3.06 / 4.02
$Na^{(0)}O_2^{(-)}$	2.11 / 3.07	2.42 / 3.38	2.52 / 3.48
$K^{(0)}O_2^{(-)}$	1.81 / 2.77	2.25 / 3.21	2.38 / 3.34

Table 3.5: NEVPT2 energies (in eV) of the reaction from the anionic MO_4^- reactive dimer to either of the MO_2^- + O_2 product forms. Triplet/singlet energies are given, in this order.

In the first place, we turned back to the study of reac. (3.7) assuming the extended active space with the additional metal orbital, so that the energy of the superoxide-M^0 state is now available as well. Consistently wit the previous approach, we used SCS-MP2 for the geometric optimization of the MO_2^- fragment. In order to converge the SCF part of the calculation on the superoxide state, a broken-symmetry singlet wave function is necessary, where the unpaired alpha electron on O-O and the unpaired beta electron on the metal produce a spin contamination of approximately 2.0 in S^2 atomic units. While this may appear to be in conflict with an approach based on multiconfigurational methods, we actually verified that the broken-symmetry MP2 geometries are in very good agreement (see data) with those optimized using NEVPT2 numerical gradients. So we continued to use single-reference MP2 only for the purpose of obtaining minimum structures, to be used for on-top multireference calculations. The basis set is ma-def2-TZVP, as before, but the quality of the results was also positively checked against the larger ma-def2-QZVPP basis. Relaxed to its minimum energy structure, this superoxide state presents a short O-O bond length of about 1.35 Å, while the O-M distance is sensibly enlarged: it is increased to 1.84, 2.23 and 2.55 Å for Li, Na and K, respectively, while they where only 1.69, 2.05 and 2.33 Å in the peroxide state. The two reaction channels, which we denote as the proper "disproportionation" (eq. 3.9) and the "metal reduction" (eq. 3.10) routes, were studied with the [18,13] active space in vacuum and in implicit solvent, again diethyl ether and acetonitrile.

Tab. 3.5 summarizes the ΔE of reaction leading from the $[MO_4]^-$ pre-reaction complex to

the two different product states. We just limited our analysis to the electronic potential energy, since we are just interested in the energy difference between the two states of MO2-, where the corrections due to vibrational modes and molecular entropy should differ for a negligible amount. In the gas phase, the reaction energy to $M^{(0)}O_2^{(-1)}$ ranges from 2.6 to 1.8 eV moving from Li to K, i.e. it follows a trend Li > Na > K that is the opposite of the one observed in the disproportionation route. In comparison, the superoxide state is in fact surprisingly lower in energy for any of the three metals: the ΔE between the two product states amounts to -0.67 eV in LiO_2^-, -1.74 eV in NaO_2^- and -2.01 eV in KO_2^-, as depicted in fig. 3.7. This way, the energy gain when reducing the heavier metals (Na and K) largely overcomes the triplet-singlet splitting, opening for an easier way for the release of $^1O_2$. It must be stressed that the disproportionation channel shows no significant changes in energy when the active space is increased from [18,12], as in the previous data, to [18,13]. This confirms that, as the metal orbital remains unoccupied all through the whole process, it doesn't contribute in a relevant way to the wave function, so the [18,12]-CAS is already suitable for assessing the disproportionation energetics. Clearly, the difference in charge separation between the peroxide and the superoxide states involve different behaviours in response to the introduction of a solvent. The higher the polarity of the medium, the more stabilized will be the peroxide state, where the charge separation is higher; compared to the situation in vacuum, the superoxide state will not experience a comparable stabilization, so that in the end the two states will be brought closer in energy. In diethyl ether (SMD implicit model) the energies of the reduction channel are all raised, and the situation undergoes a qualitative change. With a dielectric constant of 4.2, the metal reduction already becomes unfavorable (by 0.64 eV) for lithium, which is the less prone between the alkali to stabilize the $M^{(0)}O_2^{(-1)}$ state. On the other hand, the two reactive channels for sodium and potassium are close in energy, with the superoxide state still lower in energy by 0.2 - 0.4 eV. The same trend is repeated when switching to acetonitrile. In this case, all three the metals show a lower energy in the peroxide $M^{(+1)}O_2{}^{(-2)}$ state. But while the difference in lithium is striking (1.08 eV), for sodium and potassium, again, the distance between the two states remains within 0.3 - 0.4 eV. In order to check qualitative result given by the implicit solvent model, additional calculations were performed including a minimal shell of explicit solvent (fig. 3.8). This was performed only for the sodium NaO_2^- systems, in the two electronic states and with three different solvents (dimethoxyethane, acenotrile and dimethylsulfoxide), adding only the number of solvent molecules required to raise the coordination number of Na to n = 6. The total of six systems were, again, relaxed through geometrical optimization at the MP2 level, while the energies were subsequently evaluated in a multiscale ONIOM approach, treating the NaO_2^- portion at the usual NEVPT2 level

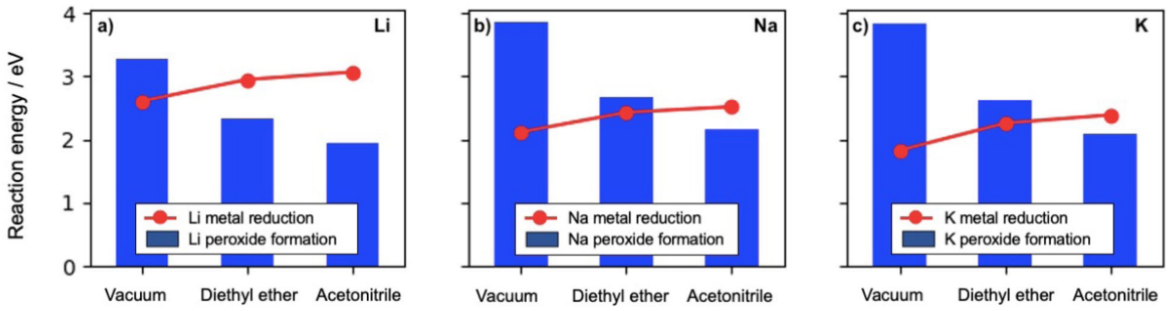

Figure 3.7: Superoxide-reduction vs metal-reduction in SMD implicit solvent. The energies of the peroxide channel are the blue bars, the energies of the metal-reduction channel are the red circles.

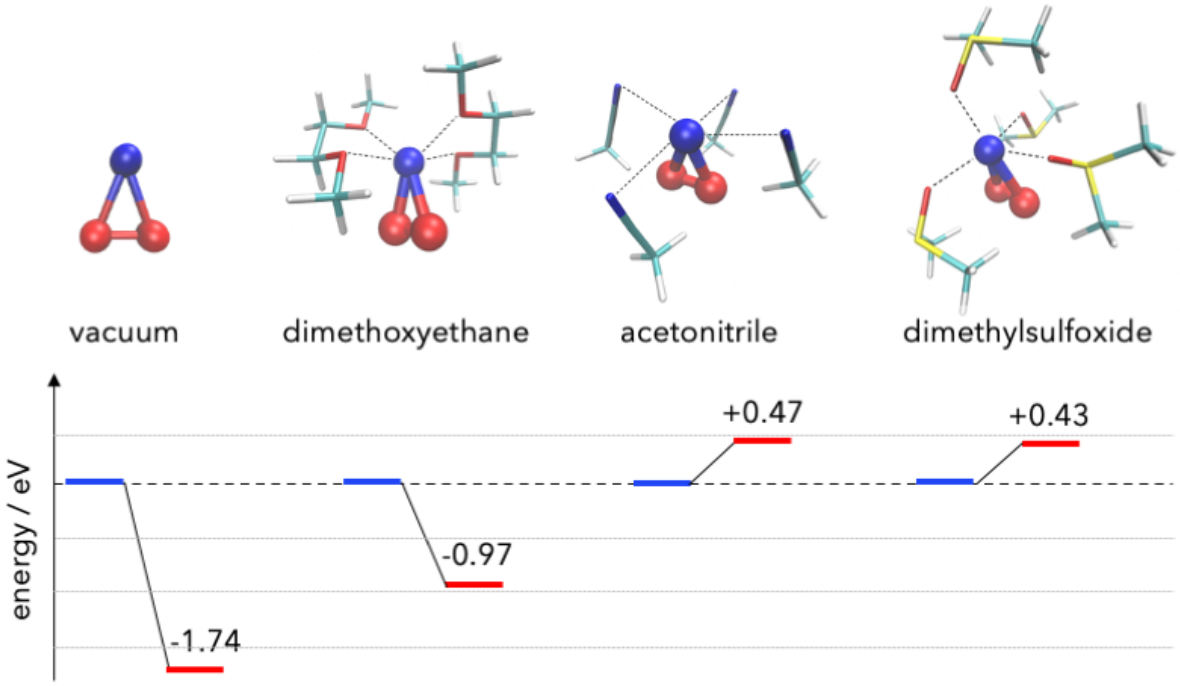

Figure 3.8: Superoxide-reduction vs metal-reduction for Na^+ inside an explicit solvent shell. A minimum number of solvent molecule is introduced, sufficient to raise to n=6 the coordination around the Na center. The energies of the peroxide and metal-reduction channels are the blue and red lines, respectively.

Peroxide states	vacuum	diethyl ether	acetonitrile
Li_2O_2	+0.73	+0.61	+0.57
Na_2O_2	+1.48	+1.31	+1.22
K_2O_2	+1.40	+1.80	+1.73
Superoxide states	vacuum	diethyl ether	acetonitrile
$Li^{(+)}Li^{(0)}O_2^{(-)}$	+3.17	+3.02	+3.00
$Na^{(+)}Na^{(0)}O_2^{(-)}$	+2.53	+2.50	+2.71
$K^{(+)}K^{(0)}O_2^{(-)}$	+2.07	+3.22	+3.21

Table 3.6: NEVPT2 energies (in eV) of the reaction from the neutral M_2O_4 reactive dimer to either of the M_2O_2 + O_2 product forms. Only triplet energies are reported.

while enforcing the MP2 for the coordinated molecules. Despite the considerable deviation in the energy values, a qualitative agreement is found between the two approaches, showing both: i) a neat stabilization of the peroxide state (in blue) over the superoxide (in red) for increased polarity of the solvent, regardless of other chemical properties like the donicity of the solvent; ii) an inversion of the relative position of the two states, occurring somewhere in between acetonitrile and low-polarity ethers along the scale of ϵ.
Overall, the reduction of Li^+ ion in the peroxide is unlikely in solution, whereas it remains a competitive route in the case of Na^+ and K^+. This opens up for a possible explaination for the $^1O_2$ release trend reported in ref.[39], as will be deepened in the next Discussion section.

This unforeseen metal reduction channel is only characteristic of the anionic reaction given by of eq. (3.7). When a second cation is involved (eq. 3.8), the presence of two positive charges is such to force the maximum charge separation, stabilizing the O_2^{2-} peroxide over the superoxide. These latter were optimized with the same broken-symmetry formalism as explained before, yielding an asymmetric structure where, of the two M centers, one has the orbitals population and charge density of an M^+ cation and the other that of a reduced M^0 neutral metal atom, placed at significantly larger distance from the O-O moiety. As the global charge is neutralized, it can be seen from table 3.1.3 that the peroxide state is much lower in energy already in vacuum, being around -1.0 eV for Na and K and more than -2.5 eV for Li. For this reason, this metal reduction may be regarded as limited to

solution mechanisms, where limitations in ion transport can favor the formation of relatively long-lasting anionic MO_2^- structures.

3.1.4 Electronic structure of the MO_2^- peroxide anion

Given the sharp difference in the geometry of the two energy minima, it is clear that the nature of the electronic state is fundamentally impacted by structural changes. In particular, the O-O bond distance seems to be critical for it determines the similarity with isolated superoxide ($\sim$ 1.3 Å) and peroxide ($\sim$ 1.5 Å) anions. This is altered for instance by vibrational motion, so a deeper analysis was required in order to clarify the mechanism of an eventual transition of the system from one state to the other. For example, the O-O stretching corresponds to a vibrational Raman peak at 810 cm^{-1} in Li_2O_2 and 1090 cm^{-1} in LiO_2[224], which means a significant population of the excited vibrational states at room temperature. In order to study the transient nature of the $M^{(0)}O_2^{(-)}$ specie, we scanned the potential energy surface of different electronic states in the triatomic system. This calculations were performed with the OpenMolcas code, using CASPT2 energies in the [10,7] complete active space with the cc-pVQZ basis set. Only the LiO_2^- and NaO_2^- triatomics were examined. In first place, the C_{2v} symmetry was enforced, thus constraining the two M-O distances to be equal. Given this symmetry restriction, only two degrees of freedom are left in order to deform the geometry. Hence we scanned the potential energy surfaces along the coordinates given by the two lengths b and h, as in fig. 3.9, representing respectively the O-O bond length and the distance of the M metal from the O-O bond. The chemical character of the lower electronic state varies depending on the irreducible representation (irrep) to which it belongs. The three singlet states lying lower in energy belong to the a_1, b_1 and a_2 irreps, with varying ordering at different geometries. The symmetry of the states and of the active orbitals are summarized in fig. 3.9. The $^1A_1$ ground-state is a peroxide state, with symmetric occupations in the two oxygen frontier orbitals. On the other hand, the $^1A_2$ ground-state is a superoxide state, where the oxygen unpaired electron is placed in the π_x^* antibonding molecular obital. Additionally, the $^1B_1$ ground-state is also found to be of the superoxide kind, presenting a half-filled π_z^* molecular orbital. A representative description of the wave functions in terms of the leading CSFs is given in tab. 3.7, where configurations and weights are given respectively for each of the three state at near-minimum geometry.

In each of the irreps, the energy of the lowest state was obtained by applying the multi-

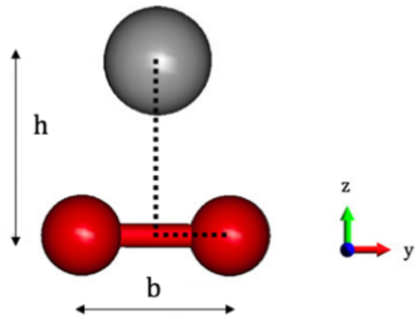

a_1	b_1	b_2	a_2
O p_z ($\rightarrow \pi_z$)	O p_z ($\rightarrow \pi_z^*$)	O p_x ($\rightarrow \pi_x$)	O p_x ($\rightarrow \pi_x^*$)
O p_y ($\rightarrow \sigma$)	O p_y ($\rightarrow \sigma^*$)		
Li s			

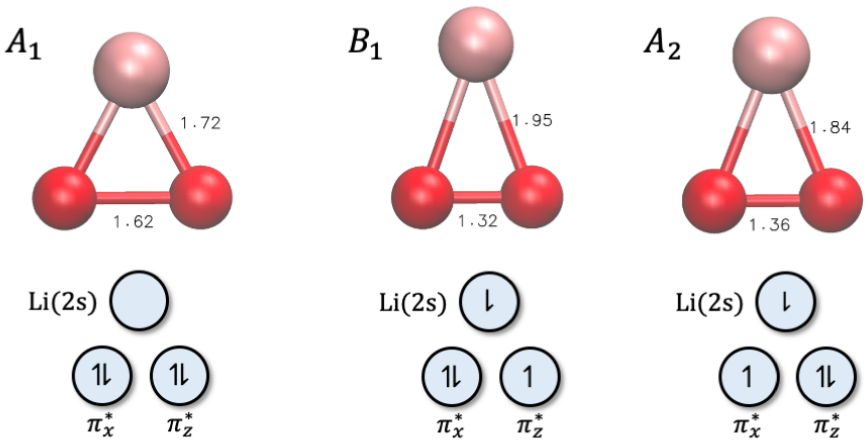

Figure 3.9: Electronic states of the LiO_2^- anion in the C_{2v} symmetry. The table on the top of the figure shows the transormation of atomic orbitals to molecular orbitals according to the properties of the different irreducible representation of the C_{2v} point group.

state (MS-CASPT2) formalism over a 3-roots SA-CASSCF wavefunction. This way, the diagonalization of an effective Hamiltonian yields a roots-mixing which corrects for what can happen to be a wrong interaction of states, inside the same irrep, at the uncorrelated CASSCF level. While irrelevant in the case of the a_2 and b_1 irreps, where there is no significant state-mixing, the multi-state procedure was found to be necessary for the $^1A_2$ state. In fact, due to the lack of dynamic correlation at the CASSCF level of theory, the ground-state wavefunction in the A_1 irrep is contaminated by mixing with higher roots, and the CASPT2 energy is consequently largely overestimated. An illustrative example is given by the CSF composition of the a_1 state at b = 1.55 Å and h = 2.00 Å. In the CASSCF eigenvectors, the first root present a strong mixing of the CSF nr.23 (the closed-shell configuration of the peroxide) and nr.28 (an open-shell configuration), with weights of 0.574 and 0.328 respectively. This wave function composition yields, after CASPT2 perturbative correction, a energy of -157.56784 Eh. After MS-CASPT2, the weights of

State	A_1			B_1		B_2	A_2	weight
$1a_1$	2	2	0	2	0	2	2	0.8868
$1a_2$	2	2	1	2	0	2	1	0.9973
$1b_1$	2	2	1	1	0	2	2	0.9994

Table 3.7: Leading CSF in the wave function of the three electronic states of LiO_2^-, at representative geometries (b=1.60 and h=1.50 for a_1, b=1.35 and h=1.75 for a_2, b=1.35 and h=1.85 for b_1.

the peroxide state are "purified" (0.940 for CSF nr.23 and 0.003 for CSF nr.28) and the energy is consequently lowered to -157.60073 Eh.

The potential energy surface of singlet states in the gas-phase, together with their relative color scales, are reported in fig. 3.10. In the LiO_2^- system the scanned values of the *b* and *h* coordinates span from 1.30 to 1.70 Å and from 1.45 to 2.05 Å, respectively. The A_1 state shows a wide minimum-energy region (dark purple), where the O-O bond is stable between 1.55 - 1.70 Å, and this corresponds to a short *h* distance around 1.5 Å. The large O-O distance clearly agrees with the peroxide nature of the O_2^{2-} moiety. On the other hand, the low-energy region in the A_2 surface is strongly localized inside the 1.30 - 1.35 Å range of *b*, which clearly characterizes it as a superoxide state. The equilibrium *h* distance is increased to about 1.7 Å, and it shows a much larger flexibility for the molecule in order to stretch along this parameter instead of *b*. A similar situation is found in the B_1 surface, another superoxide state. Here the purple area is restricted to even higher *h* values, around 1.9 Å, but, except for this deviation, the overall appearance of the surface shows little difference with respect to the A_2 one. Compared to A_1, the two superoxide states exhibits a narrow field of stability, and their energies rise (from purple to yellow) much more steeply, going from short to large *b*. This observation somehow recalls the potential energy curves of fig. 3.3, where the slope of the reactant (superoxide) curves is generally much larger than that of the intersected product (peroxide) curves. The minima in the maps perfectly agree with geometries optimized with CASPT2 numerical gradients in each of the irreducible representations. From the above observations, it is not only evident that peroxide and superoxide states in the LiO_2^- anion have strongly separated locations of their energy minima on the PES. Also, the different directions and rates in their energy rise suggests the occurrence of surface crossings at intermediate O-O values in between the respective ranges of stability. This feature can be highlighted by plotting energy-difference maps. The deep blue stripes in fig. 3.11 denote the set of points where the absolute difference $|E_i - E_j|$

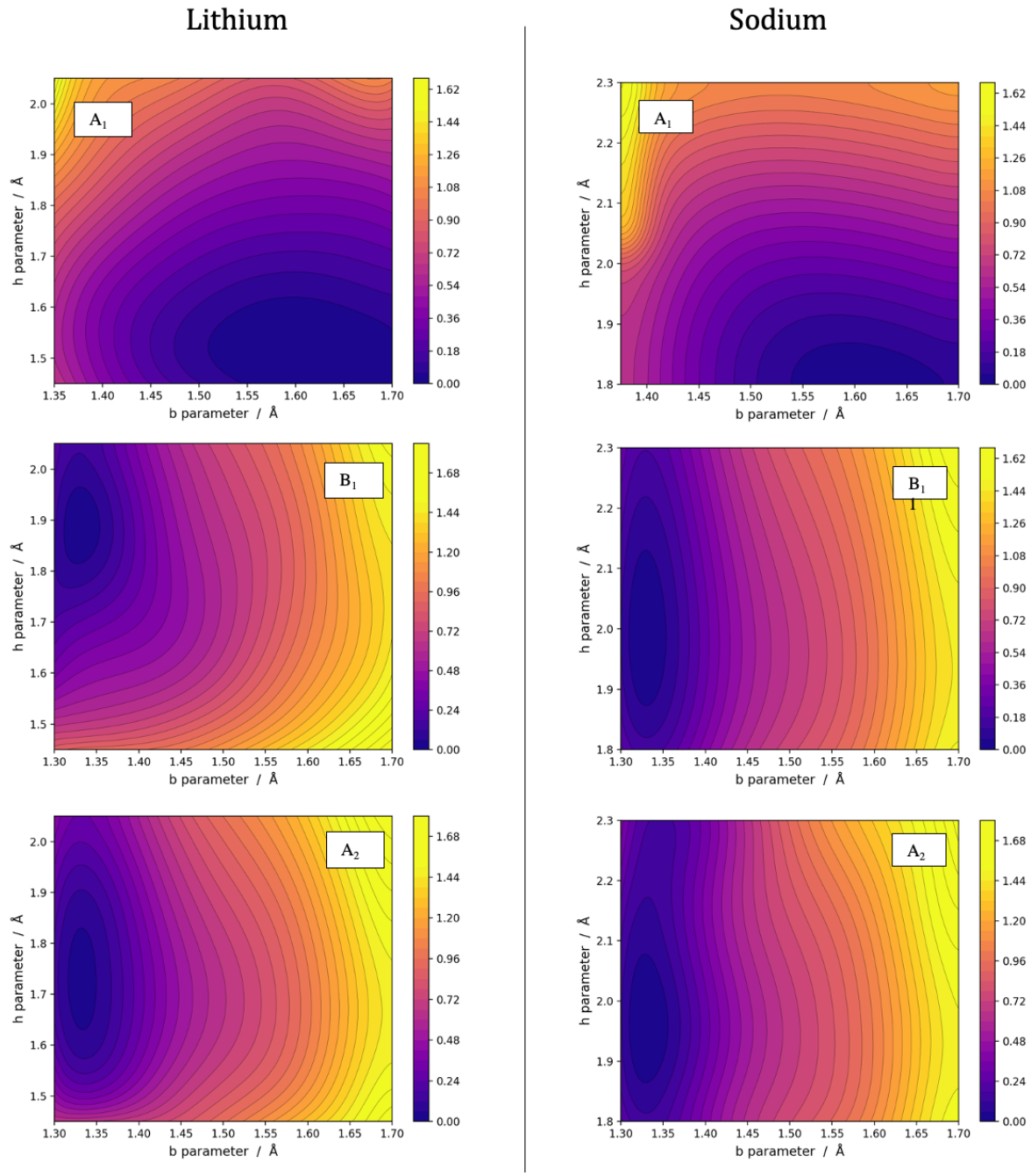

Figure 3.10: PES for the three electronic states of LiO_2^- (on the left) and NaO_2^- (on the right). In each panel, the lowest energy value has been set as the zero in the corresponding color scale.

between the energies of states *i* and *j* approaches zero, i.e. where the two states become energetically degenerate. A difference map between the two superoxide states (B_1/A_2) is absent, because the two surfaces are roughly parallel and the A_2 one is 0.5 - 0.7 eV eV lower in energy, hence they never approach each other inside the PES ranges we took into account. The A_1/A_2 crossing seam is well defined instead (left panel), and it is shifted at higher *b* values than the one relative to the A_1/B_1 couple (right panel), which is, again, a result of the B_1 state always being higher in energy than A_2. A clearer picture of how the ordering of the three states does change along the coordinate scan is given by the surface cuts in fig. 3.11 (right panels). In these graphs, the energies for each of the three states are reported together as functions of the *h* parameter, for *b* held fixed at selected values. The energy scale, on the left, is referenced to the lowest single-point energy in the A_2 PES, which is taken as zero. At $b = 1.40$ Å, the peroxide state is too destabilized, and none of the curves do intersect for almost all of the scan. Increasing *b* results in a first crossing between the A_1 and the B_1 states, until, for $b = 1.60$ Å, the peroxide state crosses also the second superoxide state (A_2) becoming the overall ground-state for small *h* values. At $b = 1.70$ Å the superoxide states are lifted so high in energy that A_1 remains undoubtedly the lowest state up to $h \sim 1.9$ Å.

The PESs for the electronic states of the NaO_2^- system (fig. 3.10, right panels) qualitatively reproduce the same features already seen in LiO_2^-. In this case, the ranges of stability are shifted to higher *h* values, because of the larger atomic radius of sodium, while the O-O distances remain approximately the same. Again, the purple areas in the A_1 PES span between 1.55 and 1.70 Å along the *b* axis, while those of the A_2 and B_1 states are limited inside the 1.30 - 1.35 Å range. These last are much more stable than the peroxide state, compared to the lithium PESs. In fact, looking at the energy-difference maps, the blue bands denoting null ΔE are found to be shifted on the far right of the plot, because the A_1 state starts to compete in energy only when the O-O distance is very favorable to form a peroxide. In the case of the A_1/A_2, the surfaces' intersections is displaced at such large O-O lengths that it barely appears in the bottom-right corner, at *b* close to 1.70 Å, where A_2 is extremely destabilized. This is clearly visualized by means of the surface cuts in the right-down panels of fig 3.11. At $b = 1.70$ Å the A_1 state becomes the lowest only for a very short *h* distance. When $b < 1.60$ Å, no intersections take place between peroxide and superoxide states. As with lithium, the surfaces of A_2 and B_1 are parallel over all the explored parameters' range.

The above discussion was entirely focused on singlet spin states of MO_2^{2-}. Corresponding triplet states of the same nature, i.e. representing a superoxide anion bound to a neutral M^0 metal, also do exist, and they simply consist in an alpha-alpha same-spin pairing of the two

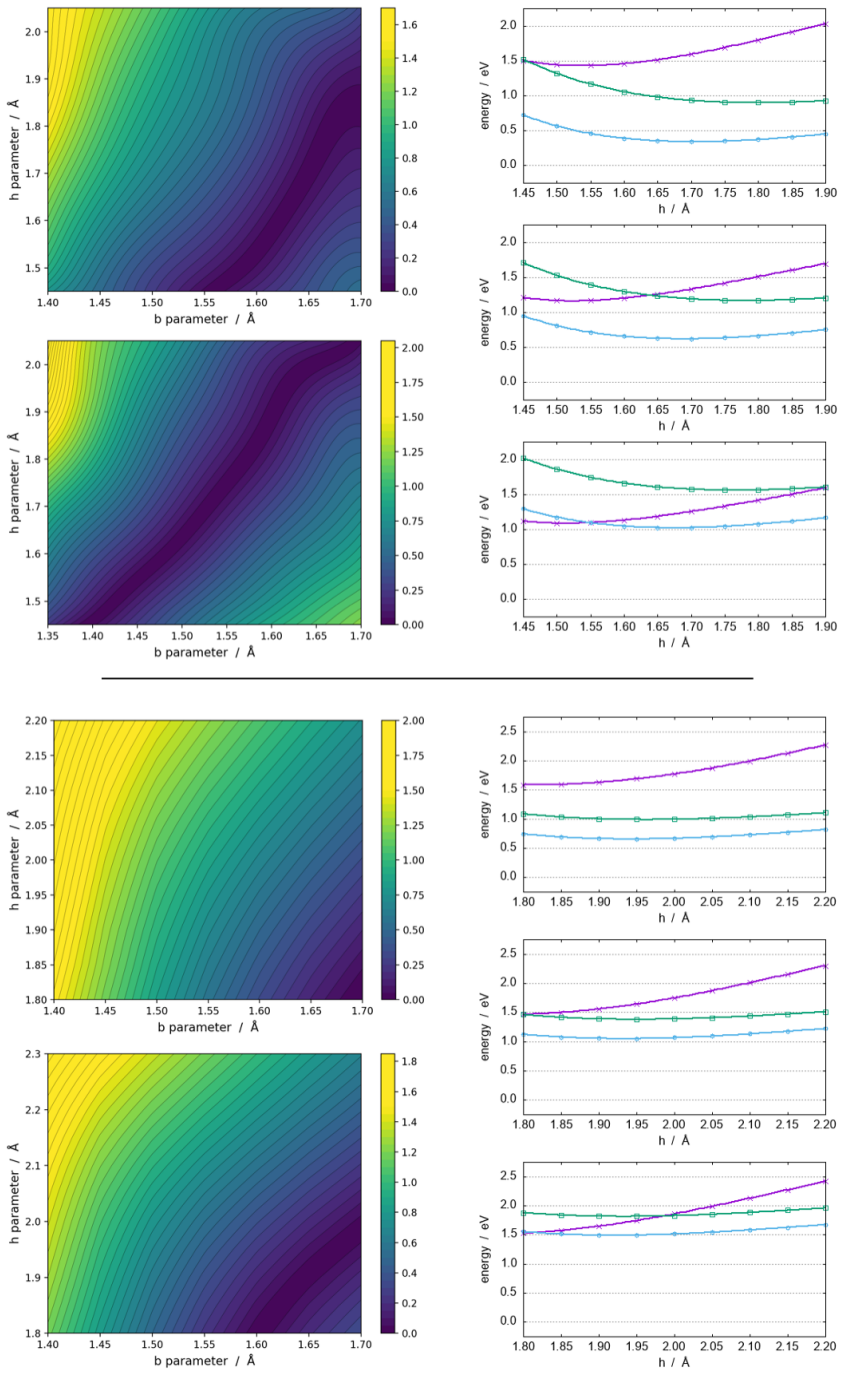

Figure 3.11: Intersection points of the electronic states. Upper panel refer to LiO_2^-, lower panel to NaO_2^-. The energy-difference maps, on the left, highlight the locus of points where the two states (A_1-A_2 above, A_1-B_1 below) become degenerate in energy. On the right, cuts of the three PESs at different values of b: 1.40, 1.50 and 1.60 Å for the upper panels, 1.50, 1.60 and 1.70 Å for the lower panels

unpaired electrons, that is, the one on the O-O moiety and the one on the metal. These two superoxide states, in the triplet and singlet multiplicity, are almost degenerate in energy. This closely recalls the situation encountered with the potential energy curves of $[MO_4]^-$ dimeric superoxides (fig. 3.12, left panels), where the energies of singlet and triplet reactants almost coincide along the NEB minimum energy path. A possible electronic transition from the closed-shell singlet state of the peroxide would be spin-forbidden. Looking at the left-hand sides of eqs. (3.9) and (3.10), the overall spin multiplicity must be singlet or triplet. Therefore, a triplet state in the M_O^{2-} product can only arise in case of singlet O_2 formation.

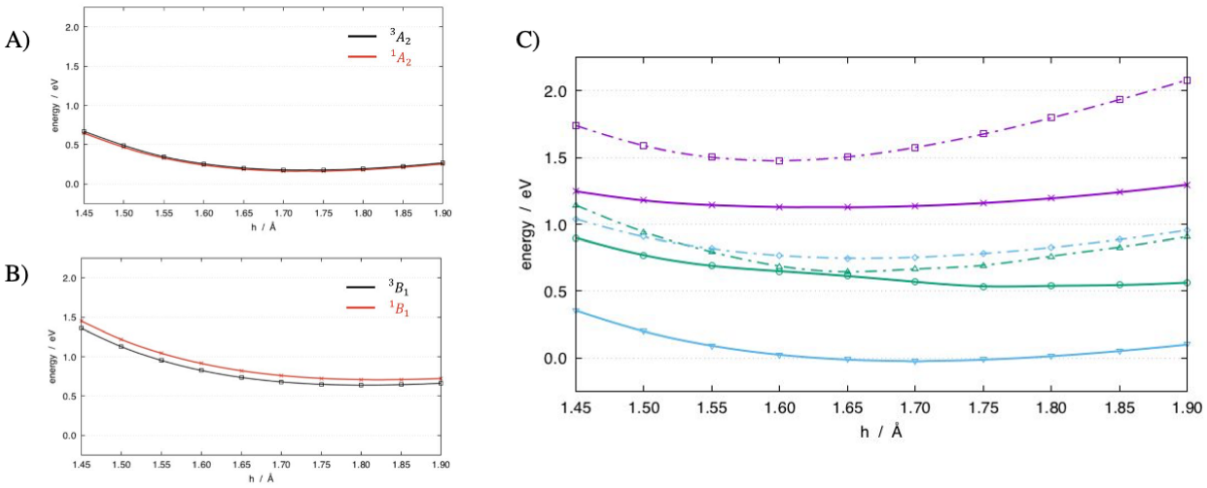

Figure 3.12: Additional tests for checking the A) inclusion of triplet states, and B) the enlargement of the active space to include the metal *n*p orbitals (see the text for details).

The [10,7] active space for a system of three light atoms can be generally considered exhaustive, given that it allows to represent all the chemically significant configurations for the phenomena of interest. Nevertheless, a test was appropriate in order to check if the selected orbitals provided a sufficiently flexible basis for representing the most relevant electronic states. Therefore, because of the 2p orbitals of Li being close in energy to the 2s, a larger [10,10] active space was tested, including all the valence orbitals of lithium. Taking into account a total of six low energy states from all the four irreps, three "new" states appear, belonging to the a_1, b_1 and a_2 irreps. Even in the the extended active space, only high energy states belong to the b_2 irrep, so they are discarded from our analysis. The three new states all correspond to a reduced-metal superoxide, with a singly occupied p_x, p_y or p_z Li orbital, and will be addressed as $2A_1$, $2B_1$ and $2A_2$ (dashed lines). The potential energy curves in fig. 3.12 (right panel) represent the cuts of all the six PESs together, at a representative O-O bond length (b = 1.40 Å). As expected, the occupation of the 2p

orbitals of Li do not contribute to lower the energy of the reduced-metal product. The superoxide ground-state $1A_2$ (cyan, full line), which corresponds to a $(2s)^1$ occupancy, lies more than 0.5 eV below the energy of the $2A_2$ state (cyan, dashed line), whose energy surface just results to be shifted upwards. Similarly, the $2A_1$ state (violet, dashed line) lies at higher energies than the $1A_1$ one, but the two respective surfaces run almost in parallel. The two B_1 states (green), instead, arising from either a $(2s)^1$ or $(2p)^1$ occupation, are close in energy and interact when *h* is between 1.45 and 1.65 Å. Nevertheless, since the $1B_1$ state already represent an electronically excited superoxide, the inclusion of this second $2B_1$ is of minor relevance for the chemistry of the LiO_2^- system. The weight of singly occupied $(2s)^1$ configurations dominates the lowest superoxide state, hence the [10,7] active space is sufficient for the purposes of determining the chemical nature of the ground-state in the LiO_2^- system at different geometries. A similar conclusion, for the sake of comparison, was outlined in ref.[225], where Li 2p orbitals are reported not to play a significant role in the homolytic dissociation of the OO-Li bond leading to either an isolated Li^+ cation or Li^0 atom.

The discussion on potential energy surfaces so far was limited to the molecule in vacuo. An implicit solvent was therefore introduced into the model by means the PCM method, using the parameters of diethyl ether for consistency with the previous calculations. As already seen in the case of single-point energies of optimized structures, the dielectric continuum rises the energy of low charge-separation states with respect to high charge-separation and superoxide surfaces are accordingly lifted. As a result, the surface crossings are strongly shifted towards the left of the energy difference-maps, closer to the minimum energy zone of the superoxide states, while the shape of the surfaces remains approximately unaltered. In LiO_2^- only the A_2 PES is low enough to barely intersect with A_1 inside the same range of *b* of the previous plots. Both of the A_1/A_2 and A_1/B_1 crossing seams are visible for NaO_2^-, but placed at *b* lengths well shorter than in vacuum. This is in agreement with the previous observations on the metal-reduction channel: when a low-polarity solvent is introduced, the superoxide-M^0 keeps to be competitive with the disproportionation channel only for sodium (and potassium), but not for lithium.

According to the 3N - 6 rule, the triatomic MO_2^- system has 3 vibrational normal modes, but the C_{2v} symmetry only accounts for two of them, i.e. those that don't break the symmetry across the C_v reflection plane, keeping the two M-O distances constrained to be equal. A third normal mode, however, would move the M atom out of the symmetry plane, thus lowering the point group to C_s. For this reason, we examined again the electronic states of LiO_2^- in the C_s symmetry group. This point group only has two distinct irreps: *a*' and *a*". Of the four C_{2v} irreps, a_1 and b_1 degenerate into *a*' while a_2 and b_2 degenerate into *a*". We

introduced α as a third degree of freedom, describing the angle of deviation between the b and h segments from 90°. For small values of α, the deviation from the C_{2v} symmetry do not alter the three PESs significantly. As a general trend, this has the effect of lowering the superoxide states with respect to the peroxide state. The main difference concerns the behaviour at the crossing regions. While the A_2 and the A_1 still belong to different irreps and are then allowed to intersect each other, the latter is now an A' state as it is also B_1. Hence, the two states can interact and their intersection becomes forbidden by symmetry. An avoided crossing is therefore observed in fig. 3.13 (left panels), where the two PES are cut at a representative value of b = 1.45 Å for increasingly larger α angles (0°, 5° and 10°). This suggests that the crossing points in the C_{2v} symmetry (fig. 3.11) should actually live on the seam of a conical intersection. The C_s symmetry cannot be further lowered just by geometrical distortion, for the triatomic system will always lie on the reflection plane. Thus, in order to couple the A' and the A" states (that is, the A_1 and A_2 states in the C_{2v} point group), the symmetry through the molecular plane has to be lowered by perturbation of the wave function. Fig. 3.13 (right panels) reports the effect of an external electric field applied perpendicular to the molecular plane, when b = 1.60 Å and α = 10°. A small avoided crossing between the curves is then seen to occur at h close to 1.50 Å.

3.1.5 Discussion

From the above results, singlet oxygen can form, in principle, from two different reactive pathways of alkali superoxides. Factors like the metal chemistry, the solvent polarity and the ionicity of the reactants are found to impact the disproportionation and the metal-reduction channels in different ways. What follows is a deeper discussion on the key results of this part of our theoretical investigation, whose aim is to complement the experimental evidences.

For what concerns the disproportionation channel, the presence of a second cation was overall found to ease the chemical process in terms of reaction ΔG, although the ionicity of the disproportionation, i.e. the prevalence of a ionic or neutral mechanism, can be at least in part determined by the dielectric constant of the solvent. When the dielectric constant is low, the $[M_2O_4]$ complexes can release molecular oxygen much more easily than $[MO_4]^-$ complexes can do. Anyway, as it is seen switching from Et_2O to CH_3CN, the higher the dielectric constant, the smaller is the difference in the energy required to release O_2 between the two different mechanisms. In the limit of highly polar solvents, the anionic reaction should therefore become favored. As pointed out in sec. 1.1.4, experiments suggest, at least for Li, that in solvent with high dielectric constant like DMF (ϵ = 37) and DMSO (ϵ = 46) the reaction proceeds faster in the presence of just one metal cation[87],

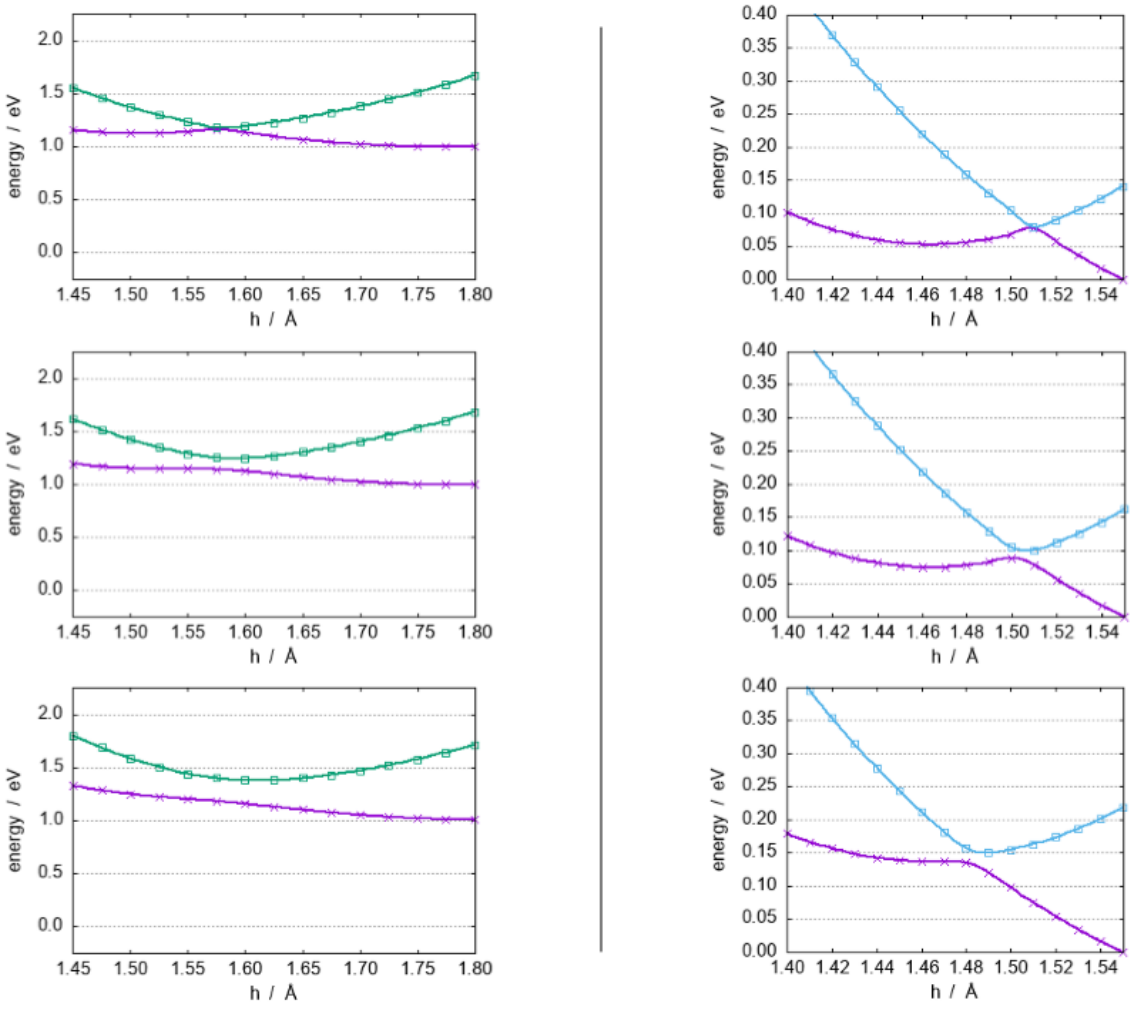

Figure 3.13: Avoided crossings when lowering the symmetry of the system. On the left: the interaction between the A_1 and B_1 states when lowering the symmetry to C_s, for increasing value of distortion of the triangle. On the right: the interaction between the A_1 and A_2 states when an electric field of intensity 0.1 (in atomic units) is directed perpendicular to the plane of the molecule.

and this agrees with our qualitative conclusions. Additionally, two more hypothesis can be drawn in order to explain the ionic mechanism observed experimentally. First, ionic transport through the electrolyte can be a decisive limiting factor. Despite the favorable thermodynamics, the neutral reaction (eq. 3.3) requires the transport of a second M^+ cation to form another ionic pair with a free superoxide, before the reactive dimer complex can form. This additional transport would thus represent a kinetic limitations which overcomes the thermodynamic factor. Another possible argument in favor of the anionic reaction may reside in the electron-transfer rate. ET reactions, even when non light-assisted, can be very fast events whose timescale can fall below the order of picoseconds[226,227]. If the transfer rate is high enough in order to induce the disproportionation before the superoxide $[MO_4]^-$ or $[M_2O_4]$ dimer can thermally relax in the solvent, then it can reach the energy well of the products without losing the whole excess energy. This way, the positive barrier encountered in reacs. (3.7-3.8) is overcome with a far less endoergic income, so that the thermodynamic advantage of the neutral mechanism over the anionic mechanism is significantly levelled. In this scenario, the anionic disproportionation of potassium superoxide, which has the less exoergic path to form the superoxide dimer following eq. 3.2, still has to exceed more than 1 eV in order to form peroxide and oxygen from KO_2 and O_2^-, which is higher than lithium and sodium, a circumstance that agrees with the experimental trends. If the relaxation time-scale of the pre-reaction complex is a key factor, a major role is then played by the solvent structure around the reactant. Anyway, in order to study the varying of relaxation times in different solvents, for example through vibrational relaxation, it would be required to study the dynamics of an extended portion of explicit solvent, something which at present is out of the scope of this thesis. With alkaline-earth metals, the trend against solvent polarity is reversed. Disproportionation of MgO_4 and CaO_4 is thermodinamically favored in solvents with a large dielectric constant. When ϵ is low, instead, the last reaction step requires more than 1 eV of energy, making disproportionation at room temperature hardly relevant.

These considerations on the polarity of the solvent also apply to the production of singlet oxygen. In weakly polar solvents, the neutral mechanism is expected to prevail, leading to a favorable disproportionation thermodynamic so that $^1O_2$ formation becomes feasible with less than 1 eV in LOBs. On the other hand, increasing the dielectric constant of the solvent shifts the reaction towards the ionic mechanism, with higher energy barriers which prevent a relevant release of $^1O_2$ by alkaline cations. In our calculations, the disproportionation is predicted to be most effective when assisted by H^+ ions. The HO_2^- product is more stable than any of the alkali MO_2^- or MO_2 peroxides, lowering the threshold for $^1O_2$ production well below 1 eV over the $[HO_4]^-$ energy. Interestingly, the trend toward the dielectric constant of the medium goes in the opposite direction for protons: a higher ϵ enhance the exoergicity

of the disproportionation and allows $^1O_2$ to form with a little barrier, in the order of only 0.1 - 0.2 eV for CH_3CN solvent (see fig. 3.4). Hence, when a solvent with high polarity is used, most of the singlet oxygen release arising from disproportionation of alkali superoxides will be suppressed, but, at the same time, its fraction due to protic contamination, if present, will be boosted. As with protons, divalent Mg^{2+} and Ca^{2+} cations also encounter less positive ΔG with the solvent medium has a higher dieletric constant. Those solvents are then expected to increase the $^1O_2$ yield in alkaline-earth MOBs.

When the anionic mechanism drives the disproportionation of alkali superoxide, the MO_2^- peroxide anion is formed as a discharge intermediate, which opens up for the metal-reduction channel to compete under certain conditions (see previous section). Not only this additional reactive pathway can lead to the release of singlet O_2 with lower energy than that required to form it through disproportionation. Regardless of the electronic state of the evolved O_2 gas, the superoxide-$M^{(0)}$ specie contains a reduced metallic center, which can itself represent a source of parasitic chemistry. In fact, neutral alkali metal atoms are known to be strong reducing agents, and we suggest that the presence of free ions carrying $M^{(0)}$ in the bulk or at the electrode can represent the onset for additional side-reactions and degradation. Considering both $^1O_2$ and $M^{(0)}O_2^-$ species as potential initiators of parasitic reactions, fig. 3.14 summarizes the possible landscapes for generating a most stable onset degradation reactant (ODR) in Li-O_2, Na-O_2 and K-O_2 systems (the data here are referred to a diethyl ether model solvent). Starting from the MO_2 + O_2^- reactants on the left, all of the ODR require at least 1 eV or more, making the activation of these reactive channels unlikely at room temperature. Anyway, it must be considered that, under the operating conditions of the electrochemical cell, overpotentials are required in order to overcome ionic transport resistance and activation energies. If a direct energy transfer takes place from the polarization overpotential to the internal energy of the reactive species, extra energy will be available for climbing the activation energy hills[228,229]. This assumption is rough, but it qualitatively reflects the out-of-equilibrium regime of a polarized electrode with flowing current. Considering the potentials of the respective O_2/MO_2 redox couples (see tab. 1.1.1), the overpotentials required in order to reach the ODR energy would be as low as >0.4 V in the case of Li-O_2, >0.1 V for Na-O_2 and >0.2 V for K-O_2.

The likelihood of such reduced-metal products is strongly related to the presence of a second cation, which strongly stabilizes peroxide-like products, as already mentioned. Hence, the aggregation of M_2O_2 is certainly expected to result in the predominant formation of peroxide clusters. Free MO_2^- anions can nevertheless form as $M^{(0)}O_2^-$ isolated species in solution and survive long enough to impact the cell chemistry, before they can form M_2O_2 upon ionic transport and then precipitate. Conversely, if produced at the cathode as a result of

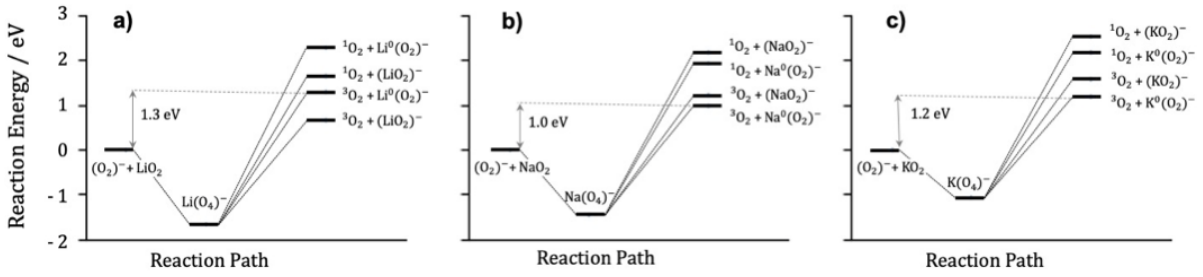

Figure 3.14: Competition of the disproportionation and metal-reduction channels leading to ODR (see text for details).

the electroreduction of already formed MO_2 (the surface mechanism in the ORR, see sec. 1.1.3), the $M^{(0)}O_2^-$ product could also alter the mechanism of deposition and growth of the discharge products. A direct experimental evidence, although not in the scope of the present thesis project, would be mandatory in order to assess and discuss this unknown reactive channel. A possible experimental technique to tackle the the transient formation of $M^{(0)}$ species is by in-operando nuclear magnetic resonance spectroscopy. In fact, NMR allows to discriminate magnetic centers in different bonding environments, and in the last years 7Li NMR has been increasingly used to study the electrochemistry of metal-ion and metal-air batteries[230–233]. It is worth to recall that evidences of an internal instability of the electronic state in peroxide phases to form superoxide are already known in the literature. Li_2O_2 clusters are predicted to present mixed oxidation states, over a given size[234], and the presence of superoxide-like moieties in bulk Li peroxide was experimentally proved[235]. Also, the order of stability K > Na > Li to form a reduced neutral metal atom, in spite of being reversed with respect to the redox potentials of the alkali series, is not unprecedented. For instance, experimental data on the dissociation of the O-M bond in alkali superoxides agree with this trend, with bigger alkali metals showing smaller homolytic dissociation energy to form O_2 and a neutral metal[236,237]. Estimates of bond dissociation energy by flame combustion can be affected by significantly large error, but they agree, at least qualitatively, with our predicted trend. This result is also validated by theory, in the computational study by Zaichenko et al.[225] which employs multireference ab-initio calculations on the same dissociation process.

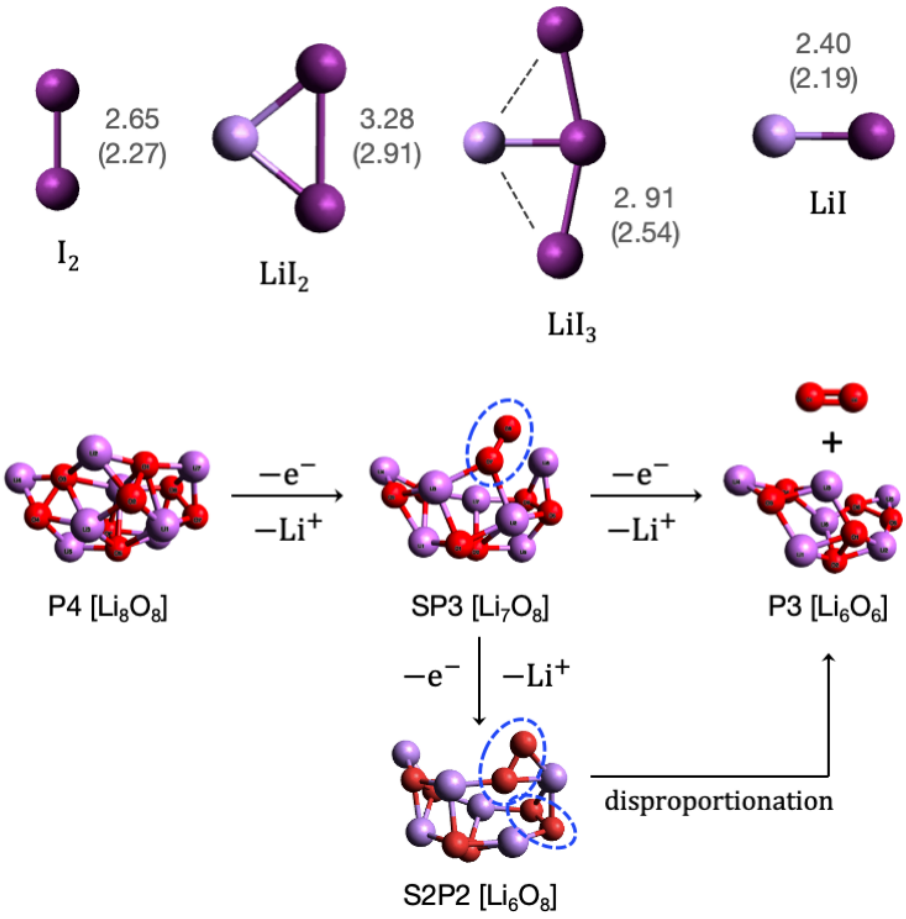

Figure 3.15: Optimized geometries at the B2PLYP level. The bond lengths in parenthesis (upper part) are those of the corresponding bromine species. The dashed circles around specific O-O bonds in the cluster (lower part) identify superoxide-like moieties.

3.2 Mediated Oxygen Evolution Reactions

3.2.1 Structures of RMs and peroxide clusters

Halogen redox systems can be employed as redox mediators by adding halide salts to the electrolyte. At charging, the X^- halide is converted into the oxidized form, which is the one which chemically reacts with the discharge products. Iodine and bromine present a number of molecular species with different oxidation states, and the nature of the actual oxidized form depends on the oxidation potentials of the relative redox couples, which in turn are highly sensitive with respect to the solvent. For this reason, a unified mechanism for redox mediators based on iodine or bromine is not yet defined, and ambiguities hold about which

redox couple should be expected to act as redox mediator at a given electrolyte composition and at given voltage. Here, the relevant species taken into account are, in order of increasing oxidation number: X^-, X_2^-, X_3^-, X_2. Iodine is also known to form stable higher polyiodide (like X_5^- and X_7^-), which are not considered here. The calculations have been carried out both in vacuo and in implicit solvent, through the SMD continuum model. For SMD, the built-in parameters of diethyl ether were adopted, to mimic the low-polarity glymes usually employed in Li-O_2 cells. The two DFT functionals, B2PLYP and ωB97X-D3, have both been used. Minimum energy geometries have been optimized using a def2-TZVP basis set, which introduces effective-core potentials to replace the core electrons of I atoms; a non-relativistic Hamiltonian is therefore used. Here we took into account the four redox semireactions:

$$X_2 + e^- + Li^+ \longrightarrow LiX_2 \tag{3.11}$$

$$X_2 + 2\,e^- + 2\,Li^+ \longrightarrow 2\,LiX \tag{3.12}$$

$$X_2{}^- + e^- + 2\,Li^+ \longrightarrow 2\,LiX \tag{3.13}$$

$$X_3{}^- + 2\,e^- + 3\,Li^+ \longrightarrow 3\,LiX \tag{3.14}$$

The optimized geometries of the respective iodine species are depicted in fig. 3.15 (upper part). In parenthesis are also given the interatomic distances of the corresponding bromine-based species.

In order to explore the oxidative process of the discharge products, the insoluble nature of lithium peroxide in most of the solvents adopted must somehow be taken into account. Periodic simulations typically limit the level of theory which can be adopted; moreover, results have a non-trivial dependency on the structure of the bulk and the surface. In order to be consistent with the level of theory adopted, a simplified approach oriented toward molecular clusters. A tetramer Li_2O_2 peroxide cluster is used here as a simplified model of the discharge products, which allows to consider different oxidation pathways. This size has been already been considered in previous studies[238,239], and has proved to be a useful representation also for bigger, nano-sized model clusters[234]. A central topic in the discussion of the mechanism of mediated oxidation of alkali peroxide to molecular oxygen is whether it takes place by direct oxygen evolution (two-electron process) or by sequential oxidation to superoxide and then to molecular O_2 (two one-electron processes). If a direct two-electron oxidation occurs, then O_2 is liberated from P4 to form P3 without mixed peroxide/superoxide intermediates. This hypothesis has been discarded in the general case, as motivated e.g. in ref.[182]. If, on the contrary, the mediated oxidation is a sequence of

one-electron processes, de-lithiated species are expected to form, thus maintaining the electroneutrality of the cluster as electrons are withdrawn from peroxides to form superoxides. Hence, four kinds of clusters have been considered:

- $(Li_2O_2)_4$, abbreviated as P4, is a spin singlet;
- $(LiO_2)(Li_2O_2)_3$, abbreviated as SP3, is a spin doublet;
- $(LiO_2)_2(Li_2O_2)_2$, abbreviated as S2P2, is a spin triplet (or singlet);
- $(\ Li_2O_2)_3$, abbreviated as P3, is a spin singlet.

The complete oxidation of one Li_2O_2 to molecular oxygen leads from a starting P4 cluster to P3 plus a free O_2 molecule, as represented in the scheme of fig. 3.15 (lower part). The two clusters SP3 and S2P2 are, respectively, singly and doubly de-lithiated structures that represent possible intermediates in the oxidation process from P4 to P3. The optimization procedure of the clusters was as follows. For each type of the four types of clusters, a large number of initial configurations is generated and subsequently optimized at low-cost sempiempirical GFN2-xTB level of theory. The structures whose energy lie within a range of 100 mHa from the most stable one were then re-optimized with both the B2PLYP and the ωB97X-D3 functionals, with a def2-TZVP basis set. The lowest-energy structure is then taken as the final minimum geometry, and a frequency calculation is performed to evaluate the Gibbs free energy (at 298 K).

3.2.2 Oxidative routes

Spontaneous de-lithiation by electrochemical oxidation has already been studied[238]. Here we focus on the process where electron-transfer is accompanied by cation abstraction:

$$(RM)^+ + Li_2O_2 \longrightarrow (RM)Li^+ + LiO_2 \tag{3.15}$$

$$(RM)^+ + LiO_2 \longrightarrow (RM)Li^+ + O_2 \tag{3.16}$$

This can be regarded as a similar process to what happens in proton-coupled electron transfers. Moreover, Chen et al.[240] came to the conclusion that, with most redox mediators, oxidation of Li_2O_2 is mainly an inner-shell process, involving the adsorption of the mediator on the peroxide surface. Therefore, in analogy with inner-shell electron transfers of coordination complexes, which occur via exchange of a bridging ion between the two redox active centers, an analogous inner-shell mechanism can be proposed here: Li^+ cations act

n.	peroxide oxidation (1 e^-)	ΔE_{gas}	ΔE_{SMD}	ΔG_{gas}	ΔG_{SMD}
1	I_2 + P4 → LiI_2 + SP3	+0.74	+0.53	+0.49	+0.27
2	I_2 + SP3 → LiI_2 + S2P2	+0.77	+0.67	+0.53	+0.41
3	I_2 + P4 → 2LiI + S2P2	+1.91	+0.88	+1.12	+0.06
4	LiI_2 + P4 → 2LiI + SP3	+1.14	+0.20	+0.59	-0.35
5	LiI_2 + SP3 → 2LiI + S2P2	+1.18	+0.35	+0.63	-0.21
6	LiI_3 + P4 → 3LiI + S2P2	+2.23	+1.08	+1.03	-0.13
n.	peroxide oxidation (2 e^-)	ΔE_{gas}	ΔE_{SMD}	ΔG_{gas}	ΔG_{SMD}
7	I_2 + P4 → 2LiI + P3 + O_2	+3.18	+1.69	+2.01	+0.56
8	LiI_3 + P4 → 3LiI + P3 + O_2	+3.43	+1.90	+1.91	+0.37
n.	superoxide oxidation (1 e^-)	ΔE_{gas}	ΔE_{SMD}	ΔG_{gas}	ΔG_{SMD}
9	I_2 + SP3 → LiI_2 + P3 + O_2	+1.97	+1.49	+1.42	+0.91
10	LiI_2 + SP3 → 2LiI + P3 + O_2	+2.38	+1.17	+1.52	+0.29

Table 3.8: B2PLYP reaction energies (in eV) of iodine oxidant species with different clusters. SMD indicates energies calculated in implicit diethyl ether solvent.

as a bridging moiety which coordinates the oxidized RM and the reduced oxygen and is then exchanged to the reduced RM. In our work this founds justification by the fact that the association energy of Li^+ cations with anionic RM^{red} species is always negative in our calculation. So we will consider the products as contact ion pairs, as in the redox couples of eqs. (3.11-3.14). In the real system, compounds like LiX and LiX_2 may be present as dissociated ions, providing an additional thermodynamic driving force.

Tables 3.8 and 3.9 summarise the energy of iodine-RM and bromine-RM reactions, respectively, with peroxide clusters. The discussion will focus exclusively on the fourth column, reporting Gibbs free energy in the continuum solvent model (again, the parameters of diethyl ether were employed). Two major observations can be drawn from these data. In first place, peroxides and superoxides react with bromine species through more exoergic or less endoergic reactions than with iodine species. This point is not surprising, since Br is known to be a better oxidant than I, and the redox potentials of halogen redox couples generally increase going up along the periodic table from I to F. Although this positively affects the oxidant power of the Br mediators, reversibility requires higher charging voltages, stepping into the voltage window of chemical instability of cathodic materials (see sec. 1.2.1). Secondly, it is found that partially reduced X_2^- species, which should be formed upon

n.	peroxide oxidation (1 e^-)	ΔE_{gas}	ΔE_{SMD}	ΔG_{gas}	ΔG_{SMD}
1	Br_2 + P4 → $LiBr_2$ + SP3	+0.33	+0.04	+0.05	-0.22
2	Br_2 + SP3 → $LiBr_2$ + S2P2	+0.36	+0.19	+0.09	-0.08
3	Br_2 + P4 → 2LiBr + S2P2	+1.00	+0.06	+0.21	-0.76
4	$LiBr_2$ + P4 → 2LiBr + SP3	+0.64	-0.14	+0.10	-0.68
5	$LiBr_2$ + SP3 → 2LiBr + S2P2	+0.68	+0.01	+0.14	-0.54
6	$LiBr_3$ + P4 -> 3LiBr + S2P2	+2.23	+1.08	+1.03	-0.13
n.	peroxide oxidation (2 e^-)	ΔE_{gas}	ΔE_{SMD}	ΔG_{gas}	ΔG_{SMD}
7	Br_2 + P4 → 2BrI + P3 + O_2	+2.29	+0.87	+1.08	-0.26
8	$LiBr_3$ + P4 → 3LiBr + P3 + O_2	+3.43	+1.90	+1.91	+0.37
n.	superoxide oxidation (2 e^-)	ΔE_{gas}	ΔE_{SMD}	ΔG_{gas}	ΔG_{SMD}
9	Br_2 + SP3 → $LiBr_2$ + P3 + O_2	+1.56	+1.01	+0.98	+0.42
10	$LiBr_2$ + SP3 → 2LiBr + P3 + O_2	+1.88	+0.83	+1.03	-0.04

Table 3.9: B2PLYP reaction energies (in eV) of bromine oxidant species with different clusters. SMD indicates energies calculated in implicit diethyl ether solvent.

the transfer of just one electron from the reduced substrate to X_2, are the most reactive species. For instance, the difference between the ΔG in reactions 1 and 4 of table 3.8 is about -0.6 eV for iodine and -0.4 eV for bromine (table 3.9). This means that, whenever X_2^- is formed upon reduction of X_2, it is readily able to react again, instead of being re-oxidized at the electrode back to X_2, which is less reactive. Therefore, a full oxidation route can be supposed to carry from P4 to P3 through both the radical intermediates I_2^- (or Br_2^-) and SP3 (superoxide), with eqs. 3.11 and 3.13 summing up as a two-step equivalent to eq. 3.12.

Two-electron oxidations without superoxide intermediates are also reported in rows 7 and 8, though, as already pointed out many times, such a process is not believed to take place, for kinetic reasons. Additionally, X_2 and X_3^- species can undergo a 2-electron reduction by oxidizing two different peroxide moieties to superoxide, i.e. forming S2P2 out of P4 (rows 3 and 6). Such a process would still produce the intermediate superoxide species which are actually detected by experiments, though the kinetic could still suffer for high activation barriers. These reactions are both exoergic for Br_2 and Br_3^-, whilst only I_3^- forms S2P2 spontaneously (the reaction with I_2 is slightly endoergic).

3.2.3 Spin-orbit couplings

If spin multiplicity has to be conserved along any of the oxidation pathways, the reaction outcomes must enforce rigid limitations on their possible spin states. The initiation of Li_2O_2 oxidative decomposition is particularly relevant from this point of view. Assuming that the initial redox mediator in its oxidized form, be it either as X_2 or X_3^-, is in a singlet spin state, the products of the reaction with Li_2O_2 are expected to be a global singlet as well. In principle, this reaction can be either a direct two-electron oxidation that yields O_2, or a one-electron oxidation to form LiO_2 superoxide intermediate. We will consider only the latter process, since the former has been generally discarded by most of literature. If the products LiX_2 + LiO_2 have to form a global singlet, a subsequent reaction of these two species to form X^- halide plus O_2 (table 3.8 row 10) would again bring to a final singlet product. This would inevitably imply the formation of $^1O_2$, if the system is provided with enough energy to reach this excited state. This scenario undoubtedly sheds a negative light on the perspective of using halogen/halide redox mediator for suppressing the release of $^1O_2$, unless a spin transition mechanism is present that allows the formation of ground-state $^3O_2$. In order to investigate such a possibility, we studied the spin-orbit coupling (SOC) between triplet and singlet spin-pure states in the reaction:

$$X_2 + Li_2O_2 \longrightarrow LiX_2 + LiO_2 \tag{3.17}$$

What we are interested into is a qualitative answer about the possibility of heavy atoms (I, Br) to allow intersystem crossing. We therefore take into account a simplified model system made of only one I_2 and one Li_2O_2 molecule. Upon the encounter of the two reactant species, a singlet pre-reactive complex is expected to form, as in fig. 3.16. According to [187], such a complex can transit to a triplet state following a mechanism similar to that of $^1O_2$ quenching (see section 1.2.5). We therefore focused on the study of the iodine-peroxide and bromine-peroxide $X_2 \cdots Li_2O_2$ complexes (abbreviated as IPC and BPC) and their excited electronic states.

These calculations are based on a time-dependent DFT (TDDFT) approach, which offers a convenient alternative, although not equally reliable, to MRCI spin-orbit coupling calculations on heavy atoms with full-core electrons. The range-separated hybrid ωB97X-D3 functional is employed, which is proved to perform well not only for ground-state calculations but also when dealing with charge-transfer states [241], which are a notorious challenge for GGA and hybrid functionals. The complex was first optimized with the aforementioned functional, using a def2-TZVP basis-set with effective core potentials on I atoms, and vibra-

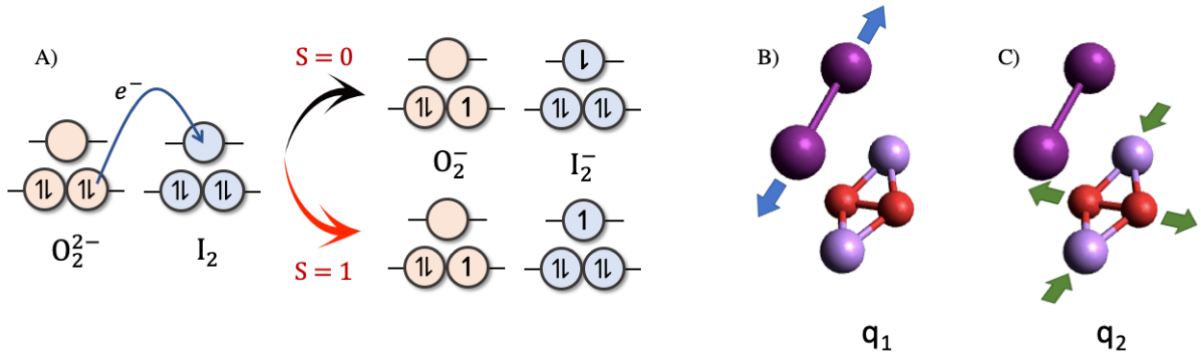

Figure 3.16: Scheme of the oxidation of Li_2O_2 by I_2. A) The transfer of one electron from the peroxide to iodine produces two radical species which can couple as a global singlet (spin allowed) or triplet (spin forbidden). B) Representation of the q_1 normal mode of vibration. C) Representation of the q_2 normal mode of vibration.

tional normal modes where then calculated. Among the 18 normal modes, two were selected for they produce the most relevant atomic displacements required for the reaction to proceed to form I_2^- and O_2^-. Based on the previous experience with the reaction coordinate of the superoxide disproportionation (see section 3.1.2), these two normal modes are expected to be those corresponding to the elongation/shortening of the O-O and I-I bonds. In both complexes, the vibrational mode nr. 13 corresponds to the stretching of X-X (229 cm^{-1} in IPC and 344 cm^{-1} in BPC), and this will be indicated as the q_1 normal coordinate. The vibrational mode nr. 18, instead, corresponds to the O-O stretching (867 cm^{-1} in both IPC and BPC), accompanied by the estrangement of the two Li^+ cations, and will be denoted as q_2. A number of molecular structures was therefore projected along q_1 and q_2 simultaneously, both in the positive and in the negative directions of the coordinate, thus generating a bi-dimensional grid of structures which has the equilibrium geometry of the complex at its center. At each point of the grid, a TDDFT calculation was performed with 5 singlet and 5 triplet roots. These are relativistic, full-electron calculations, which employ the DKH-def2-TZVP basis set (replaced by SARC-DKH-TZVPP for I atoms) and the second-order Douglas-Kroll-Hess (DKH2) relativistic Hamiltonian. Spin-orbit couplings were calculated between states of different multiplicity, through quasi-degenerate perturbation theory[242] as implemented in the package Orca 5.0.3. Fig. 3.17 reproduces two significant cuts of the energy surfaces of IPC, one along q_2 (upper panels) and the other along q_1 (lower panels). The dimensionless units on the x-axes are arbitrary displacement units, obtained by multiplying the computed normal modes (eigenvectors of the Hessian matrix expressed in atomic units) by integer multiples of a factor equal to 0.025. The curves on the left are the

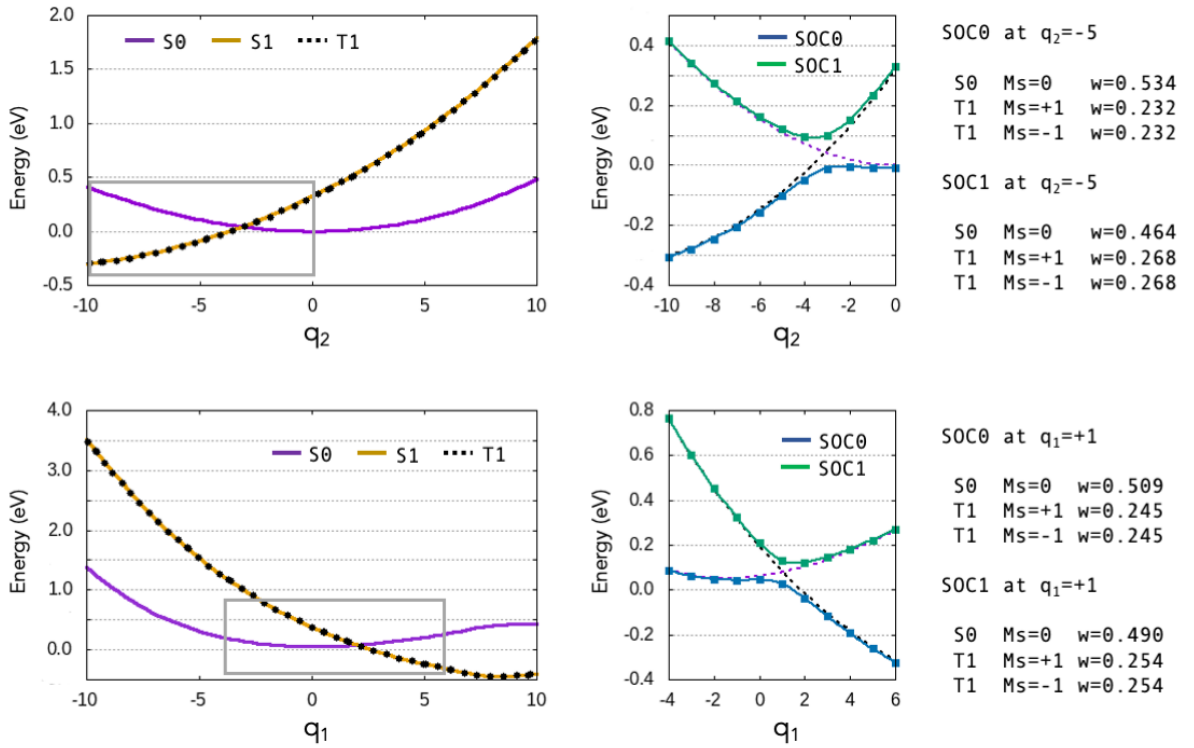

Figure 3.17: Spin-orbit coupling of states in the I_2 + Li_2O_2 reaction. On the right, TDDFT energies along cut of the PESs at fixed value of the q_1 (upper panels) and q_2 (lower panels) coordinates. The curves on the right show the SOC states in the region of singlet-triplet curve crossing, with the relative composition of the SOC states reported on the right side.

TDDFT energies (with relativistic corrections, but without SOCs) of the ground-state (S0) and the first excited state in the singlet (S1) and triplet (T1) spin multiplicities. S1 and T1 represent charge-transfer states where an electron has jumped from an oxygen orbital into a iodine orbital (partial oxidation of Li_2O_2 to LiO_2). In both graphs, T1 and S1 are substantially degenerate in energy and they intersect S0 close to its minimum. The curves on the right are a zoom-in of the crossing region, displaying the electronic states coupled by spin-orbit interactions (SOC0 and SOC1), together with the previous S0 and T1 curves (dotted lines). A strong spin-orbit interaction occurs at the place of curves crossing, with a complete mixing of the two spin-pure states as demonstrated by the reported weights on the right of the graphs. The two avoided-crossings produce an energy splitting in the order of $\sim$ 0.1 eV, which allow the system to evolve from the equilibrium geometry of S0 to the T1 energy well (right to left in the upper panel, left to right in the lower panel) without any relevant energy barrier. The same analysis is repeated in fig. 3.18 for BPC, showing only one scan along the q_2 normal coordinate. The TDDFT energies, on the left panel, closely

resemble those of fig. 3.17. When it comes to the SOC states, however, the comparison with the IPC case shows that the coupling between S0 and T1 is much weaker, and the resulting avoided-crossing produces a much smaller energy splitting between the two curves. The mixing between T1 and S0 is, in fact, less effective: as can be seen by the weights reported in the right of fig. 3.18, the composition of the SOC states, in terms of S0 and T1, abruptly inverts in the span of only one q_2 unitary displacement. Globally, spin-orbit coupling is definitively weaker in BPC than in IPC, as can be expected by the difference in atomic mass ($m_{(I)}$ = 126.9 and $m_{(Br)}$ = 79.9 uma), clearly showing that the heavy-atom effect accounts for most part of the spin transition mechanism in halogen-based RMs.

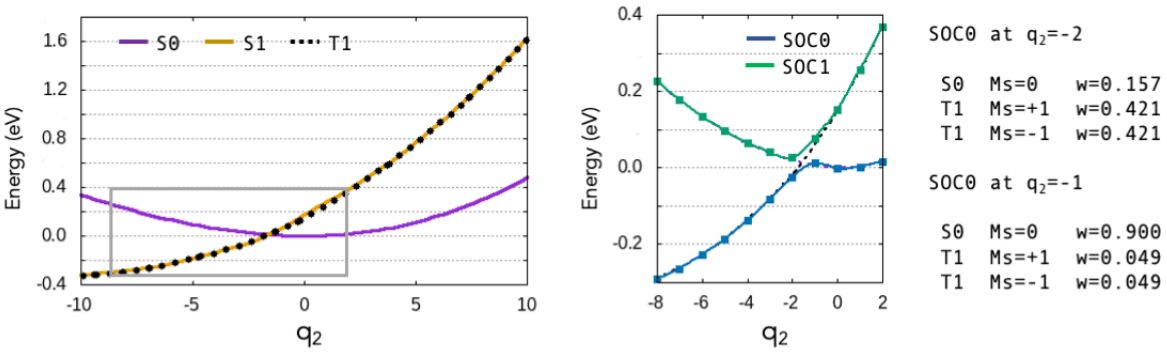

Figure 3.18: Spin-orbit coupling of states in the Br_2 + Li_2O_2 reaction (see the caption of fig. 3.17 for details).

3.2.4 Discussion

The redox semireactions of eqs. 3.11-3.14 can be combined in several ways, to obtain reactive pathways leading from P4 to P3 + O_2, as illustrated in fig. 3.15. Starting from I_2 as the active RM specie, two subsequent single electron-transfer (ET) can take place, leading first to I_2^- and then to I^-. One mechanism, which we will denote as *ET-ET*, generates O_2 by oxidation of the one superoxide in SP3:

$$I_2 + P_4 \longrightarrow LiI_2 + SP_3 \longrightarrow 2\,LiI + P_3 + O_2 \tag{3.18}$$

Another mechanism, however, which will be denoted as *ET-ET-Disp*, can lead to O_2 through disproportionation of the two superoxides present in S2P2:

$$I_2 + P_4 \longrightarrow LiI_2 + SP_3 \longrightarrow 2\,LiI + S_2P_2 \xrightarrow{\text{disp}} 2\,LiI + P_3 + O_2 \tag{3.19}$$

In addition, disproportionation of S2P2 can also occur after a double electron-transfer from P4 to I_2 or to I_3^-, and the resulting mechanisms are denoted as *DET-Disp*:

$$I_2 + P_4 \longrightarrow 2\,LiI + S_2P_2 \xrightarrow{disp} 2\,LiI + P_3 + O_2 \tag{3.20}$$

.

$$LiI_3 + P_4 \longrightarrow 3\,LiI + S_2P_2 \xrightarrow{disp} 3\,LiI + P_3 + O_2 \tag{3.21}$$

Experimentally, disproportionation of pure or mixed lithium superoxide solid phases is known to be spontaneous. On the other hand, the second step in the *ET-ET* mechanism, that is, oxidation of superoxide by LiI_2 (row 10 in table 3.8), is estimated to be ~ 0.3 eV endoergic. So a competition is most likely to be limited between the two mechanism which include disproportionation, i.e. *ET-ET-Disp* and *DET-Disp*. This is in perfect agreement with the estimates of ref.[182]. Accordingly, singlet oxygen release will just depend on superoxide disproportionation, where I-species take no part. As we demonstrated, the reaction between I_2 and lithium peroxide(s) can undergo a spin transition promoted by heavy-atom spin-orbit coupling. So the SP3 intermediate, which is the first intermediate in both *ET-ET* and *ET-ET-Disp* mechanisms, can equally form form as a triplet or a singlet, despite the initial spin state of the reactants being a singlet. The fraction of $^1O_2$ released then should just depend on the energetics of the disproportionation. In sec. 3.1.2 we found that neutral disproportionation of LiO_2 can produce singlet O_2 with < 1 eV of extra energy, which isn't completely unrealistic in presence of high charging voltage.

In the above discussion I_2 was considered only in its reduction reactions to form I_2^- or I^-. It should be reminded that this doesn't contradict the fact that experiments often report a voltage plateau, during recharge, which corresponds to the redox potential of the I_2/I_3^- redox couple. In fact, a distinction must be made between the potential of a redox couple and the specific reactive step where electrons are actually exchanged. For a given redox couple, the redox potential is a quantity related to the ΔG of reaction at equilibrium. The latter depends on the chemical potentials of the species at equilibrium, hence also on their activity (or concentration, to simplify). The I_2/I_3^- redox couple, for instance, can be referred to the sum of coexistent equilibria:

$$I_2 + 2\,e^- \rightleftharpoons 2\,I^-$$

$$I_2 + I^- \rightleftharpoons {I_3}^-$$

as well as to the equilibria:

$$I_2 + e^- \rightleftharpoons {I_2}^-$$

$$I_2^- + I_2^- \rightleftharpoons I_3^- + I^-$$
$$I_2 + I^- \rightleftharpoons I_3^-$$

When the conditions are met for which I_2 reduces at the potential characteristic of the I_2/I_3^- couple, it means that the above equilibria are shifted toward I_3^-, even if this latter doesn't form directly from a transfer of electron(s) to I_2.

The oxidative potential of Br-species is remarkably higher than I-species. As a result, all the oxidation-reduction steps inside the three mechanism presented before (with Br in place of I) are exoergic. In this scenario, the *ET-ET* can also compete with the other two mechanisms, that involve superoxide disproportionation. Singlet oxygen can then form also by oxidation of the superoxide in SP3 by the action of $LiBr_2$. In the previous section, Br was shown to be far less effective in coupling singlet and triplet states owing to its atomic weight. Consequently, the reaction of Br_2 with peroxide is more likely to preserve a singlet spin state in the products, which in turn will lead to the evolution of singlet O_2 according to the *ET-ET* pathway. Given the strong exoergicity of the reactions reported in table 3.9, the system is then expected to have sufficient energy to produce $^1O_2$. Bromine/bromide RMs are therefore expected to have an easier path toward the release of $^1O_2$, something which was not yet not properly investigated by experiments.

Conclusions and final remarks

MOBs are an hot research topic in the field of energy storage. In the near future, increasingly more effort will be put on implementing strategies for the contrast to the problem of parasitic reactivity. This thesis aimed at exploiting computational chemistry methods to model reactive systems of great relevance for aprotic MOBs, trying to contribute to the understanding of the mechanisms which drive the release of singlet oxygen during ORR and OER.

We used the ab-initio methods to study the superoxide disproportionation not only by the thermodynamics of its ground-state species, but also exploring the potential energy surfaces of the chemical processes leading from reactants to products. This approach allowed to investigate the reaction kinetic from a mechanistic viewpoint and to gain insights in the involvement of excited-states in the evolution of the system towards harmful $^1O_2$ release. While proton contaminations where found to favor the most accessible way leading to $^1O_2$ through the proper disproportionation route, an alternative metal-reduction electronic state was found to lie close the peroxide configuration, which can lower the reaction energies for the larger, weaker Lewis-acid alkali cations (Na and K). Not only this provides a deeper insight into the complex mechanism of oxygen discharge during ORR, but it also provide an additional route for the onset of degradation reactions, which was not foreseen in the previous literature. In the study on redox mediators we focused on the identification of reactive pathways consistent with the release of $^1O_2$. Our conclusion is that iodine-based RMs do not directly produce $^1O_2$, whose presence, in agreement with experimental literature, should be ascribed to the disproportionation reaction occurring in partially oxidized superoxide/peroxide mixed phases. For Br_2, instead, a possible pathway to the direct production of $^1O_2$ from Li_2O_2 is identified, which is also connected with the lower extent of singlet and triplet states coupling due to spin-orbit.

A current limitation in the approach adopted is surely represented by the limited size of the systems that can be included in CAS-based calculations. Hence, a future development should go in the direction of including a larger part of the cell environment into the computational model, starting from a description of solvent effects based not only on the bulk

dielectric constant, up to the inclusion of interfacial effects involving the surface of the discharged peroxide products and/or the electrode. On the other hand, a direct experimental support is mandatory to validate the mechanisms proposed in chapter 3. For this purpose, collaborations are ongoing with the group of prof. Sergio Brutti at *Sapienza* University of Rome and the EPR laboratory of the I.S.S. (*Istituto Superiore di Sanità*). The main aim of this collaboration is the characterization, through combined spectroscopic techniques, of intermediate species to elucidate the mechanism of $^1O_2$ release during Li_2O_2 oxidation with redox mediators.

Acknowledgements

My most sincere thanks go to my supervisor Prof. Enrico Bodo. My work under his guidance has started more than four years ago, while working on my Master's thesis. During all this time, not only his profound knowledge supported me across the many obstacles I had to face. Also, his original approach to scientific problems and his personal view on the world of research undoubtedly made the most of my development as a scientist and a researcher.
I gratefully thank Prof. Sergio Brutti for his invaluable collaboration, which materialized during all these years in both publications and precious advises. As a theoretical chemist lent to battery research, I could benefit in many occasions from his knowledge and experience in the field of electrochemistry for adjusting the direction of my research project.
I am pleased to express my deep gratitude to Prof. Patrik Johansson, who hosted me for half a year in his research group at Chalmers University of Technology. During those months I could challenge myself to explore techniques and systems which were out of my experience, while working in an extremely stimulating environment and directly learning from one of the best in the field.
My sincere and heartfelt thanks go also to the many colleagues and students who shared with me part of this journey. In particular: Dr. Mohammed Salha, Dr. Stefano Russo and Dr. Vanessa Piacentini, who have been part of my group in these last years, sharing everyday problems and mutually supporting each other, and also PhD Andrea Le Donne, PhD Josephine Alba, Dr. Nicole Mancini and PhD Henry Adenousi, who were with me as both friends and points of reference when I moved my first steps in the world of scientific research. To all of them, I wish the best of luck.
Sapienza University of Rome has somehow been my house for many years. I am grateful to the Institution and to my Department, for the opportunity I had to realize so far my projects and do the job that I love.

List of publications

The following articles containing the original research work of this thesis have been published:

- A. Pierini, S. Brutti and E. Bodo, Superoxide anion disproportionation induced by Li^+ and H^+: pathways to $^1O_2$ release in Li-O_2 batteries, *ChemPhysChem* 2020, 21, 2027.
- A. Pierini, S. Brutti and E. Bodo, Reactive pathways toward parasitic release of singlet oxygen in metal-air batteries, *npj Comput. Mater.* 2021, 7, 126.
- A. Pierini, S. Brutti and E. Bodo, Study of the electronic structure of alkali peroxides and their role in the chemistry of metal–oxygen batteries, *J. Phys. Chem. A* 2021, 125, 42, 9368–9376.
- A. Pierini, S. Brutti and E. Bodo, Reactions in non-aqueous alkali and alkaline-earth metal–oxygen batteries: a thermodynamic study, *Phys. Chem. Chem. Phys.* 2021, 23, 24487-24496.

The following articles containing the original research work of this thesis are under preparation:

- A. Pierini, A. Petrongari, V. Piacentini, E. Bodo and S. Brutti, Mechanistic insights into halogen/halide redox mediators for Li-O_2 batteries, *in preparation*.

The following review over the topic of metal-oxygen batteries, also discussing part of the work contained in the published papers, is under preparation:

- A. Pierini, A. Petrongari, V. Piacentini, E. Bodo and S. Brutti, Singlet oxygen in aprotic metal-O_2 batteries, *in preparation*.

Bibliography

[1] P. G. Bruce, S. A. Freunberger, L. J. Hardwick, and J.-M. Tarascon. Li–o2 and li–s batteries with high energy storage. *Nat. Mater.*, 11(1):19–29, 2012.

[2] K. M. Abraham and Z. Jiang. A polymer electrolyte-based rechargeable lithium/oxygen battery. *J. Electrochem. Soc.*, 143(1):1, 1996.

[3] R. D. Rauh, K. M. Abraham, G. F. Pearson, J. K. Surprenant, and S. B. Brummer. A lithium/dissolved sulfur battery with an organic electrolyte. *J. Electrochem. Soc.*, 126(4):523, 1979.

[4] E. Peled, Y. Sternberg, A. Gorenshtein, and Y. Lavi. Lithium-sulfur battery: evaluation of dioxolane-based electrolytes. *J. Electrochem. Soc.*, 136(6):1621, 1989.

[5] P. N. Ross. A novel zinc-air battery for electric vehicles. In *Proceedings of the Tenth Annual Battery Conference on Applications and Advances*, pages 131–133. IEEE, 1995.

[6] J. Read. Characterization of the lithium/oxygen organic electrolyte battery. *J. Electrochem. Soc.*, 149(9):A1190, 2002.

[7] J. Read. Ether-based electrolytes for the lithium/oxygen organic electrolyte battery. *J. Electrochem. Soc.*, 153(1):A96, 2005.

[8] T. Kuboki, T. Okuyama, T. Ohsaki, and N. Takami. Lithium-air batteries using hydrophobic room temperature ionic liquid electrolyte. *J. Power Sources*, 146(1-2):766–769, 2005.

[9] T. Ogasawara, A. Débart, M. Holzapfel, P. Novák, and P. G. Bruce. Rechargeable li2o2 electrode for lithium batteries. *J. Am. Chem. Soc.*, 128(4):1390–1393, 2006.

[10] G. Girishkumar, B. McCloskey, A. C. Luntz, S. Swanson, and W. Wilcke. Lithium-air battery: promise and challenges. *J. Phys. Chem. Lett.*, 1(14):2193–2203, 2010.

[11] P. Hartmann, C. L. Bender, M. Vračar, A. K. Dürr, A. Garsuch, J. Janek, and P. Adelhelm. A rechargeable room-temperature sodium superoxide (nao2) battery. *Nat. Mater.*, 12:228–232, 2013.

[12] S. K. Das, S. Lau, and L. A. Archer. Sodium–oxygen batteries: a new class of metal–air batteries. *J. Mater. Chem. A*, 2(32):12623–12629, 2014.

[13] X. Ren and Y. Wu. A low-overpotential potassium–oxygen battery based on potassium superoxide. *J. Am. Chem. Soc.*, 135(8):2923–2926, 2013.

[14] T. Shiga, Y. Hase, Y. Kato, M. Inoue, and K. Takechi. A rechargeable non-aqueous mg–o 2 battery. *Chem. Commun.*, 49(80):9152–9154, 2013.

[15] T. Zhang, Z. Tao, and J. Chen. Magnesium–air batteries: from principle to application. *Mater. Horiz.*, 1(2):196–206, 2014.

[16] P. Reinsberg, C. J. Bondue, and H. Baltruschat. Calcium–oxygen batteries as a promising alternative to sodium–oxygen batteries. *J. Phys. Chem. C*, 120(39):22179–22185, 2016.

[17] J. P. Zheng, R. Y. Liang, M. Hendrickson, and E. J. Plichta. Theoretical energy density of li–air batteries. *J. Electrochem. Soc.*, 155(6):A432, 2008.

[18] W. Cao, J. Zhang, and H. Li. Batteries with high theoretical energy densities. *Energy Storage Mater.*, 26:46–55, 2020.

[19] Y. Wu, L. Xie, H. Ming, Y. Guo, J.-Y. Hwang, W. Wang, X. He, L. Wang, H. N. Alshareef, Y.-K. Sun, et al. An empirical model for the design of batteries with high energy density. *ACS Energy Lett.*, 5(3):807–816, 2020.

[20] J. Deng, C. Bae, A. Denlinger, and T. Miller. Electric vehicles batteries: requirements and challenges. *Joule*, 4(3):511–515, 2020.

[21] A. Suryatna, I. Raya, L. Thangavelu, F. R. Alhachami, M. M. Kadhim, U. S. Altimari, Z. H. Mahmoud, Y. F. Mustafa, and E. Kianfar. A review of high-energy density lithium-air battery technology: Investigating the effect of oxides and nanocatalysts. *J. Chem.*, 2022, 2022.

[22] I. Landa-Medrano, C. Li, N. Ortiz-Vitoriano, I. Ruiz de Larramendi, J. Carrasco, and T. Rojo. Sodium–oxygen battery: steps toward reality. *J. Phys. Chem. Lett.*, 7(7):1161–1166, 2016.

[23] Y.-T. Lu, A. R. Neale, C.-C. Hu, and L. J. Hardwick. Divalent nonaqueous metal-air batteries. *Frontiers in Energy Research*, 8:602918, 2021.

[24] S. Xu, S. Lau, and L. A. Archer. Co 2 and ambient air in metal–oxygen batteries: steps towards reality. *Inorg. Chem. Front.*, 2(12):1070–1079, 2015.

[25] P. Zhang, M. Ding, X. Li, C. Li, Z. Li, and L. Yin. Challenges and strategy on parasitic reaction for high-performance nonaqueous lithium–oxygen batteries. *Adv. Energy Mater.*, 10(40):2001789, 2020.

[26] C. Laoire, S. Mukerjee, K. M. Abraham, E. J. Plichta, and M. A. Hendrickson. Elucidating the mechanism of oxygen reduction for lithium-air battery applications. *J. Phys. Chem. C*, 113(46):20127–20134, 2009.

[27] Z. Peng, S. A. Freunberger, L. J. Hardwick, Y. Chen, V. Giordani, F. Bardé, P. Novák, D. Graham, J.-M. Tarascon, and P. G. Bruce. Oxygen reactions in a non-aqueous li+ electrolyte. *Angew. Chem. Int. Ed.*, 50(28):6351–6355, 2011.

[28] Q. Yu and S. Ye. In situ study of oxygen reduction in dimethyl sulfoxide (dmso) solution: a fundamental study for development of the lithium–oxygen battery. *J. Phys. Chem. C*, 119(22):12236–12250, 2015.

[29] R. Cao, E. D. Walter, W. Xu, E. N. Nasybulin, P. Bhattacharya, M. E. Bowden, M. H. Engelhard, and J.-G. Zhang. The mechanisms of oxygen reduction and evolution reactions in nonaqueous lithium–oxygen batteries. *ChemSusChem*, 7(9):2436–2440, 2014.

[30] S. A. Freunberger, Y. Chen, Z. Peng, J. M. Griffin, L. J. Hardwick, F. Bardé, P. Novák, and P. G. Bruce. Reactions in the rechargeable lithium–o2 battery with alkyl carbonate electrolytes. *J. Am. Chem. Soc.*, 133(20):8040–8047, 2011.

[31] C. J. Barile and A. A. Gewirth. Investigating the li-o2 battery in an ether-based electrolyte using differential electrochemical mass spectrometry. *J. Electrochem. Soc.*, 160(4):A549, 2013.

[32] D. G. Kwabi, T. P. Batcho, C. V. Amanchukwu, N. Ortiz-Vitoriano, P. Hammond, C. V. Thompson, and Y. Shao-Horn. Chemical instability of dimethyl sulfoxide in lithium–air batteries. *J. Phys. Chem. Lett.*, 5(16):2850–2856, 2014.

[33] T. K. Zakharchenko, A. I. Belova, A. S. Frolov, O. O. Kapitanova, J.-J. Velasco-Velez, A. Knop-Gericke, D. Vyalikh, D. M. Itkis, and L. V. Yashina. Notable reactivity of acetonitrile towards li2o2/lio2 probed by nap xps during li–o2 battery discharge. *Top. Catal.*, 61(20):2114–2122, 2018.

[34] E. Knipping, C. Aucher, G. Guirado, and L. J. Aubouy. Room temperature ionic liquids versus organic solvents as lithium–oxygen battery electrolytes. *New J. Chem.*, 42(6):4693–4699, 2018.

[35] C. L. Bender, B. Jache, P. Adelhelm, and J. Janek. Sodiated carbon: a reversible anode for sodium–oxygen batteries and route for the chemical synthesis of sodium superoxide (nao 2). *J. Mater. Chem. A*, 3(41):20633–20641, 2015.

[36] W. D. McCulloch, X. Ren, M. Yu, Z. Huang, and Y. Wu. Potassium-ion oxygen battery based on a high capacity antimony anode. *ACS. Appl. Mater. Interfaces*, 7(47):26158–26166, 2015.

[37] M. M. Ottakam Thotiyl, S. A. Freunberger, Z. Peng, Y. Chen, Z. Liu, and P. G. Bruce. A stable cathode for the aprotic li–o2 battery. *Nat. Mater.*, 12(11):1050–1056, 2013.

[38] D. Kundu, R. Black, B. Adams, K. Harrison, K. Zavadil, and L. F. Nazar. Nanostructured metal carbides for aprotic li–o2 batteries: new insights into interfacial reactions and cathode stability. *J. Phys. Chem. Lett.*, 6(12):2252–2258, 2015.

[39] E. Mourad, Y. K. Petit, R. Spezia, A. Samojlov, F. F. Summa, C. Prehal, C. Leypold, N. Mahne, C. Slugovc, O. Fontaine, et al. Singlet oxygen from cation driven superoxide disproportionation and consequences for aprotic metal–o 2 batteries. *Energy Environ. Sci.*, 12(8):2559–2568, 2019.

[40] M. Hayyan, M. A. Hashim, and I. M. AlNashef. Superoxide ion: generation and chemical implications. *Chem. Rev.*, 116(5):3029–3085, 2016.

[41] J. Lu, Y. Jung Lee, X. Luo, K. C. Lau, M. Asadi, H.-H. Wang, S. Brombosz, J. Wen, D. Zhai, Z. Chen, et al. A lithium–oxygen battery based on lithium superoxide. *Nature*, 529(7586):377–382, 2016.

[42] C. L. Bender, P. Hartmann, M. Vračar, P. Adelhelm, and J. Janek. On the thermodynamics, the role of the carbon cathode, and the cycle life of the sodium superoxide (nao2) battery. *Adv. Energy Mater.*, 4(12):1301863, 2014.

[43] C. L. Bender, D. Schröder, R. Pinedo, P. Adelhelm, and J. Janek. One-or two-electron transfer? the ambiguous nature of the discharge products in sodium–oxygen batteries. *Angew. Chem. Int. Ed.*, 55(15):4640–4649, 2016.

[44] W.-W. Yin, J.-L. Yue, M.-H. Cao, W. Liu, J.-J. Ding, F. Ding, L. Sang, and Z.-W. Fu. Dual catalytic behavior of a soluble ferrocene as an electrocatalyst and in the electrochemistry for na–air batteries. *J. Mater. Chem. A*, 3(37):19027–19032, 2015.

[45] Q. Sun, H. Yadegari, M. N. Banis, J. Liu, B. Xiao, B. Wang, S. Lawes, X. Li, R. Li, and X. Sun. Self-stacked nitrogen-doped carbon nanotubes as long-life air electrode for sodium-air batteries: Elucidating the evolution of discharge product morphology. *Nano Energy*, 12:698–708, 2015.

[46] I. Landa-Medrano, A. Sorrentino, L. Stievano, I. de Larramendi, E. Pereiro, L. Lezama, T. Rojo, and D. Tonti. Architecture of na-o2 battery deposits revealed by transmission x-ray microscopy. *Nano Energy*, 37:224–231, 2017.

[47] Z. P. Jovanov, L. Lutz, J. Lozano, C. Holc, X. Gao, A. Grimaud, J.-M. Tarascon, Y. Chen, L. R. Johnson, and P. G. Bruce. Competitive oxygen reduction pathways to superoxide and peroxide during sodium-oxygen battery discharge. *Batteries & Supercaps*, 2022.

[48] S. Kang, Y. Mo, S. P. Ong, and G. Ceder. Nanoscale stabilization of sodium oxides: implications for na–o2 batteries. *Nano Lett.*, 14(2):1016–1020, 2014.

[49] W. Wang, N.-C. Lai, Z. Liang, Y. Wang, and Y.-C. Lu. Superoxide stabilization and a universal ko2 growth mechanism in potassium–oxygen batteries. *Angew. Chem.*, 130(18):5136–5140, 2018.

[50] W. D. McCulloch, N. Xiao, G. Gourdin, and Y. Wu. Alkali-oxygen batteries based on reversible superoxide chemistry. *Chem. Eur. J.*, 24(67):17627–17637, 2018.

[51] Y. Chen, Z. P. Jovanov, X. Gao, J. Liu, C. Holc, L. R. Johnson, and P. G. Bruce. High capacity surface route discharge at the potassium-o2 electrode. *J. Electroanal. Chem.*, 819:542–546, 2018.

[52] S. Sankarasubramanian and V. Ramani. Dimethyl sulfoxide-based electrolytes for high-current potassium–oxygen batteries. *J. Phys. Chem. C*, 122(34):19319–19327, 2018.

[53] P. H. Reinsberg, A. Koellisch, P. P. Bawol, and H. Baltruschat. K–o 2 electrochemistry: achieving highly reversible peroxide formation. *Phys. Chem. Chem. Phys.*, 21(8):4286–4294, 2019.

[54] J. S. Hummelshøj, J. Blomqvist, S. Datta, T. Vegge, J. Rossmeisl, K. S. Thygesen, A. C. Luntz, K. W. Jacobsen, and J. K. Nørskov. Communications: Elementary oxygen electrode reactions in the aprotic li-air battery. *J. Chem. Phys.*, 132(7):071101, 2010.

[55] J. M. Garcia-Lastra, J. D. Bass, and K. S. Thygesen. Communication: Strong excitonic and vibronic effects determine the optical properties of li2o2. *J. Chem. Phys.*, 135(12):121101, 2011.

[56] O. Gerbig, R. Merkle, and J. Maier. Electron and ion transport in li2o2. *Adv. Mater.*, 25(22):3129–3133, 2013.

[57] R. B. Araujo, S. Chakraborty, and R. Ahuja. Unveiling the charge migration mechanism in na 2 o 2: implications for sodium–air batteries. *Phys. Chem. Chem. Phys.*, 17(12):8203–8209, 2015.

[58] S. Yang and D. J. Siegel. Intrinsic conductivity in sodium–air battery discharge phases: sodium superoxide vs sodium peroxide. *Chem. Mater.*, 27(11):3852–3860, 2015.

[59] B. Lee, J. Kim, G. Yoon, H.-D. Lim, I.-S. Choi, and K. Kang. Theoretical evidence for low charging overpotentials of superoxide discharge products in metal–oxygen batteries. *Chem. Mater.*, 27(24):8406–8413, 2015.

[60] S. Li, J. Liu, and B. Liu. First-principles study of the charge transport mechanisms in lithium superoxide. *Chem. Mater.*, 29(5):2202–2210, 2017.

[61] O. Arcelus, C. Li, T. Rojo, and J. Carrasco. Electronic structure of sodium superoxide bulk,(100) surface, and clusters using hybrid density functional: Relevance for na–o2 batteries. *J. Phys. Chem. Lett.*, 6(11):2027–2031, 2015.

[62] Y. Zhang, X. Zhang, J. Wang, W. C. McKee, Y. Xu, and Z. Peng. Potential-dependent generation of o2–and lio2 and their critical roles in o2 reduction to li2o2 in aprotic li–o2 batteries. *J. Phys. Chem. C*, 120(7):3690–3698, 2016.

[63] C. Prehal, S. Mondal, L. Lovicar, and S. A. Freunberger. Exclusive solution discharge in li–o2 batteries? *ACS Energy Lett.*, 7(9):3112–3119, 2022.

[64] C. Sheng, F. Yu, Y. Wu, Z. Peng, and Y. Chen. Disproportionation of sodium superoxide in metal–air batteries. *Angew. Chem.*, 130(31):10054–10058, 2018.

[65] D. Sharon, D. Hirsberg, M. Salama, M. Afri, A. Frimer, M. Noked, W. Kwak, Y.-K. Sun, and D. Aurbach. Mechanistic role of li+ dissociation level in aprotic li–o2 battery. *ACS. Appl. Mater. Interfaces*, 8(8):5300–5307, 2016.

[66] H. Yadegari and X. Sun. Sodium–oxygen batteries: recent developments and remaining challenges. *Trends Chem.*, 2(3):241–253, 2020.

[67] M. Leskes, A. J. Moore, G. R. Goward, and C. P. Grey. Monitoring the electrochemical processes in the lithium–air battery by solid state nmr spectroscopy. *J. Phys. Chem. C*, 117(51):26929–26939, 2013.

[68] C. Tan, A. Wang, D. Cao, F. Yu, Y. Wu, X. He, and Y. Chen. Unravelling the complex na2co3 electrochemical process in rechargeable na-co2 batteries. *Advanced Energy Materials*, page 2204191, 2023.

[69] T. Zhang, N. Imanishi, Y. Takeda, and O. Yamamoto. Aqueous lithium/air rechargeable batteries. *Chem. Lett.*, 40(7):668–673, 2011.

[70] N. Imanishi and O. Yamamoto. Rechargeable lithium–air batteries: characteristics and prospects. *Mater. Today*, 17(1):24–30, 2014.

[71] J. Lu, L. Li, J.-B. Park, Y.-K. Sun, F. Wu, and K. Amine. Aprotic and aqueous li–o2 batteries. *Chem. Rev.*, 114(11):5611–5640, 2014.

[72] C. Xia, R. Black, R. Fernandes, B. Adams, and L. F. Nazar. The critical role of phase-transfer catalysis in aprotic sodium oxygen batteries. *Nat. Chem.*, 7(6):496–501, 2015.

[73] C. Y. Xia, C. Y. Kwok, and L. F. Nazar. A high-energy-density lithium-oxygen battery based on a reversible four-electron conversion to lithium oxide. *Science*, 361(6404):777–781, 2018.

[74] Q. Qiu, Z.-Z. Pan, P. Yao, J. Yuan, C. Xia, Y. Zhao, and Y. Li. A 98.2% energy efficiency li-o2 battery using a lani-0.5 co0. 5o3 perovskite cathode with extremely fast oxygen reduction and evolution kinetics. *Chem. Eng. J.*, page 139608, 2022.

[75] D. T. Sawyer and J. S. Valentine. How super is superoxide? *Acc. Chem. Res.*, 14(12):393–400, 1981.

[76] B. H. Bielski and A. O. Allen. Mechanism of the disproportionation of superoxide radicals. *J. Phys. Chem.*, 81(11):1048–1050, 1977.

[77] W. H. Koppenol and J. Butler. Mechanism of reactions involving singlet oxygen and the superoxide anion. *FEBS Lett.*, 83(1):1–6, 1977.

[78] C. P. Andrieux, P. Hapiot, and J. M. Saveant. Mechanism of superoxide ion disproportionation in aprotic solvents. *J. Am. Chem. Soc.*, 109(12):3768–3775, 1987.

[79] D. H. Chin, G. Chiericato Jr, E. J. Nanni Jr, and D. T. Sawyer. Proton-induced disproportionation of superoxide ion in aprotic media. *J. Am. Chem. Soc.*, 104(5):1296–1299, 1982.

[80] J. S. Valentine, A. R. Miksztal, and D. T. Sawyer. [7] methods for the study of superoxide chemistry in nonaqueous solutions. *Methods Enzymol.*, 105:71–81, 1984.

[81] D. Córdoba, H. B. Rodríguez, and E. J. Calvo. Singlet oxygen formation during the oxygen reduction reaction in dmso litfsi on lithium air battery carbon electrodes. *ChemistrySelect*, 4(42):12304–12307, 2019.

[82] G. F. Carter and D. H. Templeton. Polymorphism of sodium superoxide. *J. Am. Chem. Soc.*, 75(21):5247–5249, 1953.

[83] V. Bakulina, S. Tokareva, and I. Vol'Nov. X-ray analysis of lithium superperoxide lio2. *J. Struct. Chem.*, 8:980–981, 1967.

[84] J. Sangster and A. D. Pelton. The li-o (lithium-oxygen) system. *J. Phase Equilib.*, 13:296–299, 1992.

[85] I. Landa-Medrano, R. Pinedo, X. Bi, I. Ruiz de Larramendi, L. Lezama, J. Janek, K. Amine, J. Lu, and T. Rojo. New insights into the instability of discharge products in na–o2 batteries. *ACS. Appl. Mater. Interfaces*, 8(31):20120–20127, 2016.

[86] V. S. Dilimon, C. Hwang, Y.-G. Cho, J. Yang, H.-D. Lim, K. Kang, S. J. Kang, and H.-K. Song. Superoxide stability for reversible na-o2 electrochemistry. *Sci. Rep.*, 7(1):1–10, 2017.

[87] L. He, J. Huang, and Y. Chen. First-order or second-order? disproportionation of lithium superoxide in li–o2 batteries. *J. Phys. Chem. Lett.*, 13(8):2033–2038, 2022.

[88] Y. Orikasa, T. Masese, Y. Koyama, T. Mori, M. Hattori, K. Yamamoto, T. Okado, Z.-D. Huang, T. Minato, C. Tassel, et al. High energy density rechargeable magnesium battery using earth-abundant and non-toxic elements. *Sci. Rep.*, 4(1):1–6, 2014.

[89] M. E. Arroyo de Dompablo, A. Ponrouch, P. Johansson, and M. R. Palacín. Achievements, challenges, and prospects of calcium batteries. *Chem. Rev.*, 120(14):6331–6357, 2019.

[90] A. Ponrouch, J. Bitenc, R. Dominko, N. Lindahl, P. Johansson, and M. R. Palacín. Multivalent rechargeable batteries. *Energy Storage Mater.*, 20:253–262, 2019.

[91] G. Vardar, E. G. Nelson, J. G. Smith, J. Naruse, H. Hiramatsu, B. M. Bartlett, A. Sleightholme, D. J. Siegel, and C. W. Monroe. Identifying the discharge product and reaction pathway for a secondary mg/o2 battery. *Chem. Mater.*, 27(22):7564–7568, 2015.

[92] J. G. Smith, J. Naruse, H. Hiramatsu, and D. J. Siegel. Theoretical limiting potentials in mg/o2 batteries. *Chem. Mater.*, 28(5):1390–1401, 2016.

[93] T. Shiga, Y. Kato, and Y. Hase. Coupling of nitroxyl radical as an electrochemical charging catalyst and ionic liquid for calcium plating/stripping toward a rechargeable calcium–oxygen battery. *J. Mater. Chem. A*, 5(25):13212–13219, 2017.

[94] P. P. Bawol, P. H. Reinsberg, A. Koellisch-Mirbach, C. J. Bondue, and H. Baltruschat. The oxygen reduction reaction in ca2+-containing dmso: Reaction mechanism, electrode surface characterization, and redox mediation. *ChemSusChem*, 14(1):428–440, 2021.

[95] A. Koellisch-Mirbach, P. P. Bawol, I. Park, and H. Baltruschat. Towards a generalized orr mechanism in m2+-containing dmso: Oxygen reduction and evolution in ca2+-containing dmso on atomically smooth and rough pt. *ChemElectroChem*, 9(9):e202200159, 2022.

[96] N. Mahne, O. Fontaine, M. Ottakam Thotiyl, M. Wilkening, and S. A. Freunberger. Mechanism and performance of lithium–oxygen batteries–a perspective. *Chem. Sci.*, 8(10):6716–6729, 2017.

[97] A. C. Luntz and B. D. McCloskey. Li–air batteries: Importance of singlet oxygen. *Nat. Energy*, 2(5):1–2, 2017.

[98] B. D. McCloskey, A. Valery, A. C. Luntz, S. R. Gowda, G. M. Wallraff, J. M. Garcia, T. Mori, and L. E. Krupp. Combining accurate o2 and li2o2 assays to separate discharge and charge stability limitations in nonaqueous li–o2 batteries. *J. Phys. Chem. Lett.*, 4(17):2989–2993, 2013.

[99] B. D. McCloskey, D. S. Bethune, R. M. Shelby, T. Mori, R. Scheffler, A. Speidel, M. Sherwood, and A. C. Luntz. Limitations in rechargeability of li-o2 batteries and possible origins. *J. Phys. Chem. Lett.*, 3(20):3043–3047, 2012.

[100] M. Balaish, A. Kraytsberg, and Y. Ein-Eli. A critical review on lithium–air battery electrolytes. *Phys. Chem. Chem. Phys.*, 16(7):2801–2822, 2014.

[101] B. D. McCloskey, D. S. Bethune, R. M. Shelby, G. Girishkumar, and A. C. Luntz. Solvents' critical role in nonaqueous lithium–oxygen battery electrochemistry. *J. Phys. Chem. Lett.*, 2(10):1161–1166, 2011.

[102] S. A. Freunberger, Y. Chen, N. E. Drewett, L. J. Hardwick, F. Bardé, and P. G. Bruce. The lithium–oxygen battery with ether-based electrolytes. *Angew. Chem. Int. Ed.*, 50(37):8609–8613, 2011.

[103] D. Sharon, M. Afri, M. Noked, A. Garsuch, A. A. Frimer, and D. Aurbach. Oxidation of dimethyl sulfoxide solutions by electrochemical reduction of oxygen. *J. Phys. Chem. Lett.*, 4(18):3115–3119, 2013.

[104] M. Carboni, A. G. Marrani, R. Spezia, and S. Brutti. Degradation of litfo/tegme and litfo/dme electrolytes in li-o2 batteries. *J. Electrochem. Soc.*, 165(2):A118, 2018.

[105] M. Olivares-Marin, A. Sorrentino, E. Pereiro, and D. Tonti. Discharge products of ionic liquid-based li-o2 batteries observed by energy dependent soft x-ray transmission microscopy. *J. Power Sources*, 359:234–241, 2017.

[106] S. Y. Sayed, K. Yao, D. G. Kwabi, T. P. Batcho, C. V. Amanchukwu, S. Feng, C. V. Thompson, and Y. Shao-Horn. Revealing instability and irreversibility in nonaqueous sodium–o 2 battery chemistry. *Chem. Commun.*, 52(62):9691–9694, 2016.

[107] L. Lutz, D. Alves Dalla Corte, M. Tang, E. Salager, M. Deschamps, A. Grimaud, L. Johnson, P. G. Bruce, and J.-M. Tarascon. Role of electrolyte anions in the na–o2 battery: implications for nao2 solvation and the stability of the sodium solid electrolyte interphase in glyme ethers. *Chem. Mater.*, 29(14):6066–6075, 2017.

[108] G. Cong, W. Wang, N.-C. Lai, Z. Liang, and Y.-C. Lu. A high-rate and long-life organic–oxygen battery. *Nat. Mater.*, 18(4):390–396, 2019.

[109] W. Wang and Y.-C. Lu. Achieving a stable nonaqueous air cathode under true ambient air. *ACS Energy Lett.*, 5(12):3804–3812, 2020.

[110] W. Zhang, Y. Huang, Y. Liu, L. Wang, S. Chou, and H. Liu. Strategies toward stable nonaqueous alkali metal–o2 batteries. *Adv. Energy Mater.*, 9(24):1900464, 2019.

[111] V. S. Bryantsev, V. Giordani, W. Walker, M. Blanco, S. Zecevic, K. Sasaki, J. Uddin, D. Addison, and G. V. Chase. Predicting solvent stability in aprotic electrolyte li–air batteries: nucleophilic substitution by the superoxide anion radical (o2•–). *J. Phys. Chem. A*, 115(44):12399–12409, 2011.

[112] N. Kumar, M. D. Radin, B. C. Wood, T. Ogitsu, and D. J. Siegel. Surface-mediated solvent decomposition in li–air batteries: impact of peroxide and superoxide surface terminations. *J. Phys. Chem. C*, 119(17):9050–9060, 2015.

[113] V. Chau, Z. Chen, H. Hu, and K.-J. Chan. Exploring solvent stability against nucleophilic attack by solvated lio2- in an aprotic li-o2 battery. *J. Electrochem. Soc.*, 164(2):A284, 2016.

[114] J. Kim, H. Park, B. Lee, W. M. Seong, H.-D. Lim, Y. Bae, H. Kim, W. K. Kim, K. H. Ryu, and K. Kang. Dissolution and ionization of sodium superoxide in sodium–oxygen batteries. *Nat. Commun.*, 7(1):1–9, 2016.

[115] M. M. Ottakam Thotiyl, S. A. Freunberger, Z. Peng, and P. G. Bruce. The carbon electrode in nonaqueous li–o2 cells. *J. Am. Chem. Soc.*, 135(1):494–500, 2013.

[116] D. G. Kwabi, N. Ortiz-Vitoriano, S. A. Freunberger, Y. Chen, N. Imanishi, P. G. Bruce, and Y. Shao-Horn. Materials challenges in rechargeable lithium-air batteries. *MRS bulletin*, 39(5):443–452, 2014.

[117] J. Wandt, P. Jakes, J. Granwehr, H. A. Gasteiger, and R. A. Eichel. Singlet oxygen formation during the charging process of an aprotic lithium–oxygen battery. *Angew. Chem.*, 128(24):7006–7009, 2016.

[118] N. Mahne, B. Schafzahl, C. Leypold, M. Leypold, S. Grumm, A. Leitgeb, G. A. Strohmeier, M. Wilkening, O. Fontaine, D. Kramer, et al. Singlet oxygen generation as a major cause for parasitic reactions during cycling of aprotic lithium–oxygen batteries. *Nat. Energy*, 2(5):1–9, 2017.

[119] N. Mahne, S. E. Renfrew, B. D. McCloskey, and S. A. Freunberger. Electrochemical oxidation of lithium carbonate generates singlet oxygen. *Angew. Chem. Int. Ed.*, 57(19):5529–5533, 2018.

[120] L. Schafzahl, N. Mahne, B. Schafzahl, M. Wilkening, C. Slugovc, S. M. Borisov, and S. A. Freunberger. Singlet oxygen during cycling of the aprotic sodium–o2 battery. *Angew. Chem. Int. Ed.*, 56(49):15728–15732, 2017.

[121] L. Qin, L. Schkeryantz nd J. Zheng, N. Xiao, and Y. Wu. Superoxide-based k–o2 batteries: Highly reversible oxygen redox solves challenges in air electrodes. *J. Am. Chem. Soc.*, 142(27):11629–11640, 2020.

[122] Z. Qu. Reactivities of singlet oxygen: open-shell or closed-shell? *Phys. Chem. Chem. Phys.*, 22(24):13373–13377, 2020.

[123] C. Schweitzer and R. Schmidt. Physical mechanisms of generation and deactivation of singlet oxygen. *Chem. Rev.*, 103(5):1685–1758, 2003.

[124] I. Ruiz de Larramendi and N. Ortiz-Vitoriano. Unraveling the effect of singlet oxygen on metal-o2 batteries: Strategies toward deactivation. *Front. Chem.*, 8:605, 2020.

[125] A. Schürmann, B. Luerßen, D. Mollenhauer, J. Janek, and D. Schröder. Singlet oxygen in electrochemical cells: A critical review of literature and theory. *Chem. Rev.*, 121(20):12445–12464, 2021.

[126] B. J. Moss, F. W. Bobrowicz, and W. A. Goddard III. The generalized valence bond description of o2. *J. Chem. Phys.*, 63(11):4632–4639, 1975.

[127] M. J. Paterson, O. Christiansen, F. Jensen, and P. R. Ogilby. Overview of theoretical and computational methods applied to the oxygen-organic molecule photosystem. *Photochem. Photobiol*, 82(5):1136–1160, 2006.

[128] M. Garavelli, F. Bernardi, M. Olivucci, and M. A. Robb. Dft study of the reactions between singlet-oxygen and a carotenoid model. *J. Am. Chem. Soc.*, 120(39):10210–10222, 1998.

[129] Y. Kitagawa, T. Saito, Y. Nakanishi, Y. Kataoka, T. Matsui, T. Kawakami, M. Okumura, and K. Yamaguchi. Spin contamination error in optimized geometry of singlet carbene (1a1) by broken-symmetry method. *J. Phys. Chem. A*, 113(52):15041–15046, 2009.

[130] J. W. Mullinax, C. W. Bauschlicher Jr, and J. W. Lawson. Reaction of singlet oxygen with the ethylene group: implications for electrolyte stability in li-ion and li-o2 batteries. *J. Phys. Chem. A*, 125(14):2876–2884, 2021.

[131] J. W. Mullinax, C. W. Bauschlicher Jr, and J. W. Lawson. Modeling singlet oxygen-induced degradation pathways including environmental effects of 1, 2-dimethoxyethane in li–o2 batteries through density functional theory. *J. Phys. Chem. A*, 2022.

[132] W.-J. Kwak, H. Kim, Y. K. Petit, C. Leypold, T. T. Nguyen, N. Mahne, P. Redfern, L. A. Curtiss, H.-G. Jung, S. M. Borisov, et al. Deactivation of redox mediators in lithium-oxygen batteries by singlet oxygen. *Nat. Commun.*, 10(1):1–8, 2019.

[133] D. A. Singleton, C. Hang, M. J. Szymanski, M. P. Meyer, A. G. Leach, KK. T. uwata, J. S. Chen, A. Greer, C. S. Foote, and K. N. Houk. Mechanism of ene reactions of singlet oxygen. a two-step no-intermediate mechanism. *J. Am. Chem. Soc.*, 125(5):1319–1328, 2003.

[134] M. N. Alberti and M. Orfanopoulos. Unraveling the mechanism of the singlet oxygen ene reaction: recent computational and experimental approaches. *Chem. Eur. J.*, 16(31):9414–9421, 2010.

[135] J.-M. Aubry, B. Mandard-Cazin, M. Rougee, and R. V. Bensasson. Kinetic studies of singlet oxygen [4+ 2]-cycloadditions with cyclic 1, 3-dienes in 28 solvents. *J. Am. Chem. Soc.*, 117(36):9159–9164, 1995.

[136] L. M. Harwood, J. Robertson, and S. Swallow. Singlet oxygen cycloaddition to dienes: A biomimetic approach to marine endoperoxides? *Synlett*, 1999(09):1359–1362, 1999.

[137] M. Bauch, W. Fudickar, and T. Linker. Stereoselective [4+ 2] cycloaddition of singlet oxygen to naphthalenes controlled by carbohydrates. *Molecules*, 26(4):804, 2021.

[138] A. G. Leach and K. N. Houk. Diels–alder and ene reactions of singlet oxygen, nitroso compounds and triazolinediones: transition states and mechanisms from contemporary theory. *Chem. Commun.*, 12:1243–1255, 2002.

[139] F. Jensen, A. Greer, and E. L. Clennan. Reaction of organic sulfides with singlet oxygen. a revised mechanism. *J. Am. Chem. Soc.*, 120(18):4439–4449, 1998.

[140] G. W. Wanjala, A. N. Onyango, D. Abuga, C. Onyango, and M. Makayoto. Evidence for the formation of ozone (or ozone-like oxidants) by the reaction of singlet oxygen with amino acids. *J. Chem.*, 2018, 2018.

[141] A. Sagadevan, K. C. Hwang, and M.-D. Su. Singlet oxygen-mediated selective c–h bond hydroperoxidation of ethereal hydrocarbons. *Nat. Commun.*, 8(1):1–8, 2017.

[142] A. P. Schaap, A. L. Thayer, G. R. Faler, K. Goda, and T. Kimura. Singlet molecular oxygen and superoxide dismutase. *J. Am. Chem. Soc.*, 96(12):4025–4026, 1974.

[143] A. U. Khan. Singlet molecular oxygen from superoxide anion and sensitized fluorescence of organic molecules. *Science*, 168(3930):476–477, 1970.

[144] E. A. Mayeda and A. J. Bard. Singlet oxygen. suppresion of its production in dismutation of superoxide ion by superoxide dismutase. *J. Am. Chem. Soc.*, 96(12):4023–4024, 1974.

[145] A. U. Khan. Singlet molecular oxygen. a new kind of oxygen. *J. Phys. Chem.*, 80(20):2219–2228, 1976.

[146] A. U. Khan. Direct spectral evidence of the generation of singlet molecular oxygen (1. delta. g) in the reaction of potassium superoxide with water. *J. Am. Chem. Soc.*, 103(21):6516–6517, 1981.

[147] E. J. Corey, M. M. Mehrotra, and A. U. Khan. Water induced dismutation of superoxide anion generates singlet molecular oxygen. *Biochem. Biophys. Res. Commun.*, 145(2):842–846, 1987.

[148] R. Poupko and I. Rosenthal. Electron transfer interactions between superoxide ion and organic compounds. *J. Phys. Chem.*, 77(13):1722–1724, 1973.

[149] G. E. Barlow, R. H. Bisby, and R. B. Cundall. Does disproportionation of superoxide produce singlet oxygen. *Radiat. Phys. Chem*, 13(1-2):73–75, 1979.

[150] J. M. Aubry, J. Rigaudy, C. Ferradini, and J. Pucheault. Search for singlet oxygen in the disproportionation of superoxide anion. *J. Am. Chem. Soc.*, 103(16):4965–4966, 1981.

[151] E. J. Nanni Jr, R. R. Birge, L. M. Hubbard, M. M. Morrison, and D. T. Sawyer. Oxidation and dismutation of superoxide ion solutions to molecular oxygen. singlet vs. triplet state. *Inorg. Chem.*, 20(3):737–741, 1981.

[152] H. Sugimoto, D. T. Sawyer, and J. R. Kanofsky. Transient formation of hydrogen tetraoxide [hooooh] from the dimerization of perhydroxyl (hoo. cntdot.): concerted homolytic dissociation to singlet oxygen (1o2) and hydrogen peroxide. *J. Am. Chem. Soc.*, 110(26):8707–8708, 1988.

[153] E. A. Mayeda and A. J. Bard. Production of singlet oxygen in electrogenerated radical ion electron transfer reactions. *J. Am. Chem. Soc.*, 95(19):6223–6226, 1973.

[154] W. H. Koppenol. Reactions involving singlet oxygen and the superoxide anion. *Nature*, 262(5567):420–421, 1976.

[155] R. A. Marcus. On the theory of chemiluminescent electron-transfer reactions. *J. Chem. Phys.*, 43(8):2654–2657, 1965.

[156] I. Lozano, D. Córdoba, H. Rodríguez, I. Landa-Medrano, N. Ortiz-Vitoriano, T. Rojo, I. R. de Larramendi, and E. J. Calvo. Singlet oxygen formation in nao2 battery cathodes catalyzed by ammonium brönsted acid. *J. Electroanal. Chem.*, 872:114265, 2020.

[157] V. S. Bryantsev, M. Blanco, and F. Faglioni. Stability of lithium superoxide lio2 in the gas phase: computational study of dimerization and disproportionation reactions. *J. Phys. Chem. A*, 114(31):8165–8169, 2010.

[158] U. Das, K. C. Lau, P. C. Redfern, and L. A. Curtiss. Structure and stability of lithium superoxide clusters and relevance to li–o2 batteries. *J. Phys. Chem. Lett.*, 5(5):813–819, 2014.

[159] G. Houchins, V. Pande, and V. Viswanathan. Mechanism for singlet oxygen production in li-ion and metal–air batteries. *ACS Energy Lett.*, 5(6):1893–1899, 2020.

[160] S. Dong, S. Yang, Y. Chen, C. Kuss, G. Cui, L. R. Johnson, X. Gao, and P. G. Bruce. Singlet oxygen and dioxygen bond cleavage in the aprotic lithium-oxygen battery. *Joule*, 2022.

[161] J. R. Kanofsky, H. Sugimoto, and D. T. Sawyer. Singlet oxygen production from the reaction of superoxide ion with halocarbons in acetonitrile. *J. Am. Chem. Soc.*, 110(11):3698–3699, 1988.

[162] M. T. Martins-Costa, J. M. Anglada, and M. F. Ruiz-López. Structure of hydrogen tetroxide in gas phase and in aqueous environments: relationship to the hydroperoxyl radical self-reaction. *Struct. Chem.*, 27(1):231–242, 2016.

[163] M. Catir and H. Kilic. Transient formation of hydrogen tetraoxide from hydrogen peroxide with bis (trifluoroacetoxyiodo) benzene: A chemical generator of singlet oxygen for organic synthesis. *Synlett*, 2003(08):1180–1182, 2003.

[164] A. Samojlov, D. Schuster, J. Kahr, and S. A. Freunberger. Surface and catalyst driven singlet oxygen formation in li-o2 cells. *Electrochim. Acta*, 362:137175, 2020.

[165] S. Meini, N. Tsiouvaras, K. U. Schwenke, M. Piana, H. Beyer, L. Lange, and H. A. Gasteiger. Rechargeability of li–air cathodes pre-filled with discharge products using an ether-based electrolyte solution: implications for cycle-life of li–air cells. *Phys. Chem. Chem. Phys.*, 15(27):11478–11493, 2013.

[166] Z. Zhao, J. Huang, and Z. Peng. Achilles' heel of lithium–air batteries: Lithium carbonate. *Angew. Chem. Int. Ed.*, 57(15):3874–3886, 2018.

[167] D. Cao, C. Tan, and Y. Chen. Oxidative decomposition mechanisms of lithium carbonate on carbon substrates in lithium battery chemistries. *Nat. Commun.*, 13(1):1–12, 2022.

[168] Y. Lin, Q. Yang, F. Geng, H. Feng, M. Chen, and B. Hu. Suppressing singlet oxygen formation during the charge process of li-o2 batteries with a co3o4 solid catalyst revealed by operando electron paramagnetic resonance. *J. Phys. Chem. Lett.*, 12(42):10346–10352, 2021.

[169] K. Böhme and H. D. Brauer. Generation of singlet oxygen from hydrogen peroxide disproportionation catalyzed by molybdate ions. *Inorg. Chem.*, 31(16):3468–3471, 1992.

[170] J. Wahlen, S. De Hertogh, D. E. De Vos, V. Nardello, S. Bogaert, J.-M. Aubry, P. L. Alsters, and P. A. Jacobs. Disproportionation of hydrogen peroxide into singlet oxygen catalyzed by lanthanum-exchanged zeolites. *J. Catal.*, 233(2):422–433, 2005.

[171] F. Waiblinger, J. Keck, A. P. Fluegge, H. Krame, D. Leppard, and G. Rytz. Ultraviolet absorbers and singlet oxygen. *J. Photochem. Photobiol. A*, 126(1-3):43–49, 1999.

[172] M. C. DeRosa and R. J. Crutchley. Photosensitized singlet oxygen and its applications. *Coord. Chem. Rev.*, 233:351–371, 2002.

[173] Z. Jiang, Y. Huang, Z. Zhu, S. Gao, Q. Lv, and F. Li. Quenching singlet oxygen via intersystem crossing for a stable li-o2 battery. *Proc. Natl. Acad. Sci.*, 119(34):e2202835119, 2022.

[174] A. P. Darmanyan, W. S. Jenks, and P. Jardon. Charge-transfer quenching of singlet oxygen o2 ($1\delta g$) by amines and aromatic hydrocarbons. *J. Phys. Chem. A*, 102(38):7420–7426, 1998.

[175] Y. K. Petit, C. Leypold, N. Mahne, E. Mourad, L. Schafzahl, C. Slugovc, S. M. Borisov, and S. A. Freunberger. Dabconium: An efficient and high-voltage stable singlet oxygen quencher for metal–o2 cells. *Angew. Chem. Int. Ed.*, 58(20):6535–6539, 2019.

[176] S. Liu, Z. Wang, C. Yu, Z. Zhao, X. Fan, Z. Ling, and J. Qiu. Free-standing, hierarchically porous carbon nanotube film as a binder-free electrode for high-energy li–o 2 batteries. *J. Mater. Chem. A*, 1(39):12033–12037, 2013.

[177] H.-D. Lim, B. Lee, Y. Zheng, J. Hong, J. Kim, H. Gwon, Y. Ko, M. Lee, K. Cho, and K. Kang. Rational design of redox mediators for advanced li–o2 batteries. *Nat. Energy*, 1(6):1–9, 2016.

[178] R. Black, J.-H. Lee, B. Adams, C. A. Mims, and L. F. Nazar. The role of catalysts and peroxide oxidation in lithium–oxygen batteries. *Angew. Chem. Int. Ed.*, 52(1):392–396, 2013.

[179] R. A. Wong, C. Yang, A. Dutta, M. O, M. Hong, M. L. Thomas, K. Yamanaka, T. Ohta, K. Waki, and H. R. Byon. Critically examining the role of nanocatalysts in li–o2 batteries: viability toward suppression of recharge overpotential, rechargeability, and cyclability. *ACS Energy Lett.*, 3(3):592–597, 2018.

[180] Z. Chang, J. Xu, and X. Zhang. Recent progress in electrocatalyst for li-o2 batteries. *Adv. Energy Mater.*, 7(23):1700875, 2017.

[181] J.-B. Park, S. H. Lee, H.-G. Jung, D. Aurbach, and Y.-K. Sun. Redox mediators for li–o2 batteries: status and perspectives. *Adv. Mater.*, 30(1):1704162, 2018.

[182] Y. K. Petit, E. Mourad, C. Prehal, C. Leypold, A. Windischbacher, D. Mijailovic, C. Slugovc, M. Borisov S, E. Zojer, S. Brutti, et al. Mechanism of mediated alkali peroxide oxidation and triplet versus singlet oxygen formation. *Nat. Chem.*, 13(5):465–471, 2021.

[183] W.-J. Kwak, J. Park, H. Kim, J. M. Joo, D. Aurbach, H. R. Byon, and Y.-K. Sun. Oxidation stability of organic redox mediators as mobile catalysts in lithium–oxygen batteries. *ACS Energy Lett.*, 5(6):2122–2129, 2020.

[184] X. Chen, Z. Luo, X. Zhuge, Z. Ding, Y. Ren, A. Loya, Y. Li, and K. Luo. Protecting lithium anode with ionic liquid modified poly (vinylidene fluoride) single ion conducting separators for iodide-assisted lithium oxygen batteries. *J. Energy Storage*, 50:104580, 2022.

[185] Z. Liang and Y.-C. Lu. Critical role of redox mediator in suppressing charging instabilities of lithium–oxygen batteries. *J. Am. Chem. Soc.*, 138(24):7574–7583, 2016.

[186] Y. Dou, Z. Xie, Y. Wei, Z. Peng, and Z. Zhou. Redox mediators for high-performance lithium–oxygen batteries. *Natl. Sci. Rev.*, 9(4):nwac040, 2022.

[187] Z. Liang, Q. Zou, J. Xie, and Y.-C. Lu. Suppressing singlet oxygen generation in lithium–oxygen batteries with redox mediators. *Energy Environ. Sci.*, 13(9):2870–2877, 2020.

[188] W.-J. Kwak, S. A. Freunberger, H. Kim, J. Park, T. T. Nguyen, H.-G. Jung, Y. R. Byon, and Y.-K. Sun. Mutual conservation of redox mediator and singlet oxygen quencher in lithium–oxygen batteries. *ACS Catal.*, 9(11):9914–9922, 2019.

[189] H.-K. Lee, H. Kim, H.-G. Jung, Y.-K. Sun, and W.-J. Kwak. Ambilaterality of redox mediators towards 1o2 in li-o2 batteries: Trap and quencher. *Adv. Funct. Mater.*, 31(40):2102442, 2021.

[190] H.-D. Lim, H. Song, J. Kim, H. Gwon, Y. Bae, K.-Y. Park, J. Hong, H. Kim, T. Kim, Y. H. Kim, et al. Superior rechargeability and efficiency of lithium–oxygen batteries: hierarchical air electrode architecture combined with a soluble catalyst. *Angew. Chem.*, 126(15):4007–4012, 2014.

[191] W.-J. Kwak, D. Hirshberg, D. Sharon, H.-J. Shin, M. Afri, J.-B. Park, A. Garsuch, F. F. Chesneau, A. A. Frimer, D. Aurbach, et al. Understanding the behavior of li–oxygen cells containing lii. *J. Mater. Chem. A*, 3(16):8855–8864, 2015.

[192] T. Liu, M. Leskes, W. Yu, A. J. Moore, L. Zhou, P. M. Bayley, G. Kim, and C. P. Grey. Cycling li-o2 batteries via lioh formation and decomposition. *Science*, 350(6260):530–533, 2015.

[193] C. Zhang, N. Dandu, S. Rastegar, S. N. Misal, Z. Hemmat, A. T. Ngo, L. A. Curtiss, and A. Salehi-Khojin. A comparative study of redox mediators for improved performance of li–oxygen batteries. *Adv. Energy Mater.*, 10(27):2000201, 2020.

[194] Q. Zhang, Y. Zhou, W. Dai, X. Cui, Z. Lyu, Z. Hu, and W. Chen. Chloride ion as redox mediator in reducing charge overpotential of aprotic lithium-oxygen batteries. *Batteries & Supercaps*, 4(1):232–239, 2021.

[195] V. Pande and V. Viswanathan. Criteria and considerations for the selection of redox mediators in nonaqueous li–o2 batteries. *ACS Energy Lett.*, 2(1):60–63, 2017.

[196] W. Zhang, Y. Shen, D. Sun, Z. Huang, J. Zhou, H. Yan, and Y. Huang. Promoting li2o2 oxidation via solvent-assisted redox shuttle process for low overpotential li-o2 battery. *Nano Energy*, 30:43–51, 2016.

[197] Y. G. Zhu, Q. Liu, Y. Rong, H. Chen, J. Yang, C. Jia, L.-J.Yu, A. Karton, Y. Ren, X. Xu, et al. Proton enhanced dynamic battery chemistry for aprotic lithium–oxygen batteries. *Nat. Commun.*, 8(1):1–8, 2017.

[198] Y. Qiao, S. Wu, Y. Sun, S. Guo, J. Yi, P. He, and H. Zhou. Unraveling the complex role of iodide additives in li–o2 batteries. *ACS Energy Lett.*, 2(8):1869–1878, 2017.

[199] A. Nakanishi, M. L. Thomas, H.-M. Kwon, Y. Kobayashi, R. Tatara, K. Ueno, K. Dokko, and M. Watanabe. Electrolyte composition in li/o2 batteries with lii redox mediators: solvation effects on redox potentials and implications for redox shuttling. *J. Phys. Chem. C*, 122(3):1522–1534, 2018.

[200] G. Leverick, M. Tułodziecki, R. Tatara, F. Bardé, and Y. Shao-Horn. Solvent-dependent oxidizing power of lii redox couples for li-o2 batteries. *Joule*, 3(4):1106–1126, 2019.

[201] Y. Li, S. Dong, B. Chen, C. Lu, K. Liu, Z. Zhang, H. Du, X. Wang, X. Chen, and X. Zhou. Li–o2 cell with lii (3-hydroxypropionitrile) 2 as a redox mediator: insight into the working mechanism of i–during charge in anhydrous systems. *J. Phys. Chem. Lett.*, 8(17):4218–4225, 2017.

[202] T. Liu, G. Kim, E. Jonsson, E. Castillo-Martinez, I. Temprano, Y. Shao, J. Carretero-Gonzalez, R. N. Kerber, and C. P. Grey. Understanding lioh formation in a li-o2 battery with lii and h2o additives. *ACS Catal.*, 9(1):66–77, 2018.

[203] TM. ułodziecki, G. M. Leverick, C. V. Amanchukwu, Y. Katayama, D. G. Kwabi, F. Barde, P. T. Hammond, and Y. Shao-Horn. The role of iodide in the formation of lithium hydroxide in lithium–oxygen batteries. *Energy Environ. Sci.*, 10(8):1828–1842, 2017.

[204] W.-J. Kwak, D. Hirshberg, D. Sharon, M. Afri, A. A. Frimer, H.-G. Jung, D. Aurbach, and Y.-K. Sun. Li–o 2 cells with libr as an electrolyte and a redox mediator. *Energy Environ. Sci.*, 9(7):2334–2345, 2016.

[205] G. Leverick, S. Feng, P. Acosta, S. Acquaviva, F. Bardé, S. Cotte, and Y. Shao-Horn. Tunable redox mediators for li–o2 batteries based on interhalide complexes. *ACS. Appl. Mater. Interfaces*, 14(5):6689–6701, 2022.

[206] R. Bauernschmitt and R. Ahlrichs. Stability analysis for solutions of the closed shell kohn–sham equation. *J. Chem. Phys.*, 104(22):9047–9052, 1996.

[207] H. B. Schlegel and J. McDouall. Do you have scf stability and convergence problems? In *Computational advances in organic chemistry: Molecular structure and reactivity*, pages 167–185. Springer, 1991.

[208] L. V. Slipchenko and A. I. Krylov. Singlet-triplet gaps in diradicals by the spin-flip approach: A benchmark study. *J. Chem. Phys.*, 117(10):4694–4708, 2002.

[209] R. Caballol, O. Castell, F. Illas, I. de Moreira, and J. P. Malrieu. Remarks on the proper use of the broken symmetry approach to magnetic coupling. *J. Phys. Chem. A*, 101(42):7860–7866, 1997.

[210] N. Ferré, N. Guihéry, and J.-P. Malrieu. Spin decontamination of broken-symmetry density functional theory calculations: deeper insight and new formulations. *Phys. Chem. Chem. Phys.*, 17(22):14375–14382, 2015.

[211] G. David, G. Trinquier, and J.-P. Malrieu. Consistent spin decontamination of broken-symmetry calculations of diradicals. *J. Chem. Phys.*, 153(19):194107, 2020.

[212] S. Larsson. Applications of casscf. *Int. J. Quantum Chem.*, 111(13):3424–3430, 2011.

[213] H. Lischka, D. Nachtigallova, A. J. Aquino, P. G. Szalay, F. Plasser, F. B. Machado, and M. Barbatti. Multireference approaches for excited states of molecules. *Chem. Rev.*, 118(15):7293–7361, 2018.

[214] K. Andersson, P. A. Malmqvist, B. O. Roos, A. J. Sadlej, and K. Wolinski. Second-order perturbation theory with a casscf reference function. *J. Phys. Chem.*, 94(14):5483–5488, 1990.

[215] J. P. Zobel, J. J. Nogueira, and L. González. The ipea dilemma in caspt2. *Chem. Sci.*, 8(2):1482–1499, 2017.

[216] C. Angeli, R. Cimiraglia, S. Evangelisti, T. Leininger, and J.-P. Malrieu. Introduction of n-electron valence states for multireference perturbation theory. *J. Chem. Phys.*, 114(23):10252–10264, 2001.

[217] K. G. Dyall. The choice of a zeroth-order hamiltonian for second-order perturbation theory with a complete active space self-consistent-field reference function. *J. Chem. Phys.*, 102(12):4909–4918, 1995.

[218] C. Angeli, R. Cimiraglia, and J.-P. Malrieu. n-electron valence state perturbation theory: A spinless formulation and an efficient implementation of the strongly contracted and of the partially contracted variants. *The Journal of chemical physics*, 117(20):9138–9153, 2002.

[219] R. Sarkar, P.-F. Loos, M. Boggio-Pasqua, and D. Jacquemin. Assessing the performances of caspt2 and nevpt2 for vertical excitation energies. *J. Chem. Theory Comput.*, 18(4):2418–2436, 2022.

[220] J. Finley, P.-Å. Malmqvist, B. O. Roos, and L. Serrano-Andrés. The multi-state caspt2 method. *Chem. Phys. Lett.*, 288(2-4):299–306, 1998.

[221] C. Angeli, S. Borini, M. Cestari, and R. Cimiraglia. A quasidegenerate formulation of the second order n-electron valence state perturbation theory approach. *J. Chem. Phys.*, 121(9):4043–4049, 2004.

[222] A. V. Marenich, C. J. Cramer, and D. G. Truhlar. Universal solvation model based on solute electron density and on a continuum model of the solvent defined by the bulk dielectric constant and atomic surface tensions. *J. Phys. Chem. B*, 113(18):6378–6396, 2009.

[223] M. S. Gordon, M. W. Schmidt, G. M. Chaban, K. R. Glaesemann, W. J. Stevens, and C. Gonzalez. A natural orbital diagnostic for multiconfigurational character in correlated wave functions. *J. Chem. Phys.*, 110(9):4199–4207, 1999.

[224] X. Wang and L. Andrews. Infrared spectra, structure and bonding in the lio2, lio2li, lio and li2o molecules in solid neon. *Mol. Phys.*, 107(8-12):739–748, 2009.

[225] A. Zaichenko, D. Schröder, J. Janek, and D. Mollenhauer. Pathways to triplet or singlet oxygen during the dissociation of alkali metal superoxides: insights by multireference calculations of molecular model systems. *Chem. Eur. J.*, 26(11):2395–2404, 2020.

[226] A. Vlcek Jr, H. Kvapilová, M. Towrie, and S. Záliš. Electron-transfer acceleration investigated by time resolved infrared spectroscopy. *Acc. Chem. Res.*, 48(3):868–876, 2015.

[227] H. J. Wörner, C. A. Arrell, N. Banerji, A. Cannizzo, M. Chergui, A. K. Das, P. Hamm, U. Keller, P. M. Kraus, E. Liberatore, et al. Charge migration and charge transfer in molecular systems. *Structural Dynamics*, 4(6):061508, 2017.

[228] R. A. Marcus. Electron transfer at electrodes and in solution: comparison of theory and experiment. *Electrochim. Acta*, 13(5):995–1004, 1968.

[229] R. A. Marcus. Electron transfer theory and its inception. *Phys. Chem. Chem. Phys.*, 14(40):13729–13730, 2012.

[230] H. Au, H. Alptekin, A. Jensen, E. Olsson, C. A. O'Keefe, T. Smith, M. Crespo-Ribadeneyra, T. F. Headen, C. P. Grey, Q. Cai, et al. A revised mechanistic model for sodium insertion in hard carbons. *Energy Environ. Sci.*, 13(10):3469–3479, 2020.

[231] S. Yu, Z. Liu, H. Tempel, H. Kungl, and R.-A. Eichel. Self-standing nasicon-type electrodes with high mass loading for fast-cycling all-phosphate sodium-ion batteries. *J. Mater. Chem. A*, 6(37):18304–18317, 2018.

[232] K. Märker, C. Xu, and C. P. Grey. Operando nmr of nmc811/graphite lithium-ion batteries: structure, dynamics, and lithium metal deposition. *J. Am. Chem. Soc.*, 142(41):17447–17456, 2020.

[233] M. Gauthier, M. H. Nguyen, L. Blondeau, E. Foy, and A. Wong. Operando nmr characterization of a metal-air battery using a double-compartment cell design. *Solid State Nuclear Magnetic Resonance*, 113:101731, 2021.

[234] K. C. Lau, R. S. Assary, P. Redfern, J. Greeley, and L. A. Curtiss. Electronic structure of lithium peroxide clusters and relevance to lithium–air batteries. *J. Phys. Chem. C*, 116(45):23890–23896, 2012.

[235] J. Yang, D. Zhai, H.-H. Wang, K. C. Lau, J. A. Schlueter, P. Du, D. J. Myers, Y.-K. Sun, L. A. Curtiss, and K. Amine. Evidence for lithium superoxide-like species in the discharge product of a li–o 2 battery. *Phys. Chem. Chem. Phys.*, 15(11):3764–3771, 2013.

[236] D. E. Jensen. Alkali-metal compounds in oxygen-rich flames. a reinterpretation of experimental results. *J. Chem. Soc., Faraday Trans. 1*, 78(9):2835–2842, 1982.

[237] J. M. Plane, B. Rajasekhar, and L. Bartolotti. Theoretical and experimental determination of the lithium and sodium superoxide bond dissociation energies. *J. Phys. Chem.*, 93(8):3141–3145, 1989.

[238] R. S. Assary and L. A. Curtiss. Oxidative decomposition mechanisms of lithium peroxide clusters: an ab initio study. *Mol. Phys.*, 117(9-12):1459–1468, 2019.

[239] B. Hou, X. Lei, Z. Gan, S. Zhong, G. Liu, and C. Ouyang. Structural and electronic properties of small lithium peroxide clusters in view of the charge process in li–o 2 batteries. *Phys. Chem. Chem. Phys.*, 21(36):19935–19943, 2019.

[240] Y. Chen, X. Gao, L. R. Johnson, and P. G. Bruce. Kinetics of lithium peroxide oxidation by redox mediators and consequences for the lithium–oxygen cell. *Nat. Commun.*, 9(1):1–6, 2018.

[241] D. Mester and M. Kállay. Charge-transfer excitations within density functional theory: How accurate are the most recommended approaches? *J. Chem. Theory Comput.*, 18(3):1646–1662, 2022.

[242] B. de Souza, G. Farias, F. Neese, and R. Izsak. Predicting phosphorescence rates of light organic molecules using time-dependent density functional theory and the path integral approach to dynamics. *J. Chem. Theory Comput.*, 15(3):1896–1904, 2019.